ROUGHNESS-INDUCED TRANSIENT GROWTH: CONTINUOUS-SPECTRUM RECEPTIVITY AND SECONDARY INSTABILITY ANALYSIS

A Dissertation

by

NICHOLAS ALLEN DENISSEN

Submitted to the Office of Graduate Studies of
Texas A&M University
in partial fulfillment of the requirements for the degree of

DOCTOR OF PHILOSOPHY

May 2011

Major Subject: Aerospace Engineering

ROUGHNESS-INDUCED TRANSIENT GROWTH CONTINUOUS-SPECTRUM RECEPTIVITY AND SECONDARY INSTABILITY ANALYSIS

A Dissertation

by

NICHOLAS ALLEN DENISSEN

Submitted to the Office of Graduate Studies of
Texas A&M University
in partial fulfillment of the requirements for the degree of

DOCTOR OF PHILOSOPHY

Approved by:

Chair of Committee,	Edward White
Committee Members,	William Saric
	Helen Reed
	Diego Donzis
	Prabir Daripa
Head of Department,	Rodney Bowersox

May 2011

Major Subject: Aerospace Engineering

ABSTRACT

Roughness-induced Transient Growth: Continuous-spectrum Receptivity and
Secondary Instability Analysis. (May 2011)
Nicholas Allen Denissen, B.S., Case Western Reserve University
Chair of Advisory Committee: Dr. Edward White

This dissertation analyzes the effect of periodic roughness elements on the stability of a flat plate boundary layer. Receptivity data is extracted from direct numerical simulations and experimental data and the results are compared to theoretical predictions. This analysis shows that flow in the immediate vicinity of roughness elements is non-linear; however, the evolution of roughness-induced perturbations is a linear phenomena. New techniques are developed to calculate receptivity information for cases where direct numerical simulations are not yet possible. Additionally, the stability behavior of the roughness wake is analyzed. New instability modes are found, and the effect of boundary layer complexity, perturbation amplitude and other factors are examined. It is shown that the wake is much less stable than optimal perturbation theory predicts, and highlights the importance of receptivity studies. The implication of these results on transition-to-turbulence is discussed, and future work is proposed.

ACKNOWLEDGMENTS

I would like to thank Professor Anatoli Tumin for many helpful conversations, and Dr. Donald Rizzetta for access to the DNS results. I also acknowledge fellowship support from the NSF GRFP, and the Texas A&M Dwight Look College of Engineering. I also want to thank my advisor Ed White and the rest of the committee for their input. Finally, too numerous to count, are the people who have supported me throughout this process: family, friends and colleagues.

TABLE OF CONTENTS

LIST OF TABLES

LIST OF FIGURES

FIGURE Page

FIGURE Page

NOMENCLATURE

D	Roughness element diameter
δ	Blasius scaling
δ^*	Displacement thickness
$\delta_{\text{avg}}(x)$	Average boundary layer thickness
λ_k	Roughness element spacing
k	Roughness height
U	Basic state velocity
$\hat{u}(y)$	One-dimensional perturbation
$\tilde{u}(y,z)$	Two-dimensional perturbation
$u'(x,y,z,t)$	Three-dimensional (and time) perturbation
Re	Reynolds number based on δ
Re_k	Roughness-based Reynolds number, $(U(k)k/\nu)$
C_α	Receptivity function
Q_α	Continuous spectrum normalization function
α	Streamwise wavenumber
β	Spanwise wavenumber
$\hat{\Phi}$	Vector of perturbation quantities (9 component)

$\hat{\Psi}$	Vector of adjoint quantities (9 component)
$\hat{\phi}$	Vector of perturbation quantities (6 component)
$\hat{\psi}$	Vector of adjoint quantities (6 component)
κ	Continuous spectrum parameter
λ_{1-6}	Freestream eigenvalues of the Orr–Sommerfeld equation
$\mathcal{L}_{OS}$	Orr–Sommerfeld operator
ω	Temporal wavenumber
c	Phase speed, ω/α
$G(x_*)$	Optimal amplification
λ_0	Optimal energy eigenvalue
$\mathcal{E}[\phi,\phi]_x$	Energy operator
x_*	Optimization distance
F_j	Known partial data vector
$\gamma_{1,2}$	Regularization parameters
$\mathbf{M}_{j\alpha}$	Partial data matrix
γ	Detuning parameter
${}^{(a)}_{\infty}\hat{\phi}^{(b)}_{\alpha}$	$\infty \rightarrow$ Freestream values $a \rightarrow$ freestream mode associated with λ_a $b \rightarrow$ component of vector
$\tilde{T}_y, \tilde{T}_z$	Kinetic energy production from y,z gradients

CHAPTER I

INTRODUCTION AND LITERATURE REVIEW

A. Introduction

The transition of boundary layers from laminar to turbulent flow has attracted wide research interest for over a century. The impact of transition on drag, surface heat flux, turbulent mixing and other phenomena is well documented. For a wide variety of flow conditions an impressive body of knowledge describes the physical mechanisms that bring about the transition to turbulence. Traditional stability approaches that focus on identifying unstable modal solutions of simplified forms of the Navier–Stokes equations have produced a wealth of information for flows of aerodynamic interest. These methods have proved effective for flows with features such as surface curvature, wing sweep and compressibility effects, and can track mode interaction and non-linear development.

For two-dimensional boundary layers, the linearized disturbance equations show that spanwise-invariant traveling waves, Tollmien–Schlichting (T–S) waves, experience energy growth once a certain “critical” Reynolds number is reached. Initially instigated by freestream turbulence, acoustic fluctuations or surface vibrations, these exponentially growing instability waves eventually attain sufficient amplitude that their distortion of the boundary layer becomes significant. This leads to secondary, three-dimensional instabilities of the new base flow, and transition to turbulence. The T–S transition process is understood well enough to appear in general textbooks[1].

Other exponentially growing instabilities exist for more complex boundary layers. The three-dimensional boundary layer on a swept wing produces a different type of

---

The journal model is *IEEE Transactions on Automatic Control.*

modal disturbance. Stationary and traveling crossflow waves grow exponentially before initiating secondary mechanisms. Similarly, concave surface curvature gives rise to exponentially growing Görtler instabilities, with similar results. Compressibility effects in high-speed flows allow multiple unstable waves to coexist and interact even for two-dimensional boundary layers. The common feature of these disturbances is that they are eigenmodes of the linearized Navier–Stokes equations, and their mode shapes and growth rates are completely determined by solving the eigenvalue problem.

Despite this success there is still a great deal that is unknown about the transition process. Of specific relevance to this dissertation, the presence of surface roughness introduces complex behavior into the boundary layer. Much of this behavior has resisted the traditional modal description. Instead, a growing body of work provides evidence that roughness contributes to disturbance growth in the boundary layer via an algebraic-growth mechanism intially proposed by Ellingsen and Palm[2]. This concept was later solidified into the "lift-up" mechanism isolated by Landahl[3] and others[4]. Landhal shows that a perturbation of finite size with a velocity component normal to the base flow, and aligned with the base-flow gradient, results in the algebraic growth of a streamwise disturbance. Further, three-dimensional disturbances of any type with perturbations aligned this way will result in "streaks" of momentum excess and defect as the normal velocity perturbation redistributes streamwise momentum.

This mechanism, as it is now understood, has two important characteristics. First, it can produce disturbance growth in a boundary layer even when no traditional instabilities exist. That is, even though in the limit of long time or streamwise distance all perturbations decay, there can be a period of initial disturbance growth. Second, the theory used to describe these perturbations is *linear* which offers considerable advantages in both computation and understanding necessary for future modeling.

This *Transient Growth* potentially contributes to transition in a variety of contexts, from simple pipe flow, to atmospheric reentry of bluff bodies[5]. In boundary layers, transient growth creates long-lived streamwise streaks. Streaky boundary layers are characterized by adjacent regions of accelerated and decelerated flow relative to the one-dimensional boundary layer, and have been observed as a result of several different forcing mechanisms, including roughness and free-stream turbulence.

Morkovin[6] provides a framework for categorizing the wide variety of behavior seen in boundary layers. The transition roadmap shown in Fig. 1 shows the central role transient growth can play in various transition scenarios. In this figure, Path A represents the modal growth scenarios where a substantial amount of research has brought significant results. This includes Tollmien–Schlicting (T–S) waves, Görtler instabilities, crossflow waves, etc. How these modes grow and produce secondary instabilities, eventually leading to breakdown has been explored in great detail.

Much of the work on roughness effects in boundary layers has focused on Path B, that is, how the complications added to the boundary layer as a result of roughness enhanced T–S wave growth[7, 8, 9]. More recent work has also looked at carefully chosen roughness configurations in hopes of suppressing T–S growth[10, 11, 12]. This work will be discussed in more detail below. However, while Path B is of considerable interest, given the central role T–S waves play in many applications, analysis of Path B transition cannot be divorced from an analysis of Path C transition. In Path C the transiently growing disturbances themselves attain sufficient amplitude to bring about destabilizing secondary effects. In fact, for relatively high-amplitude three-dimensional roughness, the T–S mechanism does not provide an explanation for transition[13], and transient growth is thought to be of central importance. The potential for transient growth to trip turbulence must be taken into account when analyzing the impact of transient growth on modal instabilities. Certainly any attempt to modify the boundary layer in a predictable manner to control modal growth must be concerned with unintentionally pushing the flow down Path C.

An analysis of Path C transition in the wake of surface roughness involves several stages. Following the roadmap, there is first a receptivity phase, where the boundary layer converts the roughness into a flow perturbation. A great deal of research effort has been devoted to receptivity in the past as physics-based models for receptivity are challenging to obtain. Unlike the growth of the perturbation itself, which this work will show can be modeled by the linearized equations, the initial input forcing is difficult to quantify and generalize. This problem is heightened in the case of transient growth as there is no fixed mode-shape to look for when analyzing experiments or direct numerical simulation (DNS)[14]. The mode shape *and* the growth rate are both determined by the receptivity, not by the eigenvalue problem. One of the key focuses of the present dissertation is to fully capture this receptivity mathematically so progress can be made in modeling the physics of the receptivity process. Experiments point to the receptivity process being non-linear, even though the subsequent evolution of the perturbation is linear[15].

The receptivity phase is followed by a period of transient growth, where the perturbation generated by the roughness grows larger and begins to distort the mean-flow. This growth is a linear process. Each of the eigenmodes that comprise the perturbation decays; however, the sum of these modes experiences net energy growth. This is possible because the linearized Navier–Stokes operator is non-normal, and thus the eigenmodes are non-orthogonal[16]. That is, they may interfere destructively with one another at one location, and constructively at another. This growth and decay is computed by tracking every mode in the boundary layer, unlike T–S-type disturbances where only the growing modes (and possibly some of the harmonics) must be computed.

As it evolves, the transiently growing perturbation alters the mean-flow, creating streamwise streaks. These streaks risk destabilization by secondary, inflectional, instabilities once they reach sufficient amplitude. It is this combined base-flow, Blasius flow plus transient growth, that generates exponential instabilities. The growth rates and mode shapes of these secondary instabilities can be computed by solving a set of coupled eigenvalue problems. A complete analysis of receptivity, transient growth, and potential secondary instabilities forms the primary objectives in the present work.

This dissertation has two main parts. The first part fully quantifies the boundary layer receptivity to an array of roughness elements, and analyzes the energy growth of each spanwise harmonic. Quantitative receptivity information is extracted from a physically-realized, transiently-growing perturbation for the first time. This can be used to demonstrate the linearity of disturbances generated by a class of roughness elements in both experiments and DNS. Further, this analysis allows for quantitative comparison between theoretical, experimental, and numerical approaches to the receptivity problem.

The second part addresses the latter stage, the resulting instability of the roughness wake as the perturbation evolves downstream. This builds on the the linear nature of roughness wake, and systematically analyzes the stability characteristics of the resulting secondary flow. This analysis shows that, relative to previously analyzed theoretical models of transient growth (optimal perturbation theory), the physically-realized transient growth is less stable to inviscid/inflectional instabilities. Furthermore, the combination of different spanwise harmonics generated by realistic roughness gives rise to more unstable secondary modes than previous work. The stability analysis is compared to experimental evidence to isolate the physical mechanisms that lead to transition in the wake of surface roughness.

B. Roughness-induced Transition

Although it is usually assumed in fluid dynamic analyses, no surface is truly smooth. A great deal of attention has been focused on the effect of roughness on transition given the observed sensitivity of the transition process. These investigations have proceeded in several stages. The goal of the present work is to contribute to a more detailed physical and mathematical understanding of these past results. It is important to summarize what is known about the stability of boundary layers in the presence of surface roughness so that the current results can be properly contextualized and applied.

Initial investigations, the "pre-history" of roughness-induced transition experiments, sought to produce workable engineering correlations for roughened surfaces. These works, including efforts by well known researchers such as Dryden[17], and Klebanoff[18] formed the initial understanding of the effect of rough surfaces on transition location. The primary findings were noting the importance of the height of the roughness to the thickness of the boundary layer (k/δ^*), and noting that over both distributed roughness and localized 2D roughness the transition location moves forward. In 2D this was explained by the presence of a persistent separation region in the wake of the roughness. This separated region created both an inflection point and decelerated flow which amplified T–S wave receptivity and growth. This established the effectiveness of 2D trips for triggering turbulence.

Work on 3D roughness gave results that were less easily understood. While a separation region may be present in the wake of 3D roughness, it is short-lived. Researchers noted the relevance of the Reynolds number based on roughness height ($Re_k = U(k)k/\nu$), as well as behavior deemed "critical." That is, the transition location experienced sharp movements as Re_k was increased above a critical threshold

[19, 20]. Trying to build engineering models and correlations to describe transition in the presence of surface roughness made it clear that complex behavior was at work in the wake of roughness elements and generated great interest in trying to understand the physics of this phenomena as stability theory became increasingly effective. Developments in stability theory motivated the first generation of experiments on the physics of transition on roughened surfaces.

Generation 1 (1980s)

The first generation of detailed experiments involving 3D roughness include work by groups at Case Western Reserve University[7], the Jet Propulsion Lab[9], and the Illinois Institute of Technology[8], as well as continued work at NIST (cited as private communication in Ref. [21]). Reshotko and Leventhal[7] found that transition moves forward when distributed roughness (sandpaper) was placed in the region sub-critical to T–S-wave growth, an effect partly attributed to the thickening of the boundary layer as well as larger initial unsteadiness. In addition, for sufficiently high amplitude roughness, transition was observed with no sign of a T–S-type mechanism. This was referred to as “bypass” transition because the usual linear growth stage is bypassed. Moving this roughness into the region where T–S waves are unstable, Corke et al.[8] found that although the roughness did not seem to create inflectional profiles away from the wall, the streamwise vorticity generated by roughness, as well as the decelerated flow near the wall, likely play a role in accentuating T–S growth, and increasing the boundary layer’s susceptibility to secondary instabilities. Further work at IIT also showed that the despite the complexity of the flow topology behind three-dimensional roughness elements, the vortex structure and resulting streaks were near-universal regardless of the shape of the roughness (cylinder, squares, etc.)[22].

In an experiment that presages those that will be the focus in this dissertation, Kendall[9] investigated the boundary layer response to an array of roughness elements that were both repeatable and of significant size. He arranged an array of spheres on a flat plate and contrasted results with single spheres and multi-sphere arrays. These spheres produce counter-rotating vortex pairs that are persistent (i.e. long lasting in the streamwise direction), and he found inflectional profiles (in the wall-normal direction) may indeed exist, though closer to the wall surface than was able to be measured previously in experiments involving distributed roughness. The difficulty in measuring boundary layer profiles in and around surface roughness is a problem that still attracts attention today.

Many of these results were summarized by Morkovin[21], who noted several things that will be important when analyzing the present results. First he notes that "The *incubation distance* from the offending roughness to the roughness-conditioned transition is *initially very long*" (emphasis in the original). This incubation distance makes parameter-based correlations extremely difficult and argues for the necessity of greater physical understanding of the flow behavior in the wake of roughness elements. In retrospect this can be seen as evidence for a period of transient growth behind roughness elements and of a tradeoff between roughness accentuating T–S wave breakdown versus causing "bypass" transition. A modern look at these results will make some sense of these findings.

Second, Morkovin noted that roughness acted as a receptivity source and "*increased three dimensionality* due to the roughness and consequently an *earlier* onset of *secondary* Herbert-type *instability* was observed." This conclusion will be of great importance when analyzing the potential for control strategies based on deliberately applied surface roughness. Any positive impact gained by limiting the growth of the initial 2D T–S wave must be balanced against the effects on the 3D secondary disturbances that bring about rapid transition to turbulence. The tendency of roughness to act as a receptivity source will make e^N type methods more challenging as initial conditions based on smooth leading edges may not be applicable. Secondary instabilities in wind tunnels may be much more pronounced than for "disturbance-free" DNS. Additionally, the extent to which secondary instabilities generated by the roughness wakes interact with traditional primary/secondary instabilities is of great interest (though a full treatment is beyond the scope of this work).

Finally, Morkovin notes that "Reshotko (1984) wrote of an indication that the departure from laminar flow was 'explosive'." This will be relevant in analyzing the growth rates observed in the secondary instability analysis. Although T–S waves grow exponentially, the growth rate is relatively slow, the secondary instability results in this dissertation will have growth rates that are orders of magnitude larger.

Generation 2 (1990s)

Subsequent to the work summarized by Morkovin, the next generation of experiments was undertaken with knowledge of secondary instabilities beginning to be well established[23]. Klebanoff et al.[24] looked extensively at isolated roughness elements. In addition to documenting "shedding" frequencies and critical Re_k values for both hemispheres and cylinders the authors offered an explanation of the wake behavior consistent with an inflectional instability. Further, the extreme sensitivity to the disturbance environment was seen as evidence of a secondary instability tied to inflectional behavior. The authors admitted that this model was not consistent with some other works, specifically work by Morkovin that found significant growth but subsequent decay of vortical structures. This result is now explainable via the transient growth mechanism.

The most direct predecessor to the current transient growth experiments was done at Novosibirsk in the mid 1990's. Bakchinov et al.[25] performed detailed hotwire measurements behind an array of rectangular roughness elements and found several important results. First, they posited that even at roughness-based Reynolds numbers well in excess of any that will be looked in this dissertation, the elements themselves did not cause transition, but rather created stationary vortex structures on which a secondary instability grew. Further, they found that this instability was associated with the spanwise gradients in the mean flow, and took place at a frequency well above the unstable T–S frequency band. These three findings are in good agreement with the secondary instability calculations that will be presented in this dissertation.

Optimal Theory

While the second generation of experimental work was underway a change in the theoretical approach to the problem was taking place. Realizing that significant disturbance growth could take place even if all the modes were damped, focus was shifted away from the eigenvalue problem and toward the initial value problem (IVP) for a flow perturbation. Using a variational calculus approach, Butler and Farrell[26] solved the IVP for the "optimal" input perturbation. That is, the input perturbation that leads to the most energy growth over a finite streamwise domain. This approach exploited the fact that the spectrum of the Orr–Sommerfeld operator is non-self-adjoint. Thus, eigenmodes can cancel one another at one location, and at another location this cancellation can decrease, yielding a period of strong energy growth in the absence of any modal instability.

This helped form the basis for transient growth and was further grounded mathematically by Schmid and coworkers[27, 28]. These works formulated the optimization problem as a singular value decomposition (SVD) and generalized the approach. This dissertation will show the variational calculus approach of Butler and Farrell and the SVD approach of Schmid and Henningson are equivalent.

Following this initial formulation, the approach was extended to non-parallel boundary layers[29], as well as to the spatial evolution framework[30]. These studies solidified that the optimal perturbation, in terms of the ratio of input to output energy, is a stationary streamwise vortex. This vortex efficiently redistributes the mean flow momentum, causing large boundary layer disturbances with little input energy. These resulting disturbances take the form of streamwise streaks, regions of adjacent high-speed and low-speed flow. These streaks grow algebraically until the streamwise vortex dissipates and the streak begins to decay exponentially. This mechanism fit well with previous work with boundary layers subject to freestream turbulence[31, 32] (which is beyond the scope of the present work) as well as experiments involving three-dimensional roughness elements. By the end of the decade the transient growth mechanism became a suspect in a variety of previously challenging transition scenarios including pipe flow, reentry of blunt bodies, and the effect of distributed roughness[5].

These optimal disturbances have formed the foundation for much of the numerical and theoretical work done over the past ten years. Notably, extensive secondary instability calculations were performed by Andersson et al.[33] that mapped neutral curves and growth rates depending on the amplitude of these optimal perturbations. Their approach will form the basis of the secondary instability calculations in this dissertation and the physical results are the point of departure for the present work. Additionally, optimal perturbations are used in computational studies by Cossu and Brandt[11, 34] that show T–S waves are attenuated by the inclusion of streaks in the boundary layer.

Optimal perturbations have seen some success in analyzing perturbations induced in a boundary layer as a result of freestream turbulence (FST). Experimental work by Westin et al.[31] and Matsubara and Alfreddson[32] found fluctuations in the boundary layer whose peak amplitude agreed with optimal perturbation predictions.

However, explicit comparison is challenging as it is difficult to divorce any potential transient growth from the disturbance accumulation as the FST interacts with the boundary layer. Work in the second part of this dissertation suggests that this agreement may be more the result of non-uniform dissipation of the vortical fluctuations in the certain regions of the boundary layer as opposed to a specific growth mechanism.

Generation 3 (2000's)

The potential of transient growth to explain earlier work in roughness-induced transition spurred a great deal of research interest. In many ways these new studies mirrored experiments done previously. Now researchers had a different focus, a new mechanism to look for that would explain the results that had been baffling in previous work. Using a setup similar to Backhinov et al.[25], White[14] was able to clearly identify transiently growing perturbations in the wake of cylindrical roughness elements.

In some ways these experimentally measured perturbations agree qualitatively with the results obtained by the optimal perturbation models. The general behavior of algebraic growth followed by exponential decay is clear in the experiments. However, the growth rates, and the development lengths (Morkovin's "incubation distances") over which the growth took place are significantly different than those predicted by optimal theory. Also, these perturbations achieved their maximum disturbance amplitude lower in the boundary layer than optimal predictions, in contrast to the results found in experiments using FST. These disturbances were termed "sub-optimal." Using a similar setup of cylinders, Frannson et al.[35] saw similar behavior, and this setup has become a canonical one for studying transient growth. In all experiments and simulations known to the author physically realized perturbations have been found to exhibit this sub-optimal behavior.

Another feature of physically-realized transient growth, in contrast to the optimal theory, is the rich behavior found in the wake of the roughness elements. Transient growth is seen in several spanwise wavelengths, including the element spacing (λ_k), and the element diameter ($\lambda_k/3$ in the case analyzed in this dissertation), but also wavelengths that aren't directly forced such as $\lambda_k/4$. Additional work by White and coworkers[15, 36] revealed more complex behavior as the diameter of the cylinders was varied. This makes it clear that optimal theory alone is unlikely to capture the behavior behind physical surface roughness.

Despite the complex behavior found in the experiments some general trends were identified in the work by the White group. Importantly, the total disturbance energy generated by the roughness elements scales well with Re_k^2, collapsing disturbance energy curves for different roughness heights. This finding, that the energy scaled non-linearly with the height of the roughness, was unexpected and initially at odds with linear stability and optimal perturbation theory. The validation of this scaling is evidence of complex receptivity phenomena prior to the linear transient growth phase. This scaling has been verified through continued work[37] and unsteady contours in the wake of these elements have been documented[36, 37] and will be used to analyze the secondary instability results in this dissertation. Additionally, despite the perturbations increasing in magnitude as Re_k is increased, the location in the boundary layer where the peak fluctuations occur is only weakly affected by changing the element height. Thus, increasing the height of the roughness element changes the amplitude but not the shape of the perturbation. This fact makes it possible to use a rescaled velocity perturbation as a proxy for changing roughness height.

Modern computational tools have also been brought to bear on this problem. Direct numerical simulations (DNS) show promising agreement with the experimental work. Initial analysis by Fischer and Choudhari[38] captures the behavior in different spanwise harmonics for a relatively low $Re_k = 119$. A more detailed simulation on higher Re_k configurations (202, 334) was performed by Rizzetta and Visbal[39]. This simulation shows good agreement with the streamwise velocity measurements made by White and coworkers, and the data from this DNS will be used throughout this dissertation. Additionally, work is proceeding by Goldstein and coworkers[40] at the University of Texas using immersed boundary methods.

Emerging Work

In addition to the work already discussed there is recent work that, while it does not form the basis of this dissertation, informs the present work. Downs et al.[41] extends previous work done by the White group by employing a novel method of generating repeatable randomized roughness. Experiments with these distributed roughness patches show many features similar to work done with discrete cylinders. Some of the numerical work done for this dissertation is undertaken with the goal of expanding the techniques to future work on this type of distributed roughness. The complexity of the surface makes a fully-resolved DNS very challenging. The present work develops an analytical tool that does not rely on DNS, making analysis of this complex case possible.

Additionally, groups at The Royal Institute of Technology (KTH) in Sweden have investigated using controlled roughness to attenuate the growth of T–S waves both numerically[11] and experimentally[10]. In light of these works a more detailed examination of the transient growth and secondary instabilities behind roughness elements will be critical in judging their effectiveness. Moving away from roughness and toward vortices generated by plasma actuators, Hanson et al.[12] have investigated boundary layer control methods by vortex generation. These vortices seem to behave similarly to those generated by roughness elements, and so a deeper understanding of boundary layer response to roughness would be beneficial.

C. Approach and Organization

The objective of this dissertation is to fully analyze transiently growing perturbations, from receptivity to secondary instability, and contrast these results with optimal perturbations, DNS, and experiments. The focus will be on the aspects of transient growth most directly applicable to roughness effects. Three numerical/theoretical tools are used to investigate the evolution of a transiently growing perturbation. Multimode decomposition, based on the Biorthogonal Eigenfunction (BES) formalism developed by Tumin[42], will be derived and employed to calculate receptivity information for transient growth seen in DNS. This formulation allows for a complete solution to the initial value problem in wall-bounded flows. A good deal of time will be spent developing the method as it is somewhat abstract and an extended derivation does not exist in the literature. Also, multimode decomposition will be expanded to analyze the receptivity in experimental data.

In lieu of calculating receptivity information using multimode decomposition, previous authors have used optimal perturbation theory to generate initial conditions for transient growth. The present work will use these optimal calculations to contrast with the behavior of roughness-induced transient growth. Methods for computing optimal perturbations will be shown both using a variational calculus approach[26] and a singular value decomposition method[28]. Third, a numerical solution of the two-dimensional inviscid stability problem[33] is used to study the secondary instabilities in the transiently growing boundary layer. Thorough background on all the mathematical techniques and numerical methods employed will be given in the subsequent sections.

The dissertation is organized as follows. Chapter II outlines the linearized disturbance equations and the methods used to solve the eigenvalue problem, the optimal perturbation problem, and the modal decomposition. Chapter III uses these tools to analyze transient growth in both experiments and DNS, demonstrating the flows linearity and mathematically quantifying the receptivity. Chapter IV introduces the terminology and methods for calculating secondary instabilities and addresses the necessary numerical methods for solving this problem. Chapter V gives the results of secondary stability calculations for a model boundary layer based on optimal perturbation theory as well as roughness-induced transient growth computed via DNS. Chapter VI offers conclusions about roughness-induced transient growth and outlines future work to be undertaken.

CHAPTER II

TRANSIENT GROWTH THEORY

Linear stability analysis provides insight into the physics governing transition from laminar to turbulent flow. The complete Navier–Stokes equations are linearized around a known basic state by neglecting higher-order disturbance quantities. The resulting linear system is then analyzed to show if small perturbations are likely to grow as they evolve in time and space. For this study of transient growth, the Navier–Stokes equations are linearized about a zero-pressure-gradient flat plate boundary layer. The goal is to use these linearized equations to describe the evolution of transiently-growing perturbations.

The resulting system of equations, the Orr–Sommerfeld/Squire (OSS) equations, is very familiar, but in the present work some features of the OSS system will be used in less typical ways. For traditional instabilities the goal is to find the unstable eigenvalues. Once found, the solutions of the eigenvalue problem provide the growth rates, spatial and temporal frequencies, mode shapes and other information about the exponentially growing perturbations. For analysis of transient growth the approach is different. The initial value problem (IVP) must be solved using the full eigenvalue spectrum. The details of the decaying spectrum cannot be ignored. Because the complete spectrum is necessary, and due to the complexity of the OSS spectrum, the usual equivalence between the mathematical Fourier transform and the normal-modes *ansatz* is not as straightforward.

Care must be taken in the derivation of the OSS system to identify features in the complex plane that will be important in interpreting the solution in physical space. While this is straightforward for discrete eigenvalues, it is more involved when trying to resolve the continuous spectrum that exists for boundary-layer flows. The discrete eigenvalues of the Orr–Sommerfeld equation do not form a complete set for boundary-layer flows. To solve the IVP, the contribution from a continuous spectrum of eigenvalues must be taken into account[16]. It is these additional eigenfunctions stemming from the continuous spectrum that are non-orthogonal and their integrated contribution creates transient growth. The goal is to solve the IVP by expanding an arbitrary disturbance into an integral of solutions whose eigenvalues belong to the continuous spectrum. The amplitude distribution among the continuous spectrum modes provides the important receptivity information necessary for characterizing roughness-induced perturbations. To highlight the relevant features, some details of the derivation of the Orr–Sommerfeld equation are important.

A. Linearized Equations and Continuous Spectrum

Starting with the Navier–Stokes equations for an incompressible Newtonian fluid, suitably non-dimensionalized:

$$\frac{\partial \mathbf{u}}{\partial t} + (\mathbf{u} \cdot \nabla)\mathbf{u} = -\nabla p + \frac{1}{Re}\nabla^2 \mathbf{u} \tag{2.1}$$

an expansion is formed by substituting $\mathbf{u} = [U(y), 0, 0]^T + [u', v', w']^T$ and $p = P + p'$. The variables with capital letters are the mean quantities found from the Blasius profile and primes represent small perturbations (functions of x, y, z and t). Making this substitution, subtracting the mean flow, and neglecting terms that are products of the perturbed quantities yields the following linearized system:

$$\begin{aligned}
\frac{\partial u'}{\partial x}+\frac{\partial v'}{\partial y}+\frac{\partial w'}{\partial z} &= 0 \\
\frac{\partial u'}{\partial t}+U\frac{\partial u'}{\partial x}+v'\frac{\partial U}{\partial y} &= -\frac{\partial p'}{\partial x}+\frac{1}{Re}\nabla^2 u' \\
\frac{\partial v'}{\partial t}+U\frac{\partial v'}{\partial x} &= -\frac{\partial p'}{\partial y}+\frac{1}{Re}\nabla^2 v' \\
\frac{\partial w'}{\partial t}+U\frac{\partial w'}{\partial x} &= -\frac{\partial p'}{\partial z}+\frac{1}{Re}\nabla^2 w'
\end{aligned} \tag{2.2}$$

For the purpose of stability and receptivity analysis, the linearized disturbance equations are analyzed more readily in spectral rather than physical space. However, some care is necessary when defining the transformation to spectral space to account for transient mechanisms. Traditional modal growth analysis focuses on the normal modes. Solutions of the form $\mathbf{u}' = \hat{\mathbf{u}}(y)\exp\left[i(\alpha x+\beta z-\omega t)\right] + \text{c.c.}$ are assumed, with $\hat{\mathbf{u}} \rightarrow 0$ as $y \rightarrow \infty$. This approach can be problematic as foregoing a rigorous Fourier transform in favor of exclusively focusing on normal modes suppresses non-exponential, transient effects and yields only the discrete eigenvalues. These discrete modes cannot be used to represent an arbitrary perturbation[43].

The continuous spectrum accounts for these lost transient effects. The normal mode solution is substituted as before, and the boundary conditions for each eigenmode are no slip and no penetration at the wall: $\hat{\mathbf{u}} = 0$ at $y = 0$. However, in the freestream, the modes are only required to be bounded, $|\hat{\mathbf{u}}| < \infty$ as $y \rightarrow \infty$. When the total contribution of the continuous spectrum is considered the result will sum to zero far from the wall for a localized perturbation. This relaxed boundary condition defines the continuous spectrum and makes the set of eigenvalues complete. It is important to note there is an equivalence between this spectrum of solutions with relaxed boundary conditions and the inverse Fourier transform operation that is necessary to account for transient effects[44].

With the substitution carried out, the partial derivatives are replaced with with multiplication by the wavenumbers (e.g. $\partial u'/\partial x \rightarrow i\alpha\hat{u}$). This removes the derivatives with respect to the variables that do not appear in the basic state and leaves a linear ordinary differential equation whose derivative is in the wall-normal direction (y). This is the OSS system:

$$\frac{\partial\hat{\phi}}{\partial y} = \mathcal{L}_{OS}\hat{\phi} \tag{2.3}$$

where $\hat{\phi} = [\hat{u}, \partial\hat{u}/\partial y, \hat{v}, \hat{p}, \hat{w}, \partial\hat{w}/\partial y]^T$ (the hats denote one-dimensional variables in Fourier space). The components of the OSS operator, $\mathcal{L}_{OS}$, can be found in Appendix A.

Because spatial, not temporal, evolution of disturbances is observed in experiments[30], Eq. 2.3 is an eigenvalue problem that is solved for complex α corresponding to specified real-valued β and ω. This spatial versus temporal distinction is important because Gaster's transformation, which is used to convert between spatial and temporal stability, is not well defined for the continuous spectrum solutions.

Successful analytical and numerical approaches to Eq. 2.3 have been known for several decades. In the freestream where $U \rightarrow 1$ and $\partial U/\partial y \rightarrow 0$, $\mathcal{L}_{OS}$ reduces to a matrix of constant coefficients, and solutions take the form $\hat{\phi} \propto e^{\lambda y}$. This system has 6 eigenvalues, 2 of which are repeated:

$$\begin{aligned} \lambda_1 &= -\sqrt{\alpha^2+\beta^2} & \lambda_2 &= +\sqrt{\alpha^2+\beta^2} \\ \lambda_{3,5} &= -\sqrt{i(\alpha-\omega)Re+\alpha^2+\beta^2} & \lambda_{4,6} &= +\sqrt{i(\alpha-\omega)Re+\alpha^2+\beta^2} \end{aligned} \tag{2.4}$$

The corresponding eigenvectors are basis functions for solutions in the freestream (see Appendix 1).

In general, two classes of solutions to Eq. 2.3 exist. One class, the discrete modes, tend to zero as $y \rightarrow \infty$. Thus, in the freestream, their solution must be a linear combination of eigenvectors associated with the eigenvalues $\lambda_{1,3,5}$ (using the principal value of the complex square root). These freestream solutions can be integrated from the freestream to the wall, and combined to satisfy the wall boundary conditions (though in practice this method is unwieldy). There are only finitely many values of α that allow $\hat{\phi}$ to satisfy the three wall boundary conditions, and no solutions of this type for steady flow ($\omega = 0$). Fig. 2(a) shows an example of a discrete mode, the well-known Tollmien–Schlichting wave.

The second class of solutions, the continuous spectrum modes, requires only boundedness as $y \to \infty$. In the freestream, this means λ is purely imaginary, $\lambda = i\kappa$ where κ is any non-negative real number. Fig. 2(b) shows an example of a continuous spectrum mode. It is this type of mode that will be used to describe an arbitrary perturbation. In the freestream $\hat{\phi} \propto \exp(\lambda_j y) = \exp(i\kappa y)$, and κ can be interpreted as a wall-normal wavenumber of an oscillatory solution in y. κ also dictates the decay rate of each individual mode, as it parameterizes the eigenvalue α. It is this variability in decay rates, combined with the non-normality of the OSS operator, that produces transient growth.

When λ is purely imaginary, instead of having three solutions to satisfy the three wall boundary conditions, there are at least four, as $\lambda_{2,4,6}$ become acceptable solutions for continuously distributed values of α. As κ is varied along the positive real line, α traces a path in the complex plane that gives the continuous spectrum. For cases in which $\omega \neq 0$, $\lambda_j = i\kappa$ produces four such paths (corresponding to the four distinct eigenvalues), or branches, in the complex α plane.

Figure 3 shows a schematic of the α plane that defines the different types of modes. The first region is when α does not lie on either the imaginary axis, or the hyperbolic branch cut. In this area of the complex α plane, three of the eigenvalues defined by Eq. 2.4 will be positive, and three will be negative. The positive exponential terms are eliminated, and the remaining three basis functions can be combined to satisfy the three boundary conditions. If an eigenmode can be found that satisfies the three boundary conditions it is a discrete mode (T–S wave). If the value of α in this region is not part of the discrete spectrum it is part of the resolvent set and there is no non-trivial solution.

If a value of α is chosen along the branch cuts, there are now more than 3 basis functions available as some of the eigenvalues will be purely imaginary, and not eliminated by the boundedness condition. Thus, all values of α along the branch cuts constitute potential solutions to the eigenvalue problem. The solutions found using α along the hyperbolic branch are the vorticity modes[30], because they have non-zero vorticity in the freestream. This branch is found by setting $\lambda_{3-6} = i\kappa$. The solutions found along the imaginary α axis branch cuts are pressure modes, from setting $\lambda_{1,2} = i\kappa$, because they have non-zero pressure perturbations in the freestream.

Substituting the branch values into Eq. 2.4 gives the dispersion relations.

$$\alpha_{1,2} = \pm i\sqrt{\kappa^2 + \beta^2}, \quad \alpha_{3-6} = -\frac{iRe}{2}\left[1 \pm \sqrt{1 + \frac{4(\beta^2 + \kappa^2 - i\omega Re)}{Re^2}}\right] \tag{2.5}$$

Branches in the lower half plane, corresponding to α with a negative imaginary part do not represent exponentially growing disturbances. Rather, α values with a negative imaginary part represent upstream traveling solutions with rapidly decaying upstream growth rates[44]. Considering these solutions makes the problem ill-posed from an initial-value problem perspective. Knowledge about the initial condition and direction of wave propagation eliminates these two branches. Only parts of the continuous spectrum with an imaginary part of α greater than zero are considered in the expansion. This is consistent with the idea that transient growth stems only from decaying modes. For a detailed discussion of these branches and the structure of the complex plane see Ref. [44].

At low amplitudes, surface roughness produces stationary disturbances, $\omega = 0$. As the frequency of the disturbance tends to zero the vorticity branches approach the imaginary axis because the term in square brackets in Eq. 2.5 is purely real. Fig. 4 shows an example of this shift as a function of decreasing ω. For the present case, all branches approach the imaginary axis, and therefore all α are purely imaginary. This means the vorticity and pressure branches lie on top of each other for a segment of the complex plane. Fig. 5 shows schematically the structure of an integral in the complex α plane for the present case, the diversion around the branch cut includes the continuous spectrum modes in the inverse Fourier transform.

Only the branches that come from setting $\lambda_{3-6} = i\kappa$, the vorticity modes, will be considered. The pressure modes, $\lambda_{1,2} = i\kappa$, decay much faster and should not play an important role. With $\lambda_{3-6} = i\kappa$ there are four solutions that satisfy the boundary conditions beginning at the branch point, $\alpha \approx i\beta^2/Re$. However, these four are two complex-conjugate pairs and thus only two of the four are independent. The two independent branches will be referred to as the A and B branches, and an A and B mode exist for every α along the imaginary axis starting at the branch point. Only modes up to the branch point for the pressure modes ($\alpha = i\beta$) will be considered. Solutions above this point are neglected due to their rapid spatial decay. The goal is to solve the initial value problem by expanding an arbitrary disturbance into an integral of solutions whose eigenvalues belong to the A and B mode branches spanning $\alpha_i \in [\beta^2/Re, \beta]$.

B. The Receptivity Problem

Chapter I explains the Transition Roadmap provided by Morkovin in Fig. 1. The second block in the roadmap encapsulates the idea of receptivity. Receptivity is the process by which environmental disturbances like freestream turbulence, acoustic fluctuations, or geometric features like surface roughness are absorbed into the boundary layer and converted into flow perturbations. Receptivity has attracted significant interest because it provides the crucial initial condition in determining transition to turbulence that linear theory alone cannot provide. The relation between input environmental disturbances and the resulting amplitude of the growing instability has been studied computationally and experimentally for various combinations of modal instabilities (T–S, Crossflow. . .) and environmental forcing (freestream turbulence, acoustic forcing, roughness. . .). This work has been critical in explaining some of the complexity observed in predicting transition onset.

When measuring receptivity for a modal disturbance in an experimental or computational environment the growth rate and mode shape are known a priori. That is, the Orr–Sommerfeld/Squire system determines how the growing instability looks as well as how it evolves downstream. By taking careful measurements the mode shape of interest can be extracted, validated, and its growth calculated. Once these measurements are complete, the initial amplitude that resulted from the input forcing can be found. Thus a one-to-one correspondence between input forcing and output response can be formulated in terms of a single receptivity coefficient.

For transient growth this input-output formulation is less straightforward. There is not a unique mode of interest that can be measured independently of other disturbances present in the boundary layer. This is particularly problematic because in the case of transient growth receptivity sets the initial amplitude, the growth rate *and* the mode shape. Experiments have been able to formulate trends that correlate an input parameter such as the roughness height (Re_k) with an output description of the disturbance energy generated[15, 37]; however, apportioning this energy into its constitutive modes in a way that allows predicting downstream energy evolution or making comparisons across different types of roughness has not been possible. Because an eigenfunction exists at every point along the branches defined in Eq. 2.5, and because all modes play a role in transient growth, a receptivity *function*, instead of a receptivity *coefficient*, must be defined along the branch cut in the complex α plane to describe the initial disturbance.

Solving the receptivity problem gives a distribution of modal amplitudes, C_α that allows the perturbation to be computed at any downstream location as an integral over the continuous spectrum α values.

$$\phi(x, y, \beta, \omega) = \sum_{A,B} \int_\Gamma C_\alpha \hat{\phi}_\alpha(y) e^{i\alpha x} d\alpha \tag{2.6}$$

In Eq. 2.6 it is implied that C_α, and $\hat{\phi}_\alpha$ are functions of complex α for a fixed set of parameters, β, ω, Re etc., depending on the spanwise/temporal modes of interest. Here Γ is a curve in the complex α plane diverting around the continuous spectrum branches defined in Eq. 2.5. Once the function C_α is found, Eq. 2.6 is the solution to the IVP.

Three approaches will be used in this dissertation to solve the receptivity problem. Optimal perturbation theory is widely used in the literature and will serve as the starting point for the present work. Multimode decomposition of an arbitrary perturbation will be used to contrast optimal perturbations with physically realized perturbations, and a linearized receptivity calculation will be used assuming the limit of small roughness. These three methods are described in detail below.

1. Optimal Perturbation Theory

Due to the difficulty in analyzing the receptivity process in transient growth, optimal disturbance theory has been used extensively to investigate transient growth phenomena[26, 27, 28, 29, 45, 30] as well as secondary effects of transiently growing perturbations[33, 11]. Because the distribution of amplitudes amongst the continuous spectrum modes is not known, optimal disturbance theory calculates the modal distribution that produces the *most* energy growth over a given interval. This approach has yielded insight into the physical mechanisms that drive transient growth, and focused efforts toward the types of disturbances that produce appreciable transient growth: stationary, spanwise-periodic, streamwise vortices.

Two approaches to this computation exist in the literature. Butler and Farrell[26] formulate an eigenvalue problem by taking a variational calculus approach, whereas Schmid and Henningson[28] use a singular value decomposition (SVD) of a factored energy matrix. More physical insight can be gained from the variational calculus approach, and then it will be shown to be equivalent to the SVD method.

To deal with the problem numerically, the integrals in Eq. 2.6 must be discretized to a sum over a range of α. This is accomplished by discretizing κ_j, giving mode shapes $\hat{\phi}_{\alpha_j}$. The functions of a complex variable must be be enumerated, i.e., $C_\alpha \rightarrow C_{\alpha_j}$. Given a suitable discretization, an arbitrary velocity field can be expanded as a sum of eigenmodes $\hat{\phi}_{\alpha_j}$ for a given β and ω:

$$\phi(x,y) = \sum_{j=1}^{N} C_{\alpha_j} \hat{\phi}_{\alpha_j}(y) e^{i\alpha_j x} \,. \tag{2.7}$$

There are an unlimited number of ways to discretize the continuous spectrum in order to generate the necessary basis functions to represent an initial velocity profile as in Eq. 2.7. This characteristic of the continuous spectrum makes the choice of basis functions somewhat ambiguous, as integral methods can be used to generate an eigenfunction at any point on any branch of the continuous spectrum. However, there are distinct advantages to using the discretization of the continuous spectrum that is obtained naturally from a Chebyshev pseudospectral technique (See Appendix B), with a factorization-based eigenvalue algorithm (e.g. QZ), to solve the eigenvalues problem, Eq. 2.3. First, this discretization handles multiple continuous spectrum branches without difficulty. Second, this discretization provides modes that have $\hat{u}, \hat{v}, \hat{w} = 0$ at the top of the computational domain (though $|\partial \hat{u}/\partial y| \neq 0$). This can be combined with quadrature methods (see Appendix B) to ensure spectral accuracy and overcome the fact that the basis functions are not square-integrable in the wall-normal direction. The distribution of the eigenvalues along the continuous spectrum can be controlled by varying the maximum height of the computational domain, as well as the mapping from the Chebyshev domain to the physical domain, and the density of eigenvalues can be controlled by varying the number of Chebyshev polynomials.

The goal is to find the combination of C_{α_j} that produce the most energy growth over a specified x interval. To this end let $\mathcal{E}$ be an energy operator:

$$\mathcal{E}[\phi,\phi]_x = \int_0^\infty \bar{u}(x)u(x) + \bar{v}(x)v(x) + \bar{w}(x)w(x)dy = \int_0^\infty |\phi^{(1)}|^2 + |\phi^{(3)}|^2 + |\phi^{(5)}|^2 dy \tag{2.8}$$

where the overbars mean complex conjugation, and the parenthetical indices are the vector components. If x_* is the optimization location, the optimal perturbation should solve the maximization problem:

$$\max \mathcal{E}[\phi,\phi]_{x_*} \tag{2.9}$$

subject to the constraint

$$\mathcal{E}[\phi,\phi]_{x_0} = 1\,. \tag{2.10}$$

That is, the initial perturbation should have unit energy and produce the largest response at x_*. This maximization problem can be formulated as a variational calculus problem. Let $\mathcal{J}$ be the objective function, the variational problem is then:

$$\mathcal{J} = \mathcal{E}[\phi,\phi]_{x_*} + \lambda_0(\mathcal{E}[\phi,\phi]_{x_0} - 1)\,. \tag{2.11}$$

Using Eq. 2.7, the unknowns in Eq. 2.11 are the amplitude coefficients C_{α_j}. The operator form can be replaced with a linear algebraic form by substituting the modal representation from Eq. 2.7. Let $\mathbf{C}_\alpha$ be the vector of amplitude coefficients C_{α_j}, $\boldsymbol{\phi}_\alpha$ be the vector of eigenmodes ϕ_{α_j}, and $\mathbf{R} = \mathrm{diag}(\exp i\alpha_j(x - x_0))$ a diagonal matrix that governs the evolution of each mode in the x direction. Then each component of Eq. 2.7 can be rewritten:

$$\phi^{(k)}(x,y) = \boldsymbol{\phi}_\alpha^{(k)T}\mathbf{R}\mathbf{C}_\alpha\,. \tag{2.12}$$

Using the matrix-vector form, the energy operator can be expanded:

$$\mathcal{E}[\phi,\phi]_x = \mathbf{C}_\alpha^H\mathbf{R}^H\left\{\int_0^\infty \bar{\boldsymbol{\phi}}_\alpha^{(1)}\boldsymbol{\phi}_\alpha^{(1)T} + \bar{\boldsymbol{\phi}}_\alpha^{(3)}\boldsymbol{\phi}_\alpha^{(3)T} + \bar{\boldsymbol{\phi}}_\alpha^{(5)}\boldsymbol{\phi}_\alpha^{(5)T}\,dy\right\}\mathbf{R}\mathbf{C}_\alpha \tag{2.13}$$

where $\mathbf{R} = \mathbf{R}(x)$, and ^{H} is the complex-conjugate transpose. Using the definition of the energy operator, the middle term becomes a matrix $\mathbf{E}$ whose terms are defined:

$$E_{ij} = \mathcal{E}[\phi_{\alpha_i},\phi_{\alpha_j}]\,. \tag{2.14}$$

Once the mode shapes are computed, this matrix is completely known. This gives a problem solely in terms of the unknown receptivity coefficients, which reduces the energy operator definition to:

$$\mathcal{E}[\phi,\phi]_x = \mathbf{C}_\alpha^H\mathbf{R}^H\mathbf{E}\mathbf{R}\mathbf{C}_\alpha\,. \tag{2.15}$$

Using this definition, and the fact that $\mathbf{R} = \mathbf{I}$ at the initial condition, the variational problem, Eq. 2.11, can be rewritten:

$$\mathcal{J} = \mathbf{C}_\alpha^H\mathbf{R}^H\mathbf{E}\mathbf{R}\mathbf{C}_\alpha + \lambda_0(\mathbf{C}_\alpha^H\mathbf{E}\mathbf{C}_\alpha - 1)\,. \tag{2.16}$$

The optimization conditions are found by setting the derivative of $\mathcal{J}$ with respect to the unknown coefficients and the Lagrange multiplier to zero. Setting $\partial\mathcal{J}/\partial\lambda_0 = 0$ gives the normalization condition. The partial with respect to the unknowns gives:

$$\frac{\partial\mathcal{J}}{\partial\mathbf{C}_\alpha} = \mathbf{R}^H\mathbf{E}\mathbf{R}\mathbf{C}_\alpha + \lambda_0\mathbf{E}\mathbf{C}_\alpha = 0\,. \tag{2.17}$$

Eq. 2.17 is an eigenvalue problem for the unknown coefficients $\mathbf{C}_\alpha$, and the eigenvalue λ_0 gives the growth rate. This is similar to the formulation given in Ref. [26].

An alternative formulation is to note that the matrix representation of the energy operator can be factored. Because $\mathbf{E}$ is symmetric and positive definite it can be factored $\mathbf{E} = \mathbf{F}^H\mathbf{F}$. With this substitution, the energy amplification can be written as the standard vector-norm:

$$G(x_*) = \frac{\mathcal{E}[\phi,\phi]_{x_*}}{\mathcal{E}[\phi,\phi]_{x_0}} = \frac{\|\mathbf{F}\mathbf{R}\mathbf{C}_\alpha\|^2}{\|\mathbf{F}\mathbf{C}_\alpha\|^2}\,. \tag{2.18}$$

Without loss of generality the initial condition is constrained to have unit energy, and this becomes the maximization problem

$$\max_{\|\mathbf{F}\mathbf{C}_\alpha\|=1} \|\mathbf{F}\mathbf{R}\mathbf{C}_\alpha\|^2 \tag{2.19}$$

Noting that by definition the two-norm of a matrix $\mathbf{A}$ is:

$$\|\mathbf{A}\|_2^2 = \max_{\|x\|=1} \|\mathbf{A}x\|^2 \tag{2.20}$$

then $\mathbf{F}\mathbf{C}_\alpha = x \longrightarrow \mathbf{C}_\alpha = \mathbf{F}^{-1}x$. This replacement of $\mathbf{C}_\alpha$ means the optimization problem is equivalent to finding the two-norm of the matrix:

$$G(x_*) = \max_{\|x\|=1} \|\mathbf{F}\mathbf{R}\mathbf{F}^{-1}x\|^2 = \|\mathbf{F}\mathbf{R}\mathbf{F}^{-1}\|_2^2 \tag{2.21}$$

The two-norm in Eq. 2.21 is found via an SVD and represents the evolution of the perturbation kinetic energy. The SVD gives the factorization:

$$\mathbf{F}\mathbf{R}\mathbf{F}^{-1} = \mathbf{U}\boldsymbol{\Sigma}\mathbf{V}^{H} . \tag{2.22}$$

In this factorization $\mathbf{U}$ and $\mathbf{V}$ are unitary matrices, and $\boldsymbol{\Sigma}$ is diagonal. Physically, this represents the relation between the input $\mathbf{V}$ and the output $\mathbf{U}$, scaled by a factor from $\boldsymbol{\Sigma}$ due to the spatial evolution. The largest singular value, $\sigma_1 = \Sigma_{11}$ gives the optimal amplification, and the initial amplitude distribution can be found from the associated right singular vector $C_{\alpha_j} = \mathbf{F}^{-1}v_1$. This is the approach taken by Schmid and Henningson[28]. The advantage is that both the input and output perturbations are known after the SVD is calculated, and the SVD is numerically more tractable to compute. The disadvantage is the one-time cost of the Cholesky factorization of $\mathbf{E}$.

The solution of Eq. 2.21 provides the first base flow of interest. The optimal perturbation is computed for a zero-pressure-gradient, flat-plate boundary layer. Eq. 2.3 is solved using a Chebyshev pseudospectral method based on Ref. [46]. Three hundred polynomials are used on a grid with $y_{\max} = 45$ where y has been non-dimensionalized with δ, the Blasius scaling, in all computations and figures. Further details of the code can be found in Appendix B, and the specific conditions used are given in the results sections.

2. Multimode Decomposition

Optimal theory provides one solution to the receptivity problem. However, all transiently growing disturbances that are generated by physical roughness have been found to be sub-optimal[14, 35]. The collection of modal amplitudes that create transient growth are quantitatively and qualitatively different than those that make up the optimal disturbances[47]. This discrepancy between optimal predictions and physical realization is especially important in the context of transient growth. While a great deal of progress has been made in the study of modal instabilities even without detailed receptivity information, the divide between receptivity and linear theory is more challenging in the case of transient growth.

The fact that optimal calculations do not match what is physically realized in an experiment is not surprising. In the traditional modal growth scenario, broadband forcing is channeled into a specific mode shape with a fixed growth rate. The resulting mode then grows to rise above the decaying background noise and becomes the dominant flow feature. By contrast, a transiently growing perturbation relies on details of the initial disturbance generator to determine the growth rate. Therefore, the optimal perturbation does not arise naturally out of broadband forcing, in fact it would likely not appear at all. Optimal calculations provide proof of the *existence* of transient growth in general, but cannot show what will be seen in a specific physical situation. Unlike modal growth, the optimality/growth rate of a disturbance and its likelihood of occurring are not directly related.

A necessary first step toward analyzing physically realizable, sub-optimal disturbances is to find continuous spectrum amplitude distributions of measured disturbances. Once these sub-optimal disturbances can be correctly characterized in terms of linear theory, models and correlations can be generated that take into account the differences between modal and non-modal mechanisms. The mathematical formulation necessary for decomposing an arbitrary perturbation into its continuous spectrum modes has been put forward by Tumin[42], but has yet to find widespread adoption. This multimode decomposition was initially employed on an example problem (an optimal perturbation in Ref. [42]) and by the same author in a two-dimensional hypersonic boundary layer[48]. Prior to the work of this dissertation, the method had yet to be used to confirm whether measured transient growth is indeed a linear phenomenon, or to compare the amplitude distribution to optimal or linearized receptivity approaches.

Multimode decomposition is used to calculate this amplitude distribution for a physically-realized transiently-growing perturbation for the first time. Further, one of the reasons for the limited use of this technique despite its potential for dealing with a large number of complicated stability problems has been the lack of a dissertation-length derivation and explanation of the method. This section includes a detailed derivation of the necessary bi-orthogonality relationships that underlie multimode decomposition. In addition, the normalization functions, that do not appear in the existing literature, are given explicitly.

a. Biorthogonal Eigenfunction System

In order to extract the amplitude function from an arbitrary initial condition a set of functions must be constructed that are orthogonal to the eigenfunction basis constructed by solving Eq. 2.3. This adjoint basis will be distinct from the set $\hat{\phi}_\alpha$ because the operator $\mathcal{L}_{OS}$ is not self-adjoint. The adjoint solution is constructed by multiplying Eq. 2.3 by an adjoint vector function $\hat{\psi}$ and integrating with respect to y:

$$\int_0^\infty \hat{\psi}^T \left(\frac{\partial \hat{\phi}}{\partial y} - \mathcal{L}_{OS} \hat{\phi} \right) dy = 0\,. \tag{2.23}$$

Integrating by parts to transfer the derivative gives:

$$[\mathrm{BC}] - \int_0^\infty \hat{\phi}^T \left(\frac{\partial \hat{\psi}}{\partial y} + \mathcal{L}_{OS}^T \hat{\psi} \right) dy = 0\,. \tag{2.24}$$

Setting the terms inside the parentheses and the boundary conditions equal to zero constitutes the adjoint equation.

$$-\frac{\partial \hat{\psi}}{\partial y} = \mathcal{L}_{OS}^T \hat{\psi} \tag{2.25}$$

The boundary conditions are selected to eliminate the boundary terms in Eq. 2.24, giving $\hat{\psi}^{(2)} = \hat{\psi}^{(4)} = \hat{\psi}^{(6)} = 0$ at $y = 0$, and the total perturbation must go to zero far from the wall. The same boundedness conditions apply in the freestream on the individual adjoint modes, $|\hat{\psi}_\alpha| < \infty$ as $y \to \infty$. This presents some complication as both the adjoint and direct modes are not square integrable when considered alone. This will be addressed below when constructing the bi-orthogonal system. The eigenvalues of $\mathcal{L}_{OS}^T$ are the same as Eq. 2.4, and the basis functions are found from the eigenvectors in Appendix A.

The goal is to construct a bi-orthogonality relationship between eigenfunctions of different values of α. Unfortunately, α appears nonlinearly in the operator $\mathcal{L}_{OS}$. To derive the bi-orthogonality condition, the vector of unknowns is augmented, $\Phi = [\hat{u}, \partial\hat{u}/\partial y, \hat{v}, \hat{p}, \hat{w}, \partial\hat{w}/\partial y, \partial\hat{u}/\partial x, \partial\hat{v}/\partial x, \partial\hat{w}/\partial x]^T$, and the adjoint is the correspondingly augmented Ψ. This allows the operator $\mathcal{L}_{OS}$ to be split into two components that are independent of α:

$$\frac{\partial\Phi}{\partial y} = \mathbf{A_1}\Phi + i\alpha\mathbf{A_2}\Phi \tag{2.26}$$

where the matrix components are given in Appendix A.

From this augmented definition a bi-orthogonality condition can be derived. Let Φ_κ be a modal solution to Eq. 2.3, where κ parameterizes the continuous spectrum of α. Let $\Psi_{\kappa'}$ be a solution to Eq. 2.25 for a different eigenvalue α' converted into augmented form. Inner products with respect to the continuous spectrum modes are improper in the sense that the integrals do not converge. There are two methods to handle this difficulty. Either the inner products can be weighted with a term to render them convergent, or, more physically, the integrals can be considered in the limit of a narrow wave-packet. For notational simplicity this means:

$$\Phi_\kappa = \int_{\kappa-\epsilon}^{\kappa+\epsilon} \Phi_k dk\,, \quad \epsilon \to 0\,. \tag{2.27}$$

The wavepacket approach will be used here. First, it will be assumed that the narrow wave-packet limit renders the integrals well-behaved for the purposes of deriving the orthogonality relationship. This will be validated when showing the normalization conditions.

Consider the inner product of two modes of differing wavenumber by multiplying Eq. 2.26 by $\Psi_{\kappa'}$ and integrating:

$$\int_0^\infty \Psi_{\kappa'}^T \frac{\partial \Phi_\kappa}{\partial y}\, dy = \int_0^\infty \Psi_{\kappa'}^T \mathbf{A_1} \Phi_\kappa \, dy + i\alpha \int_0^\infty \Psi_{\kappa'}^T \mathbf{A_2} \Phi_\kappa \, dy \,. \tag{2.28}$$

Integrating by parts and using the definition of the adjoint Eq. 2.25 and its boundary conditions gives:

$$\int_0^\infty \left[\left(\mathbf{A_1}^T \Psi_{\kappa'}\right)^T \Phi_\kappa + i\alpha' \left(\mathbf{A_2}^T \Psi_{\kappa'}\right)^T \Phi_\kappa \right] dy = \int_0^\infty \Psi_{\kappa'}^T \mathbf{A_1} \Phi_\kappa dy + i\alpha \int_0^\infty \Psi_{\kappa'}^T \mathbf{A_2} \Phi_\kappa dy \,. \tag{2.29}$$

The first term vanishes identically, leaving:

$$i(\alpha - \alpha') \int_0^\infty \Psi_{\kappa'}^T \mathbf{A_2} \Phi_\kappa \, dy = 0 \tag{2.30}$$

For two different continuous spectrum modes, $\alpha \neq \alpha'$, Eq. 2.30 gives the bi-orthogonality condition. For $\alpha = \alpha'$, the integral must be shown to be convergent and the normalization constant (Q_α) found such that:

$$\int_0^\infty \Psi_{\kappa'}^T \mathbf{A_2} \Phi_\kappa \, dy = Q_\alpha \delta(\kappa - \kappa') \,. \tag{2.31}$$

The values for the normalization constants, and analysis of the convergence of the integrals will be given in the next subsection. There is a one-to-one correspondence between the parameter κ and the eigenvalue α and thus the α and κ subscripts are interchangeable. The decomposition formulas can be expressed in terms of α to give more physical meaning, but κ is used here when describing convergence behavior.

Once the values for Q_α are found, the decomposition of an arbitrary disturbance can be formulated. Because the direct modes are orthogonal to every adjoint mode except the one with common eigenvalues, multiplying an arbitrary profile by an adjoint and integrating returns the amplitude C_α of the particular mode. The decomposition can be expressed:

$$C_\alpha = \frac{1}{Q_\alpha} \int_0^\infty \Psi_\alpha^T \mathbf{A_2} \Phi_0 \, dy \tag{2.32}$$

where Φ_0 is the full disturbance data. This is the biorthogonal decomposition relationship. However this is still working in the 9x9 system, by manipulating Eq. 2.32 the 9x9 system can be simplified back to the 6x6 system in this way (see Appendix A):

$$C_\alpha = \frac{-i}{Q_\alpha} \int_0^\infty \frac{\partial \mathcal{L}_{OS}}{\partial \alpha} \hat{\phi}(x_0) \cdot \hat{\psi}_\alpha \, dy \, . \tag{2.33}$$

b. Normalization

For the continuous spectrum of the Orr–Sommerfeld/Squire system, the normalization of the bi-orthogonal eigenfunction system is non-trivial. For a set of discrete modes the normalization can be found numerically such that Eq. 2.30 is equal to one, and the functions are orthonormal. Because the solutions $\hat{\phi}_\alpha$ and $\hat{\psi}_\alpha$ are not square integrable, some analysis is necessary to compute Q_α.

Expressed in the reduced sixth-order notation, the normalization condition is:

$$Q_\alpha \delta(\alpha - \alpha') = -i \int_0^\infty \frac{\partial \mathcal{L}_{OS}}{\partial \alpha} \hat{\phi}_\alpha \cdot \hat{\psi}_{\alpha'} \, dy \tag{2.34}$$

and the value for Q_α must be found for an arbitrary normalization of the adjoint and direct modes. To find this, first note that as $y \to \infty$; $\hat{\phi}, \hat{\psi} \propto \exp(\pm i\kappa y)$. As before a narrow wave-packet is assumed. The integrals can be split, letting δ_1 be the top of the boundary layer:

$$\begin{aligned}\int_0^\infty \hat{\psi}_{\kappa'} \cdot \left(\int_{\kappa-\epsilon}^{\kappa+\epsilon} \frac{\partial \mathcal{L}_{OS}}{\partial \alpha} \hat{\phi}_k \, dk \right) \, dy = &\int_0^{\delta_1} \hat{\psi}_{\kappa'} \cdot \left(\int_{\kappa-\epsilon}^{\kappa+\epsilon} \frac{\partial \mathcal{L}_{OS}}{\partial \alpha} \hat{\phi}_k \, dk \right) \, dy \\ &- \int_0^{\delta_1} {}_\infty\hat{\psi}_{\kappa'} \cdot \left(\int_{\kappa-\epsilon}^{\kappa+\epsilon} \frac{\partial \mathcal{L}_{OS}}{\partial \alpha} {}_\infty\hat{\phi}_k \, dk \right) \, dy \\ &+ \int_0^{\infty} {}_\infty\hat{\psi}_{\kappa'} \cdot \left(\int_{\kappa-\epsilon}^{\kappa+\epsilon} \frac{\partial \mathcal{L}_{OS}}{\partial \alpha} {}_\infty\hat{\phi}_k \, dk \right) \, dy \qquad (2.35)\end{aligned}$$

Where the ∞ terms are the asymptotics evaluated outside the boundary layer. The first two integrals on the right hand side vanish as $\epsilon \to 0$ because the integrals are finite. The last integral does not vanish, though the terms are all known and constant outside the boundary layer. Pulling these constants out leaves integrals of the following type:

$$\int_0^\infty e^{-i\kappa' y} \int_{\kappa-\epsilon}^{\kappa+\epsilon} e^{iky} \, dk \, dy = 2 \int_0^\infty e^{i(\kappa-\kappa')y} \frac{\sin \epsilon y}{y} \, dy \, . \qquad (2.36)$$

Expanding in terms of trigonometric functions, the integrals can be found in Ref. [42]. The imaginary part of Eq. 2.36 gives:

$$2i \int_0^\infty \frac{\sin\left[(\kappa - \kappa')y\right] \sin \epsilon y}{y} \, dy = i \log \left| \frac{\epsilon + (\kappa - \kappa')}{\epsilon - (\kappa - \kappa')} \right| \qquad (2.37)$$

which is zero for $\kappa = \kappa'$. The real part of Eq. 2.36 gives:

$$2 \int_0^\infty \frac{\cos\left[(\kappa - \kappa')y\right] \sin \epsilon y}{y} \, dy = \begin{cases} \pi, & (\kappa - \kappa') < \epsilon \\ 0, & (\kappa - \kappa') > \epsilon \end{cases} \qquad (2.38)$$

As $\epsilon \to 0$ this integral converges to a single point for $\kappa = \kappa'$, and all integrals of this type tend to $\pi\delta(\kappa - \kappa')$ (this also demonstrates the convergence necessary in the previous section). Computing Q_α then reduces to finding the coefficients of the freestream asymptotic solutions.

On the vorticity branch there are six asymptotic solutions, but only four are non-zero far from the wall. A solution consists of a sum of any three, and thus four different combinations are possible. However, two of the combinations are simply complex conjugates of the other two. The combinations define the A and B branches. The sum of these components make up the continuous spectrum mode in the freestream. Let ζ be the coefficients of the freestream modal components of $\hat{\phi}$ and ξ the coefficients of $\hat{\psi}$, then:

$$
\begin{aligned}
{}_{\infty}\hat{\phi}_{\alpha,A} &= \zeta_3 {}^{(3)}_{\infty}\hat{\phi}_\alpha e^{\lambda_3 y} + \zeta_5 {}^{(5)}_{\infty}\hat{\phi}_\alpha e^{\lambda_5 y} + \zeta_6 {}^{(6)}_{\infty}\hat{\phi}_\alpha e^{\lambda_6 y} && (2.39)\\
{}_{\infty}\hat{\phi}_{\alpha,B} &= \zeta_3 {}^{(3)}_{\infty}\hat{\phi}_\alpha e^{\lambda_3 y} + \zeta_4 {}^{(4)}_{\infty}\hat{\phi}_\alpha e^{\lambda_4 y} + \zeta_6 {}^{(6)}_{\infty}\hat{\phi}_\alpha e^{\lambda_6 y} && (2.40)\\
{}_{\infty}\hat{\psi}_{\alpha,A} &= \xi_3 {}^{(3)}_{\infty}\hat{\psi}_\alpha e^{\lambda_3 y} + \xi_5 {}^{(5)}_{\infty}\hat{\psi}_\alpha e^{\lambda_5 y} + \xi_6 {}^{(6)}_{\infty}\hat{\psi}_\alpha e^{\lambda_6 y} && (2.41)\\
{}_{\infty}\hat{\psi}_{\alpha,B} &= \xi_3 {}^{(3)}_{\infty}\hat{\psi}_\alpha e^{\lambda_3 y} + \xi_4 {}^{(4)}_{\infty}\hat{\psi}_\alpha e^{\lambda_4 y} + \xi_6 {}^{(6)}_{\infty}\hat{\psi}_\alpha e^{\lambda_6 y} && (2.42)
\end{aligned}
$$

where the left indices correspond to the different freestream vectors associated with λ_{3-6}. From the definition of the continuous spectrum, $\lambda_{4,6} = -\lambda_{3,5} = i\kappa$, and from the analysis of the asymptotic solutions the only terms contributing in the dot product are those with opposite signs associated with $i\kappa$. Substituting these definitions back into the normalization formula gives:

$$Q_\alpha = -i\pi \frac{\partial \mathcal{L}_{OS}^{(ij)}}{\partial \alpha}\left(\zeta_3 {}^{(3)}_{\infty}\hat{\phi}_\alpha^{(j)} \xi_6 {}^{(6)}_{\infty}\hat{\psi}_\alpha^{(i)} + \zeta_5 {}^{(5)}_{\infty}\hat{\phi}_\alpha^{(j)} \xi_6 {}^{(6)}_{\infty}\hat{\psi}_\alpha^{(i)} + \zeta_6 {}^{(6)}_{\infty}\hat{\phi}_\alpha^{(j)} \xi_3 {}^{(3)}_{\infty}\hat{\psi}_\alpha^{(i)} + \zeta_6 {}^{(6)}_{\infty}\hat{\phi}_\alpha^{(j)} \xi_5 {}^{(5)}_{\infty}\hat{\psi}_\alpha^{(i)}\right) \tag{2.43}$$

for branch A, where the summation convention is used to express this compactly. The branch B normalization constant is found in a similar manner.

c. Experimental Decomposition

Experimental data is necessary to advance understanding of complex roughness. This demands a method be developed for extracting the receptivity information when only the streamwise velocity disturbance can be obtained. Hotwire anemometry can be used to obtain detailed measurements of the streamwise perturbation in the wake of realistic roughness elements, but cannot obtain the spanwise and wall-normal velocity with accuracy necessary to perform a multimode decomposition. Further, spatially distributed steady pressure perturbations are essentially unmeasurable. The result is that in the initial condition vector, the streamwise velocity component and its derivative can be used, but the unmeasured components $\hat{v}$, $\hat{w}$ and $\hat{p}$ must be left as sums of the eigenmodes and unknown coefficients[49]:

$$\hat{\phi}(x_0) = \left[\hat{u}_0, D\hat{u}_0, \int_\alpha C_\alpha \hat{v}_\alpha, \int_\alpha C_\alpha \hat{p}_\alpha, \int_\alpha C_\alpha \hat{w}_\alpha, \int_\alpha C_\alpha D\hat{w}_\alpha\right]^T . \tag{2.44}$$

The integrals are discretized into sums, and substituted into Eq. 2.33. This yields a system of algebraic Eq. in C_α that is made non-singular by the presence of u_0. This gives a linear system in the amplitude coefficients.

$$\mathbf{M}_{j\alpha} C_\alpha = F_j \tag{2.45}$$

where

$$\mathbf{M}_{j\alpha} = \int_0^\infty \left[-\hat{\psi}_j^{(2)} p_\alpha + \hat{\psi}_j^{(4)}(2\alpha/Re + iU)v_\alpha - \hat{\psi}_j^{(6)}(iURe + 2\alpha)w_\alpha\right] dy + iQ_\alpha \delta_{\alpha j} \tag{2.46}$$

and

$$F_j = \int_0^\infty \left[\hat{\psi}_j^{(2)}(iURe + 2\alpha)u_0 - i\hat{\psi}_j^{(3)} u_0 - \hat{\psi}_j^{(4)}(i/Re)Du_0\right] dy\,. \tag{2.47}$$

I is the identity matrix.

Formulating Eq. 2.45 without $\hat{v}$, $\hat{w}$ and $\hat{p}$ greatly reduces the information present in the initial data. This is especially true given that generic “streaky” structures (i.e., streamwise u' disturbances) are ubiquitous in boundary layers. Attempting a decomposition using only streamwise velocity information is not successful because the amplitude distribution that produces a streak is not unique. Specifically, the underlying streamwise vortex dynamics that drive the transiently growing perturbation, the "lift-up" forcing, are not present, making a growing streak and a decaying streak indistinguishable. However, although the underlying spanwise and wall-normal velocity cannot be directly measured, their effect on the flow can be. The impact of the underlying streamwise vortex can be seen indirectly in how the streak evolves downstream. Therefore, using multiple streamwise locations in the decomposition can build the necessary physics back into the numerical solution.

To build multiple streamwise locations into the computation, $\mathbf{M}_{j\alpha}$ is expanded from an $N \times N$ system to an $N \times KN$ system, where K is the number of streamwise stations where hotwire measurements have been obtained. Attempting to solve this overdetermined system utilizing a general least squares approach fails due to the fact that Eq. 2.45 remains ill-posed. It is ill-posed in the sense that small changes in the vector of known data F_j can produce large changes in the modal amplitudes C_α, both due to the inherent stiffness of the OSS system and the multiple possible solutions that constitute a streamwise streak. This sensitivity is especially problematic due to inherent measurement uncertainty. To remedy this ill-posedness, a regularization method based on Tikhonov[50] is utilized. A set of regularization norms and an algorithm for solving Eq. 2.45 that minimizes the error in the measured velocity profiles is developed. This procedure produces a unique solution with no information other than experimentally obtained, streamwise velocity profiles.

The approach is to minimize a functional, $\mathcal{M}$, that contains both the general least-squares functional, as well as one or more "regularizing" functionals, that serve to constrain the magnitude and smoothness of the solutions. These additional constraints are weighted by arbitrary constants, γ_1 and γ_2. In the present work $\mathcal{M}$ is defined:

$$\mathcal{M} = ||\mathbf{M}_{j\alpha} C_\alpha - F_j||^2 + \gamma_1 ||C_\alpha||^2 + \gamma_2 ||\mathbf{\Gamma} C_\alpha||^2 \tag{2.48}$$

In Eq. 2.48, the first norm represents the standard least-squares solution. This least squares term can also expanded to include weighted least squares to account for the different levels of measurement uncertainty at different streamwise locations. In the present work, weighted least squares is used to allow for locations with relatively uncertain measured $\hat{u}$ values to be prioritized less than measurement locations that are known with better accuracy.

The second norm attempts to minimize the overall vector norm of the solution. Because the modes are non-orthogonal, substantial cancellation can occur between modes when solving Eq. 2.45. This cancellation allows for solutions with arbitrarily large amplitudes, that are then cancelled by equally large modes that are nearly out of phase. Controlling the vector norm of the solution is a means of biasing the computation to prefer setting two modes to zero, where appropriate, as opposed to allowing arbitrarily large amplitudes and opposite phase.

The third norm exploits the fact that C_α must be a smooth function. $\mathbf{\Gamma}$ is a matrix representation of the derivative operation with respect to α, that acts as a penalty for discontinuities in C_α. Thus, this regularizer controls the realizability of the hypothetical disturbance input.

This $\mathcal{M}$ functional is strongly convex[50], so a minimum is found by equating the first derivative of $\mathcal{M}$ to zero. A regularized equation is then obtained:

$$C_\alpha = \left(\mathbf{M}_{j\alpha}^H \mathbf{M}_{j\alpha} + \gamma_1 \mathbf{I} + \gamma_2 \mathbf{\Gamma}^H \mathbf{\Gamma}\right)^{-1} \mathbf{M}_{j\alpha}^H F_j \tag{2.49}$$

Eq. 2.49 can give C_α in a more tractable way than inverting Eq. 2.45 directly.

The constants γ_1 and γ_2 are adjusted to provide the best solution. Some theoretical techniques for setting these coefficients are given for simple, model problems in Ref. [50]. However, for the present case with multiple regularizers and complex inputs the physical knowledge of the system can be used to optimize γ_1 and γ_2.

The following algorithm is used to optimize the regularization coefficients. First, the total energy of the experimental data is calculated. The disturbance profiles are integrated in y to find the energy as a function of x, and then integrated in x to give a single total energy. This number is then used to normalize the total energy of the input data to unity. The decomposition is performed for a range of γ_1 and γ_2 and the resulting output is also scaled to have unit total energy. This rescaling both helps numerically by making the total disturbance energy $\mathcal{O}(1)$ and helps account for error introduced from the regularization. That is, by penalizing the overall vector norm, the regularized solution tends to give a slightly lower total energy than the experimental data. However, since the problem is linear, rescaling this solution back to unit energy is an equally valid solution. Once rescaled, the rms error is computed for every $\hat{u}$ velocity profile and summed over all x locations available. The combination of parameters that give the minimum error is then taken as the regularized solution. Once this "best" regularized solution is obtained, the continuous spectrum solution and experimental data are scaled back to the physically appropriate values. This procedure produces a unique solution with no information other than experimentally obtained, streamwise velocity profiles. The optimal parameters will be given in the results section.

3. Linear Receptivity

Tumin and Reshotko[51] use the biorthogonal eigenfunction system to compute the receptivity function for small amplitude surface roughness. This is accomplished by assuming the roughness element can be linearized, and the geometric boundary condition of the roughness height can be replaced with an equivalent slip boundary condition on the streamwise velocity. Letting the roughness height be $y = hf(x, z)$, and expanding the roughness geometry in a Taylor series about $y = 0$, gives the boundary condition:

$$u_w = -hf(x,z)\frac{\partial U}{\partial y}\,. \tag{2.50}$$

The contribution to each eigenfunction is computed by taking the Fourier transform of the boundary condition:

$$\hat{u}_w(\alpha) = \frac{-h}{2\pi}\frac{\partial U}{\partial y}\int_{-\infty}^{\infty}\int_{-\infty}^{\infty} f(x,z)e^{i\alpha x+i\beta z}\,dx\,dz\,. \tag{2.51}$$

Eq. 2.33 gives the orthogonality condition for obtaining the amplitude coefficients; however, not all boundary conditions vanish in the orthogonality relationship because of the non-Dirichlet conditions created by the roughness. That is, the right hand side of Eq. 2.30 is not zero. Instead the right-hand side is the product of the adjoint and the streamwise velocity component at the wall:

$$\int_0^{\infty}\frac{\partial \mathcal{L}_{OS}}{\partial \alpha'}\hat{\phi}_{\alpha'}\cdot\hat{\psi}_{\alpha}\,dy = \frac{\hat{u}_w(\alpha')\psi_{\alpha}^{(1)}|_0}{i(\alpha-\alpha')}\,. \tag{2.52}$$

Integrating over all α' gives the contribution for all wavenumbers (using the residue theorem):

$$C_{\alpha} = \int_{-\infty}^{\infty}\frac{e^{i(\alpha'-\alpha)x}\hat{u}_w(\alpha')\psi_{\alpha}^{(1)}|_0}{i(\alpha-\alpha')Q_{\alpha}}d\alpha' = -\frac{2\pi}{Q_{\alpha}}\hat{u}(\alpha)\psi_{\alpha}^{(1)}|_0 \tag{2.53}$$

Ref. [51] does not find transient growth for the cylindrical roughness case, which is consistent with the receptivity process being non-linear. The receptivity function results here can be contrasted with those computed using optimal perturbation and decomposition methods to see why this is the case.

C. Numerical Tools

Several numerical tools are developed to carry out the multimode decomposition and optimal growth computations outlined in this section. Some details of the codes can be found in the Appendix B.

Orr–Sommerfeld Solver (Algebraic) solves spatial or temporal Orr–Sommerfeld/ Squire system using Chebyshev collocation to discretize the eigenvalue problem, and QZ factorization to solve the resulting linear algebra problem.

Orr–Sommerfeld Solver (Integral) solves spatial Orr–Sommerfeld/Squire system for continuous spectrum modes using variable stepping 7th-8th order Runge-Kutta. This code stores the modal asymptotic information necessary to construct the normalization constants.

Spatial Optimal Solver computes optimal transient growth solutions given a collection of continuous spectrum modes from the algebraic Orr–Sommerfeld solver, using both SVD and eigenvalue formulation.

Complete Data Multimode Decomposition Solver computes amplitude functions, C_α, given mode shapes and normalizations from the Orr–Sommerfeld solver, and initial profiles from DNS. Also provides post-processing of energy evolution, velocity profiles and error analysis. Also includes formulation for solving the decomposition problem when information about the pressure perturbations is absent.

Partial Data Regularization Solver computes amplitude functions, C_α, given mode shapes and normalizations from the Orr–Sommerfeld solver, and initial streamwise velocity measurements from experimental data.

CHAPTER III

DECOMPOSITION RESULTS

The previous chapter provides an extended derivation of the bi-orthogonality relationship for the continuous spectrum of the Orr–Sommerfeld/Squire system. Instead of an amplitude coefficient assigned to a particular mode, this bi-orthogonality relationship gives an amplitude function defined along the branch cuts in the complex α plane.

$$C_\alpha = \frac{-i}{Q_\alpha}\int_0^\infty \frac{\partial \mathcal{L}_{OS}}{\partial \alpha}\hat{\phi}(x_0)\hat{\psi}_\alpha \, dy \tag{2.33}$$

In this formulation, the spanwise wavenumber (β), and the Reynolds number (Re) are parameters, the integration over y eliminates the wall-normal dependence, and the amplitude function C_α is thus a function of α only. Similarly Q_α is a normalization function that also depends on α. $\hat{\phi}(x_0)$ is the vector of initial data (for a given β) and $\hat{\psi}_\alpha$ is the adjoint solution.

Once the amplitude functions have been calculated from the initial data using Eq. 2.33, the velocity and pressure profiles of the perturbation can be calculated at any location downstream.

$$\phi(x, y, \beta, \omega) = \sum_{A,B}\int_\Gamma C_\alpha \hat{\phi}_\alpha(y) e^{i\alpha x} d\alpha \tag{2.6}$$

The sum in Eq. 2.6 accounts for the contribution of the A and B branches of the continuous spectrum vorticity modes, and the integral over α accounts for total contribution along the branch.

The problem of interest is the now-canonical method of generating and measuring transient growth. A spanwise periodic array of circular cylinders in a flat plate boundary layer has been investigated extensively both experimentally[14, 15, 36, 35, 10, 37] and via direct numerical simulation (DNS)[38, 39, 40]. Fig. 6 shows a schematic of the setup. This chapter utilizes multimode decomposition to investigate two separate realizations of this setup and contrast the results to other receptivity approaches. First, a DNS of the cylinder array is analyzed. When DNS results are available, a complete description of the flow field is known. This allows Eq. 2.33 to be solved directly. The solution gives the receptivity of the boundary layer to cylindrical roughness elements. Second, experimental results with only streamwise velocity measurements are analyzed using the partial data method.

The case selected for analysis matches experiments by Ergin and White[52] and DNS by Rizzetta and Visbal[39]. The roughness-based Reynolds number is, nominally, $Re_k \approx 200$, and the cylinder spacing (λ_k) is three times the diameter (D). The Re_k value is relatively large, but still subcritical, meaning transient growth is observed but does not cause transition. The relevant dimensional and non-dimensional parameters are summarized in Table I. In this table, all quantities with subscript k indicate their values at the roughness location. Streamwise x locations are referenced to the virtual leading edge, which is 5 mm upstream of the physical leading edge.

TABLE I

Experimental and DNS Parameters

Parameter	Re' (m^{-1})	Re_k	x_k (mm)	λ_k (mm)	D (mm)	δ_k (mm)
Experiment	764×10^3	209	305	19	6.35	0.626
DNS	769×10^3	202	305	19	6.35	0.633

The continuous spectrum theory described above assumes parallel flow. However, over the domain of interest there is non-negligible boundary layer growth. To account for this when making comparison between theory and experimental/DNS results, an effective boundary layer scale and Reynolds number is employed. An average boundary layer scale is defined

$$\delta_{\text{avg}}(x) = \frac{1}{x - x_k} \int_{x_k}^{x} \delta(\xi) d\xi \tag{3.1}$$

Results from DNS and experiments are plotted against a non-dimensional streamwise location, $(x - x_k)/\delta_{\text{avg}}$. For the decomposed solutions, the value of δ used to calculate Re is the local value at the decomposition location $\delta = 0.668$ mm. In the case of the experimental decomposition, where multiple streamwise stations are used, there is no "local" δ to unambiguously set the Reynolds number for calculating the modes. To facilitate comparison, the same $Re = 510$ is used for the experimental and DNS decompositions. This corresponds to a δ_{avg} of roughly 375mm from the leading edge, near the center of the experimental measurement domain, and therefore is a reasonable balancing of non-parallel effects.

In this chapter, Section A analyzes the ability of linear theory to capture the complex behavior in the roughness wake. Section B contrasts the results of this receptivity calculation with optimal and linear receptivity approaches and highlights the significant differences. While the complete flow data makes solving Eq. 2.33 relatively straightforward, the computational expense of DNS leaves many situations where only experimental data is available. In this case, often only the streamwise component of the velocity is measurable. Section C validates the method of solving Eq. 2.45 when only certain components of the initial condition are available.

A. DNS Decomposition

A direct numerical simulation of flow over periodic cylinders in a flat plate boundary layer has been carried out by multiple authors[38, 39, 40]. The most detailed computation was performed by Rizzetta and Visbal (RV)[39], at the Air Force Research Lab. The computational cost of this simulation was substantial, utilizing 391 processors over the course of several months. Contrasting the results of RV to other DNS and experimental results reveals these computations and experiments are extremely sensitive to small changes in how the roughness elements are created, as well as the background disturbance environment. Achieving reliable and repeatable DNS results, even for this simplified geometry, remains a challenging task. Thus, extracting as much information from these simulations as possible is essential.

Within the limits of the parallel flow and linear disturbance assumptions, characterizing the flow response in terms of its continuous spectrum amplitude distribution offers many benefits. First, it represents a substantial data reduction, as a 3D, nonlinear, DNS can be reduced to one complex valued function, C_α, that contains information about *all* streamwise locations for a given β. This reduction provides the potential for future modeling of complex roughness features. Second, hope for developing a comprehensive understanding of "bypass" transition will rely on being able to make general statements across different geometries and flow conditions. The continuous spectrum analysis provides a quantitative way of expressing a DNS result that makes this possible. Further, the growth rate and distribution of C_α can be contrasted with previous theoretical results from both optimal and linear receptivity calculations. This gives a quantitative assessment of how effectively different geometries act as receptivity sources. Finally, a demonstration that perturbations evolve linearly after a small streamwise distance would substantially reduce computational time and make parametric studies possible as only a limited amount of the downstream evolution would need to be capture by the DNS.

When the results of both the DNS and the experiment are Fourier transformed in the spanwise direction, the disturbance energy is concentrated initially in the third harmonic, $\lambda_k/3$. Additionally, this wavelength exhibits substantial transient growth over the measurement domain, and its behavior is most consistent with optimal theory. For these reasons, the initial focus will be on the results from this wavelength.

To solve the problem numerically, the two branches of the continuous spectrum are discretized using 500 A and 500 B modes. κ is logarithmically spaced from $\kappa = 0.01$ to capture behavior near the branch point at $\kappa = 0$ up to a value of κ corresponding to the second branch point, $i\beta$. The pressure modes that begin at this branch point are neglected due to their rapid spatial decay. To generate the modes, an integration-based technique was used, with normalization conditions modeled after Ref. [42] ($\partial u/\partial y|_0 = 1$). The mode shapes were verified with a Chebyshev pseudospectral technique based on Ref. [46].

Although exhaustive resolution studies are not conducted, the resolution is verified by ensuring the computed velocity profiles sum to zero in the freestream at multiple x locations. Additionally, the velocity reconstructions show no "ringing" phenomena and exhibit complete freestream cancellation (see e.g., Fig. 7). Further, unlike discretization methods used in DNS and similar computations, the method of discretizing the continuous spectrum has no effect on the mode shapes. That is, the shape and evolution of each mode is independent of the neighboring modes, and adding additional solutions would serve to "sharpen" the solution. Given this, the *a posteriori* validation is deemed sufficient, and the lower bound on the necessary number of modes will be explored in the future as work on more computationally demanding problems is undertaken.

Using the DNS data available from Ref. [39], Eq. 2.33 can be used to directly compute the amplitude distribution C_α. Once this decomposition is performed at an initial streamwise station, the initial value problem is fully specified, and the downstream flow-field is completely determined. The evolution given by linear parallel theory is then compared with the DNS results. Figure 7 (a) compares the streamwise disturbance velocity for the $\lambda_k/3$ wavelength from the DNS and the eigenfunction reconstruction plotted against the Blasius coordinate ($\eta = y/\delta$). This result is for the decomposition performed 25 mm (35 δ_{avg}) downstream of the roughness elements. The decomposition/reconstruction reproduces the $\hat{u}$ velocity with high accuracy. Figure 7 (b) shows the results for the $\hat{w}$ and the $\hat{v}$ and the agreement is also very good. Note that $\hat{u}$ and $\hat{v}$ are even functions, and thus purely real, while $\hat{w}$ is odd so the imaginary component is shown. The error is significantly less than 1% of the maximum $\hat{u}$ disturbance, which is scaled to unity. This agreement demonstrates that the continuous modes can be combined to accurately describe an arbitrary disturbance at one streamwise location. While this alone does not validate the linear/parallel assumptions, it does validate the choices of how to discretize the branches. Validating the accuracy of the other assumptions requires evaluating the agreement as the disturbance evolves downstream. This agreement is shown below.

As described above, the $\lambda_k/3$ disturbance is composed of two continuous distributions of modes with purely imaginary α values ranging from $\alpha_i \approx \beta^2/Re = 8.5 \times 10^{-4}$ for $\kappa \to 0$ to $\alpha_i = \beta = 0.658$ as κ is increased. For each imaginary α, the A and B modes have complex amplitudes, C_α. The amplitudes and phases of these two branches are plotted in Fig. 8 for the x location corresponding to Fig. 7. This plot is the complete quantitative description of the flow's receptivity to the roughness.

The C_α distributions are centered about $\alpha_i = 0.006$. In physical terms, this roughly defines the overall decay rate of the disturbance. That is, because the largest amplitude modes decay with $\alpha_i = 0.006$, eventually, the disturbance will exhibit roughly this decay rate after the transient growth has subsided. The corresponding phase plot shows that the A and B modes are almost exactly out of phase. It should be pointed out the opposite sign of either phase could be shown, as the choice of the A and B modes is arbitrary. Had the complex conjugate A mode been selected, the spectrum would be of opposite sign. This phase behavior may be a consequence of enforcing the condition that the perturbation tend to zero in the freestream. Additionally, the distribution function is dependent on the choice of normalization when solving both Eq. 2.25 and Eq. 2.33. Therefore, relative differences between spectra are meaningful, but the numerical values depend on details of the method and how Q_α is defined. With this in mind, it is interesting that the amplitude distribution is a surprisingly simple function given the complexity of the roughness wake. The fact that the amplitude distribution is simple and could be described by just a few parameters suggests it may be possible to construct simplified empirical models of how roughness leads to non-optimal disturbances.

Previous experimental work[15] has shown that the boundary layer receptivity to roughness elements scales nonlinearly with increasing roughness amplitude. Further, qualitative results from both experiments and DNS visualizations indicate that finite disturbances exist in the very near wake of the roughness elements, possibly due to a separation bubble on the leeward side of the roughness element. Given these two facts, it is expected that the perturbations are not well described by linear theory in the immediate wake of the roughness element. Instead, the large perturbations must be allowed to decay before linear theory is applicable. The decomposition technique can be used to determine the extent of the nonlinear region.

Figure 9 shows the results for decompositions at several downstream locations. This figure shows that for approximately 20 mm ($3D$) downstream of the roughness, the decomposition cannot capture the energy evolution in the $\lambda_k/3$ wavelength. The predicted peak energy is higher at 10 mm than at either 6 mm or 15 mm. However, downstream of this location the agreement is quite good. The decomposition at 25 mm is accurate for over 150 δ_{avg}, until, presumably, non-parallel effects begin to cause disagreement. The energy evolution from the decomposition at 20 mm is also reasonably accurate. The disturbance energy is a sensitive metric, and the small overshoot between 25 mm and 20 mm can be partially attributed to the slightly different values of Reynolds number used at the decomposition locations.

This process is repeated for the other important wavelengths. Figure 10 shows that the other wavelengths also compare well to results found in Ref. [52]. Notably, the decomposition is able to not only capture the transiently growing disturbances found in the third and fourth harmonics, but also show the decay in the second harmonic. Also, the decomposition tracks the the transition from decay to growth and back to decay of the fundamental wavelength despite the relatively small energy content at the decomposition location, $x_0 = 35\delta_{\text{avg}}$. There is a small but noticeable underprediction in the energy content of the fundamental wavelength that will also be seen in the experimental decomposition. This is potentially due to non-parallel effects.

The behavior of each of the wavelengths can be explained by the amplitude distributions shown in Fig. 11. The peak of the amplitude distributions for the third and fourth harmonic fall at roughly the same wavenumber $\alpha_i = 0.006$, which translates into their energy maxima occurring at roughly the same downstream location, with different total energies. The fundamental wavelength has its maxima at a much lower wavenumber, which indicates maximum growth further downstream and slower decay. These features are seen in the energy evolution. In contrast the spectrum of the second harmonic is much broader and lacks the defined structure of the other spectra. These features may lead to the absence of transient growth in this case. In addition to the information found in the amplitude distributions, the phase distribution may be important, however its role is unknown without further cases to analyze.

Parametric Analysis

Work is ongoing at the Computational Fluid Physics Laboratory at the University of Texas to perform detailed DNS of other roughness geometries, including different roughness heights and diameters. Decomposing results from this DNS presents a challenge in that the DNS is a pressure-free formulation, and the decomposition process must be modified slightly. Fig. 21 shows that decomposing a perturbation without pressure information gives identical results to the full decomposition. This work has recently achieved some useful results for very low $Re_k \approx 50$, and over certain domains for larger amplitude roughness configurations (private communication). However, difficulties with the DNS finding a steady state (which will be explained in the secondary instability chapter) have made larger parametric comparisons difficult. There is not enough confidence in these results to make delicate comparisons across roughness geometries.

However, through this collaboration, an additional application for multimode decomposition has been found, namely, validating DNS results by showing the deviation from linear predictions. The multimode decomposition of DNS results with smaller roughness elements than those considered by RV showed significant discrepancy with the linear theory (despite smaller disturbances), thus encouraging grid refinement and more detailed study.

B. Theoretical Receptivity Comparisons

An optimal perturbation is defined as the initial condition that generates the most kinetic energy growth over a specified domain. Refs. [14, 35, 15] found experimentally that physically realized perturbations attained maximum energy well upstream of optimal predictions. This section attempts to quantify the difference between optimal and realizable perturbations by identifying their amplitude distributions. The present decomposition calculations provide a means of explaining not just *how* realizable disturbances are different, but *why* they are different from a receptivity perspective. Further, the important connection between optimality and the location of the disturbance in the boundary layer identified in Ref. [35] can be analyzed in a rigorous way. Contrasting the amplitude distribution of theoretically generated and physically realized disturbances is central to future progress in modeling of increasingly realistic disturbances. The optimal solutions corresponding to the present parameters were found using the singular value decomposition described in Chapter II. Comparisons are also made to the linear receptivity model[53].

The amplitude distribution of the continuous spectrum modes found in Fig. 8 are compared to the distribution of an optimal disturbance in Fig. 12. This figure shows that higher α_i modes are excited by roughness than are required for an optimal disturbance. This is to be expected as the realized disturbance decays much more quickly than the optimal disturbance. It is also noteworthy that the amplitude shape is similar between the two disturbances, indicating that a wide class of disturbances likely share this one-peaked structure. Figure 12 also shows that the shift in wavenumber space moves the spectrum toward the linearized boundary conditions found in Ref. [53], whose amplitude distribution is also similarly shaped. This suggests that the physically realized disturbance, though not well described by linear receptivity or optimal disturbance theory, lies in between these two extremes with a somewhat predictable amplitude distribution.

Prior to the development of the present approach[42], a method of characterizing sub-optimal disturbances was proposed by Fransson et al.[35] that involves rescaling an optimal disturbance, compressing it lower in the boundary layer and computing its growth using a spatial marching technique. Fransson et al. found that the energy evolution of this rescaled vortex was a closer approximation of the physically realized energy than optimal theory. This approach can be evaluated using multimode decomposition, by first solving for the optimal disturbance, rescaling the y coordinate by a factor c, performing the decomposition, and then projecting the result downstream. This calculation shows similar behavior to what is found in Ref. [35]. The energy maximum occurs further upstream in accordance with the experimental findings. Figure 13 shows that the effect of this process on C_α is to shift the spectrum up in wavenumber space toward larger α_i. This suggests a correlation between the distribution of amplitudes in the wavenumber space and the location of a disturbance in the boundary layer.

Continuing this process to match the experimental results described in the present work gives a value of the scaling parameter $c = 0.32$. Fig. 14 shows the continuous spectrum amplitudes, and Fig. 15 shows the energy evolution for this case. The continuous spectrum peak has shifted in line with the DNS solution, and the energy evolution now peaks in the same downstream location. These results somewhat validate the results found in Ref. [35]. However, Fig. 16 shows that the decomposition does not do as effective a job of decomposing this disturbance as compared to the physically realized disturbance shown in Fig. 7. The poor comparison means that the initial condition of a compressed optimal disturbance is not a solution of the OSS equations in the band of α examined here. However the location of the resulting streamwise streak is in agreement with the present results and will be used later.

As the disturbance shown in Fig. 16 evolves downstream, the higher harmonic oscillations in y decay quickly and the resulting perturbation is consistent with what is seen in the DNS and decomposition resulting in similar energy growth. However, it is clear that agreement of the energy evolution requires the velocity profiles to not agree with the input scaled-optimal disturbance, so that approach is not self-consistent.

Moreover, although the $\lambda_k/3$ and $\lambda_k/4$ energies may be captured by compressed optimal disturbances, for the other cases shown in the present work, $\lambda_k/2$, where there is minimal growth, and λ_k, which experiences both decay and growth, rescaling an optimal disturbance does not reproduce even the energy evolution. Therefore, as more complicated roughness geometries are analyzed it is unlikely that rescaling an optimal disturbance will be able to account for these more intricate spanwise variations.

C. Experimental Decomposition

The decomposition into continuous spectrum modes can be found from Eq. 2.33 when all velocity and pressure components of $\hat{\phi}(x_0)$ are known. This level of detail and accuracy is possible in DNS. However, in an experiment this complete and accurate information is not available[15]. While DNS can be performed for certain simple geometries, it remains resource intensive and, at this point, a DNS of realistic distributed roughness (e.g., Ref. [41]) is not feasible. Thus, for distributed roughness in a variety of realistic situations, experiments will remain the primary source of new data.

Since the linearity of the transient growth in this experimental configuration was demonstrated in the previous section, the experimental results from Ergin and White (EW)[36] are a good candidate to attempt a partial data decomposition. Again, the goal is to extract information similar to what was found in the decomposition of the DNS, using only the streamwise velocity at multiple streamwise locations. A successful decomposition will not only provide the receptivity information, but also reveal the correct underlying vortex dynamics that drive the transient growth but have proven too challenging to measure directly.

Disturbance profiles from 13 x locations are used to reconstruct the energy evolution. The optimal regularization coefficients can be found in Table II. The least squares term in Eq. 2.49 is weighted by the estimated measurement uncertainty for a given x location, allowing the solver more flexibility at locations with less certainty. Recall that γ_1 is the penalty for large amplitudes and γ_2 is the smoothness penalty. Whereas Eq. 2.49 includes an amplitude regularizing term, in all cases except $\lambda_k/2$ the best result gave $\gamma_1 = 0$. This is not universal; depending on how the modes are discretized and other measurement factors, γ_1 can be important. It is worth noting that, for the cases with growth, the larger difference between the measured perturbation and the optimal perturbation requires a larger γ_2.

TABLE II

Regularization Parameters

Wavelength	λ_k	$\lambda_k/2$	$\lambda_k/3$	$\lambda_k/4$
γ_1	0	1.33	0	0.0
γ_2	3750	0	7.50	562.5

Figure 17 shows the agreement between the input disturbance energy and the calculated energy found with the partial data composition. This figure shows that for a case of initially strong energy growth ($\lambda_k/3$, $\lambda_k/4$), a case of initial decay followed by slower growth (λ_k), and a case of almost no growth ($\lambda_k/2$), the partial data technique is able to capture the appropriate energy evolution. This energy evolution falls within the error estimates for much of the domain for cases with strong initial growth, and decays slightly faster than the experiment, likely owing to non-parallel effects as the disturbance travels downstream. For the fundamental wavelength, the decomposition is not as accurate. This is partly due to the very low energy in the upstream x locations for the fundamental harmonic. These initial x locations have a strong influence on the overall result. Further it should be noted that the DNS decomposition also underpredicts the energy evolution.

Figure 18 shows the reconstructed velocity profiles. Recall that the lines in this figure were generated without any measured $\hat{v}$ and $\hat{w}$. The maximum $\hat{u}$ perturbation is scaled to unity for comparisons between the DNS and experiment (whose total energy is not in exact agreement). These figures show excellent agreement in the profile shapes in the streamwise, wall-normal and spanwise directions. All profiles peak at roughly the same velocity and η values. There is some disagreement in the upper-lobe of the $\hat{w}$ profile and the magnitude of $\hat{v}$ but the energy evolution in the experiment and in the DNS are not identical. In fact, at this location, 25 mm downstream, the experiment has undergone somewhat more dramatic transient growth, so it is not unexpected that the profiles show some differences. Regardless of this, these profiles show it is possible to extract the underlying streamwise vortex structure. This was impossible using slantwires. From this reconstruction it is clear why measuring these profiles was so experimentally challenging. The velocity profiles in Fig. 18 are scaled by the maximum of the $\hat{u}$ disturbance. The $\hat{u}$ perturbation is less than 5% of the mean flow velocity, and the spanwise and wall-normal components are on the order of 5% of the $\hat{u}$ value.

While on its face, the quality of the decomposition in Fig. 16 is on par with Fig. 18, note that Fig. 16 compares a decomposition performed with complete flow data to that same data whereas Fig. 18 compares a DNS solution to a decomposition computed using only experimental $\hat{u}$ data. Thus, for the approach of rescaling optimal disturbances to be judged an effective means of representing sub-optimal disturbances, the comparison shown in Fig. 16 should be as good as that shown in Fig. 7 (i.e., the comparison of the sub-optimal DNS solution to its decomposition). The relatively worse agreement in Fig. 18 can be attributed to the facts that it compares $\hat{v}$ and $\hat{w}$

profiles generated using only experimental $\hat{u}$ data and simply that it is a comparison between two different data sets, an experiment and DNS.

Figure 19 shows contours of streamwise and wall-normal velocity transformed back to physical space. The upper figures are wall-normal velocity and the lower figures are spanwise velocity. The far left is the reconstruction based on the experimental decomposition using the four dominant modes slightly further downstream (50 mm, $68\delta_{\mathrm{avg}}$). The center figure is the DNS result using only those modes, and the far right figure is the complete DNS. These figures show that the experimental decomposition captures the essence of the underlying vortex structure in the roughness wake, making it possible to visualize the complete flow field behind an arbitrary perturbation. This makes it possible for experiments to proceed with more complicated, distributed roughness elements that are currently beyond the scope of DNS.

Figure 20 shows the continuous spectrum distribution for the $\lambda_k/3$ solution. The overall magnitude is larger in the experimental decomposition for the same total energy. This indicates that there is more mode cancellation present in this solution, which is consistent with the faster growth rate seen in the experiments as compared to the DNS[54]. However, the location of the peak amplitude and the slope of the phase distribution are in good agreement. While qualitatively similar in some respects to the DNS solutions, there is one notable difference. The A branch distribution has two peaks and not just a single peak. This could complicate modeling attempts as more parameters may be necessary to describe this distribution than the more straightforward DNS result.

An important note regarding Fig. 20 is the complication imposed by non-parallel flow. While the DNS decomposition can be calculated purely locally, the multiple stations used in the experimental decomposition necessarily re-introduce these effects. Future efforts will focus on larger, more developed boundary layers (i.e. less non-parallel) to explain why the experimental amplitudes are not single-peaked as they appear in the DNS data. Numerically speaking, increasing the least squares regularization (γ_1) smooths out this structure, but decreases the accuracy of the result. Given this, the additional peak is likely not a numerical artifact but rather the solution compensating for non-parallel effects.

D. Summary

Several features of roughness-induced transient growth have been isolated in this chapter. First and foremost, physically realizable transient growth is a linear process. While the receptivity is non-linear, the subsequent evolution of the perturbation is governed by the linear initial value problem. This means that the discrepancy between optimal perturbation predictions and what is measured experimentally is due to a difference in the receptivity function, not due to non-linear evolution. Further, the extent of the non-linear receptivity region can be mapped by determing where the linear initial value problem solution is valid.

Second, multimode decomposition can sort and track the behavior of different spanwise modes, and reduce large data into simplified amplitude functions. Future modeling will rely on reduced models of the dynamics of the boundary layer. While methods such as proper orthogonal decomposition can give a reduction of the dynamics for systems with large training data sets, they do not reflect to true underlying dynamics. Continuous spectrum analysis does capture the correct dynamics, and understanding its behavior is key to future modeling and control.

Third, realizable amplitude functions are qualitatively and quantitatively different than optimal theory and linear receptivity, but share some key features that may make modeling possible. The shapes of the receptivity functions do not appear overly complex and are somewhat consistent with shifts in the complex α plane. It is possible that some universal behavior can be isolated from these functions.

Fourth, the decomposition problem can be solved using DNS without all the flow data being available. This makes the process feasible for DNS codes that solve without pressure information. More importantly, the decomposition problem for experimental data with only streamwise velocity is solved using multiple streamwise measurement locations and regularization methods for ill-posed problems. This decomposition of experimental data reveals previously unmeasurable velocity components and the vortex behavior that drives transient growth in addition to the receptivity information.

CHAPTER IV

SECONDARY INSTABILITY THEORY

Experimental investigations[55, 56] have shown that even in cases where the primary instability is two-dimensional, i.e. a T–S wave, the onset of turbulence is preceded by the rapid growth of a three-dimensional instability. This *secondary* instability structure, characterized in flow visualizations as either aligned or staggered Λ-vortices, exists on top of the mean flow distortion created by the growing T–S wave. In the case of a traveling T–S wave, relatively small amplitudes can create secondary instabilities ($u'_{rms} \sim \mathcal{O}(1\%)$). Floquet analysis, taking advantage of the streamwise periodicity of the T–S wave, has proved a useful approach in isolating the secondary instability mechanisms[23].

The second generation of experiments described in the first chapter[24, 25], give experimental evidence that suggests the role of a "secondary" instability, due to inflectional velocity profiles, in cases of roughness-induced transition. Further, the observation by Morkovin[21] that roughness enhances the onset of the three-dimensional instability mechanism highlights the importance of these type of disturbances. However, some care must be taken in defining the concept of "secondary" instability in the present work. Secondary instability appears in the previous sentences in quotes because, as has been shown, the disturbance growth behind cylindrical roughness elements analyzed in the current work is a result of the transient-growth mechanism, and not any primary instability.

This work will not address how transient growth affects the primary T–S instability (Path B in Fig. 1). Further, the interaction between the secondary instability of T–S waves and the "secondary" instabilities that arise from transient growth (potential Path B–C connection) suggested by Morkovin will only be addressed tangentially.

While this problem is of great interest, a complete, viscous, interaction-theory type computation[57] is beyond the scope of this dissertation.

The focus here is on secondary instabilities generated by the basic state modulation due to transient growth, Path C in Fig. 1. The method of analysis will be similar to previous secondary instability calculations. Instead of the basic state being the Blasius boundary layer and a traveling, streamwise-periodic T–S wave, the basic state is the Blasius boundary layer and a steady, spanwise-periodic, transiently-growing perturbation. In both cases, the amplitude of the primary disturbance is varied to correlate the necessary disturbance amplitude with the onset of a secondary instability, and the physics of the instability that arises can be studied.

A secondary stability analysis of optimal transient growth was carried out in detail using inviscid Floquet theory by Andersson et al.[33]. This study found two unstable secondary instabilities associated with the optimal perturbation. One instability is anti-symmetric in the spanwise direction, referred to as a sinuous perturbation, that is sustained by velocity gradients in the spanwise direction. The second is symmetric in the spanwise direction, referred to as varicose, and is sustained by gradients in the wall-normal direction. This varicose profile is non-physical and unlikely to contribute to breakdown due to non-vanishing streamwise velocity at the wall. This solution is permissible in the inviscid approximation, but would be strongly attenuated with the inclusion of viscosity.

Comparison with experiments and DNS led the authors in Ref. [33] to conclude that sinuous perturbations, unstable due to spanwise inflectional velocity profiles, are the likely cause of breakdown in the presence of high-amplitude streaks. However, later experimental work[36] observed breakdown at amplitudes deemed subcritical to these secondary instabilities. To analyze whether this type of inflectional secondary instability is at work in these experiments, the present work performs secondary instability calculations using the sub-optimal transient growth found in experiments and DNS consistent with Ref. [36].

Prior chapters have dealt in great detail with how physically realized transient growth is not consistent with optimal perturbations. Thus, any secondary instability calculations involving the more realistic basic state from previous chapters will provide results that are somewhat different than previous work. However, a broader physical argument is important. Much of the justification for optimal growth approaches has been that they represent the "most dangerous" perturbations. Thus if analytical efforts focus on optimal perturbations, the results represent a conservative upper-bound for predicting transition behavior. This argument is at odds with experimental findings that observe more rapid breakdown than predicted in the presence of sub-optimal perturbations.

While optimal perturbations are "optimal" in the sense that they produce the most energy growth, they are, in fact, sub-optimal in terms of generating secondary instabilities. Physically, the optimization process reduces the velocity gradients that comprise the growing laminar "streak". While this leads to a larger streak amplitude and slower disturbance decay downstream, it also limits the profile's susceptibility to secondary instabilities which feed on these gradients. Chapter V shows, both via a simplified model streaky boundary layer, and using the complete boundary layer profile behind the roughness elements, that physically realized transient growth has higher growth rates and a neutral curve at lower amplitudes than optimal predictions. Further, this approach will explain the "critical" nature of transition behind these roughness elements seen in experiments and DNS dating back several decades[18], as well as why some DNS approaches have difficulty achieving convergence to a steady-state.

A. Theoretical Development

The approach to secondary instability analysis is the same as was used to study optimal streaks in Ref. [33], a temporal stability calculation with a Floquet expansion in the spanwise direction. With the inviscid assumption the governing equations are the Euler equations. They are linearized about a meanflow profile that now depends on both y and z as it has been modulated by the transient growth, $U(y,z) = U_B(y) + u_{TG}(y,z)$. These equations are:

$$\begin{aligned} \frac{\partial u'}{\partial x} + \frac{\partial v'}{\partial y} + \frac{\partial w'}{\partial z} &= 0 \\ \frac{\partial u'}{\partial t} + U\frac{\partial u'}{\partial x} + \frac{\partial U}{\partial y}v' + \frac{\partial U}{\partial z}w' &= -\frac{\partial p'}{\partial x} \\ \frac{\partial v'}{\partial t} + U\frac{\partial v'}{\partial x} &= -\frac{\partial p'}{\partial y} \\ \frac{\partial w'}{\partial t} + U\frac{\partial w'}{\partial x} &= -\frac{\partial p'}{\partial z} \end{aligned} \tag{4.1}$$

scaled by $\delta = \sqrt{\nu x/U_\infty}$, with the limit taken as $Re \rightarrow \infty$. As shown in previous chapters, the spanwise and wall-normal velocity of the basic state, V and W, are very small compared to U.

Unfortunately, unlike in the usual inviscid scenario where Eq. 4.2 can be manipulated to get a solution for v only, the fact that $U \rightarrow U(y,z)$ prevents this. However, the pressure can be decoupled to arrive at an equation that is free of other variables:

$$\left(\frac{\partial}{\partial t} + U\frac{\partial}{\partial x}\right)\nabla^2 p' - 2\frac{\partial U}{\partial y}\frac{\partial^2 p'}{\partial x \partial y} - 2\frac{\partial U}{\partial z}\frac{\partial^2 p'}{\partial x \partial z} = 0 \tag{4.2}$$

Since the mean flow variables do not depend on x or t a normal modes substitution is possible:

$$p'(x,y,z,t) = \tilde{p}(y,z)e^{i\alpha(x-ct)} \quad + \text{c.c.} \tag{4.3}$$

A normal modes substitution gives a two dimensional equation parameterized by the real streamwise wavenumber α and the complex phase speed c.

$$(U - c)\left(\frac{\partial^2}{\partial y^2} + \frac{\partial^2}{\partial z^2} - \alpha^2\right)\tilde{p} = 2\frac{\partial U}{\partial y}\frac{\partial \tilde{p}}{\partial y} + 2\frac{\partial U}{\partial z}\frac{\partial \tilde{p}}{\partial z} \tag{4.4}$$

This equation is very similar to the Rayleigh equation, reflecting the inviscid nature of the disturbance. The boundary conditions on $\tilde{p}$ for Eq. 4.4 are $\partial\tilde{p}/\partial y = 0$ at $y = 0, \infty$.

There are a few methods available to solve eigenvalue problems of the form in Eq. 4.4. Some authors, in an effort to generate more general-purpose codes, solve a collocation problem in both the y and z direction (see e.g. [58]) or compact finite differences (see e.g. [59]). Alternatively, the periodicity of the basic state can be exploited to address the problem using Floquet analysis. This approach handles the physical coupling in the z direction first, before solving the eigenvalue problem using collocation in the wall-normal direction only. This approach has the advantage of solving an eigenvalue problem with banded matrices (in contrast to the collocation methods) as well as having an explicit way of monitoring whether the spanwise resolution is sufficient (in contrast to the finite difference approaches).

Floquet analysis is the extension of the normal modes approach to situations where the coefficients of the problem vary periodically. Ordinarily, the normal modes assumption relies on the basic state being independent of the the normal mode variable. This variable then must appear in the solution as an exponential term and the solutions can be decoupled from each other. For example, the substitution from Eq. 4.3 is justified and general based on the fact that the base flow has no time or streamwise dependence. However substituting a normal mode for y would not be feasible.

Since the baseflow is two-dimensional, a simple normal mode substitution for z is also not possible. However, recognizing the periodicity in z at a wavelength specified by the spacing of the roughness array, the baseflow can be represented:

$$U(y, z) = \sum_{k=-\infty}^{\infty} U_k(y) e^{ik\beta z} \tag{4.5}$$

Given the setup of the problem as periodic cylinders, this form will describe the basic state velocity well even when only relatively few terms are considered. The series will be truncated at $k = m$, then $U_k(y) = 0$ when $|k| > m$. This reduces the size of the problem significantly.

Since the baseflow varies periodically in z, the solution retains the exponential dependence on z. This allows expanding $\tilde{p}$ as:

$$\tilde{p}(y, z) = \sum_{k=-\infty}^{\infty} \hat{p}_k(y) e^{i(k+\gamma)\beta z} \tag{4.6}$$

Here γ is the Floquet parameter and determines the extent to which the disturbance is fundamental ($\gamma = 0$), subharmonic ($\gamma = 0.5$), or detuned ($\gamma \in (0, 0.5)$). The fundamental mode varies over the same wavelength as the fundamental β in the basic state expansion. The subharmonic modes vary over double this wavelength, repeating the fluctuating mode shape once every two sets of streaks. Detuned modes represent other possible combinations, and preserves the generality of the expansion.

Taking derivatives the new form of the z dependent solutions gives:

$$\frac{\partial \tilde{p}}{\partial z} = \sum_{k=-\infty}^{\infty} i(k+\gamma)\beta \, \hat{p}_k(y) e^{i(k+\gamma)\beta z} \tag{4.7}$$

$$\frac{\partial^2 \tilde{p}}{\partial z^2} = \sum_{k=-\infty}^{\infty} -(k+\gamma)^2 \beta^2 \, \hat{p}_k(y) e^{i(k+\gamma)\beta z} \tag{4.8}$$

$$\frac{\partial U}{\partial z} = \sum_{k=-\infty}^{\infty} ik\beta \, U_k(y) e^{ik\beta z} \tag{4.9}$$

Substituting these into Eq. 4.4 gives:

$$\left(\sum_{k=-\infty}^{\infty} U_k(y)e^{ik\beta z} - c\right)\sum_{k=-\infty}^{\infty}\left[D^2\hat{p}_k - \left((k+\gamma)^2\beta^2+\alpha^2\right)\hat{p}_k\right]e^{i(k+\gamma)\beta z} = \tag{4.10}$$
$$2\sum_{k=-\infty}^{\infty} DU_k(y)e^{ik\beta z}\sum_{k=-\infty}^{\infty} D\hat{p}_k(y)e^{i(k+\gamma)\beta z} + 2\sum_{k=-\infty}^{\infty} ik\beta U_k(y)e^{ik\beta z}\sum_{k=-\infty}^{\infty} i(k+\gamma)\beta\hat{p}_k(y)e^{i(k+\gamma)\beta z}$$

where $D = \partial/\partial y$. The periodicity of the problem ensures these sums converge. Thus, the series multiplication can be carried out term-by-term. In all instances the outer sum stays as k and let the inner sum go to j, which gives:

$$\sum_{k=-\infty}^{\infty}\sum_{j=-\infty}^{\infty} U_k(y)\left[D^2\hat{p}_j - (j+\gamma)^2\beta^2\hat{p}_j - \alpha^2\hat{p}_j\right]e^{i(k+j+\gamma)\beta z}$$
$$-\ 2\sum_{k=-\infty}^{\infty}\sum_{j=-\infty}^{\infty} DU_k(y)D\hat{p}_j(y)e^{i(k+j+\gamma)\beta z} + 2\sum_{k=-\infty}^{\infty}\sum_{j=-\infty}^{\infty} k\beta^2(j+\gamma)U_k(y)\hat{p}_j e^{i(k+j+\gamma)\beta z}$$
$$= c\sum_{k=-\infty}^{\infty}\left[D^2\hat{p}_k - (k+\gamma)^2\beta^2\hat{p}_k - \alpha^2\hat{p}_k\right]e^{i(k+\gamma)\beta z} \tag{4.11}$$

Because the problem is still linear, and the z dependence has been removed, this equation must hold for all values of the integer k in the outermost sum. Since each of the terms on the left hand side goes as $e^{i(k+j+\gamma)\beta z}$, and the right hand side goes as $e^{i(k+\gamma)\beta z}$, equating the two sides for common wavenumbers requires that the equality holds for k on the right-hand side when on the left-hand side: $k \rightarrow k - j$. This shows why the simple normal mode expansion in Eq. 4.3 is not possible in the z direction, because the solutions here are not uncoupled. That is, the different pressure perturbation modes interact with the basic state modes. Thus the complete sums must be considered, not just the individual wavenumbers.

Removing the outer k sum, this substitution then gives:

$$\sum_{j=-\infty}^{\infty}\left\{U_{k-j}\left[D^2\hat{p}_j - (j+\gamma)^2\beta^2\hat{p}_j - \alpha^2\hat{p}_j\right] - 2DU_{k-j}D\hat{p}_j(y) + 2\beta^2(k-j)(j+\gamma)U_{k-j}\hat{p}_j\right\}e^{i(k+\gamma)\beta z}$$
$$= c\left[D^2\hat{p}_k - (k+\gamma)^2\beta^2\hat{p}_k - \alpha^2\hat{p}_k\right]e^{i(k+\gamma)\beta z} \tag{4.12}$$

Eliminating the exponential dependence and gathering terms gives the desired eigenvalue equation:

$$\sum_{j=-\infty}^{\infty} \left\{ U_{k-j} \left[D^2 - (j+\gamma)^2\beta^2 - \alpha^2 \right] - 2DU_{k-j}D + 2\beta^2(k-j)(j+\gamma)U_{k-j} \right\} \hat{p}_j$$
$$= c\left[D^2 - (k+\gamma)^2\beta^2 - \alpha^2 \right] \hat{p}_k \tag{4.13}$$

with the boundary condition remaining that the derivative of $\hat{p}$ must vanish at the wall and at ∞. This gives an infinite system of coupled differential equations, but it is now an eigenvalue problem for the phase speed c, non-homogeneous in y, for given α, β, k and γ (the detuning parameter).

This is a familiar form: y dependence only and real parameters. The sum for j must be truncated to allow for a numerical solution. In Ref. [33] $j \sim 15$ is used. With the increased complexity of the present work, many more spanwise modes are necessary. A safe truncation for j, typically $j \sim 45$, will be numerically verified by showing there is little energy content in the high wavenumbers. Limiting the wavenumbers for $U(y,z)$ to $|k| \leq m$, reduces the problem to a block diagonal form. That is, because $U_{k-j} = 0$ for $|k-j| > m$, the modes will only interact with certain "neighbors". Defining the operator on the left hand side of Eq. 4.13 to be $\mathcal{L}_{k-j,j}$, and the right hand side to be $\mathcal{R}_k$ the equations can be rewritten more compactly:

$$\sum_{j=-\infty}^{\infty} \mathcal{L}_{k-j,j}\hat{p}_j = c\mathcal{R}_k\hat{p}_k \tag{4.14}$$

If only one harmonic is included in the basic state, $m = 1$, then $\mathcal{L}_{k-j,j} = 0$ for $k > 1$, and a block-tri-diagonal structure is obtained:

$$\begin{bmatrix} \mathcal{L}_{0,-3} & \mathcal{L}_{1,-2} & 0 & 0 & 0 & 0 & 0 \\ \mathcal{L}_{-1,-3} & \mathcal{L}_{0,-2} & \mathcal{L}_{1,-1} & 0 & 0 & 0 & 0 \\ 0 & \mathcal{L}_{-1,-2} & \mathcal{L}_{0,-1} & \mathcal{L}_{1,0} & 0 & 0 & 0 \\ 0 & 0 & \mathcal{L}_{-1,-1} & \mathcal{L}_{0,0} & \mathcal{L}_{1,1} & 0 & 0 \\ 0 & 0 & 0 & \mathcal{L}_{-1,0} & \mathcal{L}_{0,1} & \mathcal{L}_{1,2} & 0 \\ 0 & 0 & 0 & 0 & \mathcal{L}_{-1,1} & \mathcal{L}_{0,2} & \mathcal{L}_{1,3} \\ 0 & 0 & 0 & 0 & 0 & \mathcal{L}_{-1,2} & \mathcal{L}_{0,3} \end{bmatrix} \begin{bmatrix} \hat{p}_{-3} \\ \hat{p}_{-2} \\ \hat{p}_{-1} \\ \hat{p}_{0} \\ \hat{p}_{1} \\ \hat{p}_{2} \\ \hat{p}_{3} \end{bmatrix} = c \begin{bmatrix} \mathcal{R}_{-3}\hat{p}_{-3} \\ \mathcal{R}_{-2}\hat{p}_{-2} \\ \mathcal{R}_{-1}\hat{p}_{-1} \\ \mathcal{R}_{0}\hat{p}_{0} \\ \mathcal{R}_{1}\hat{p}_{1} \\ \mathcal{R}_{2}\hat{p}_{2} \\ \mathcal{R}_{3}\hat{p}_{3} \end{bmatrix}$$

It can be seen that this also reduces further to the decoupled case (Rayleigh Equation) if $\mathcal{L}_{-1,j} = \mathcal{L}_{1,j} = 0$.

The structure of the basic state permits only even and odd solutions for the non-detuned modes. Thus, the numerical problem can be recast to exploit the symmetric or anti-symmetric nature of the solutions. For the majority of the computations in Chapter V, the anti-symmetric, fundamental sinuous mode, is of the greatest interest. In this case, $\hat{p}_{-j} = -\hat{p}_j$ and $\hat{p}_0 = 0$. These two equalities reduce the necessary modes in half, increasing the resolution greatly.

Discretizing the eigenvalue problem can be approached in the same way as the Orr–Sommerfeld equation in earlier sections, using Chebyshev collocation in y. The problem is sized by the number of y locations, and the number of spanwise modes. While the collocation method is similar to previous approaches, such a large scale eigenvalue problem will require a modified solution methodology as compared to the standard QZ algorithm for the Orr–Sommerfeld problem.

B. Large-scale Eigenvalue Computations

Typical eigenvalue problems in boundary layer stability encountered in engineering applications (i.e., amenable to solution with existing software such as LASTRAC[60]) tend to be of modest size. A typical computation will have $\mathcal{O}(10^2)$ points in the wall-normal direction, resulting in a matrix with $\mathcal{O}(10^4)$ elements. A QZ factorization approach to matrices of this size yields the eigenvalues with sufficient accuracy in reasonable time. However, the problems of interest in the proposed dissertation can be up to four orders of magnitude larger, $\mathcal{O}(10^8)$ matrix elements. This makes factorization limiting in both time and accuracy. Also, only a few of the least stable eigenvalues are of interest, thus the expense of the complete factorization of the matrix is not justified. To find the eigenvalues of Eq. 4.13, iterative methods are employed instead.

A popular class of iterative methods for large-scale eigenvalue problems in fluid dynamics are based on Arnoldi iteration. These methods use a sophisticated form of power iteration to construct subspaces on which iterated solutions converge to the correct eigenvectors. One implementation of the procedure, which also incorporates implicit restarts to the iterations (IRAM), is available for research use as ARPACK[61] and has been shown in a variety of cases to be an efficient eigenvalue algorithm[62] (See Appendix B for a brief explanation). While some drivers are available for simple, or symmetric eigenvalue problems, some work is required to implement the IRAM algorithms in ARPACK for generalized, complex, non-symmetric eigenvalue problems. Several numerical techniques are used to quickly compute eigenvalues and eigenvectors of large-scale problems.

Consider the eigenvalue problem:

$$\mathbf{A}x = \lambda \mathbf{M}x \tag{4.15}$$

with both **A** and **M** general, complex $n \times n$ matrices. While some factorization methods are possible for generalized matrices without inverting, Eq. 4.15 can be reposed as a standard eigenvalue problem.

$$\mathbf{M}^{-1}\mathbf{A}x = \lambda x \tag{4.16}$$

If this inverse were found directly it would be both computationally expensive and potentially error-prone given the size of the matrices involved, but its computation is not necessary for iterative schemes. For any iterative method applied to Eq. 4.16, what is required is an efficient way of computing the matrix-vector product:

$$v_{i+1} = \mathbf{M}^{-1}\mathbf{A}v_i \tag{4.17}$$

For the present problem the focus is the most efficient way of supplying Eq. 4.17 to the underlying Arnoldi algorithm.

The IRAM converges to a specified number of eigenvalues of largest magnitude lying near the convex hull of the c spectra. Fig. 22 shows an example of what a convex hull might look like for the case of a Rayleigh-type equation. In a sense, the hull corresponds to the eigenvalues furthest in magnitude from the center of the spectra. Convergence toward the eigenvalues near the hull, that is, away from the real line, is more rapid. This property that can be exploited if an initial guess for the eigenvalue of interest is known.

Let the estimated eigenvalue be σ. Eq. 4.15 can be rewritten:

$$\mathbf{A}x - \sigma\mathbf{M}x = \lambda\mathbf{M}x - \sigma\mathbf{M}x \tag{4.18}$$

Factoring with respect to x gives:

$$\left(\mathbf{A} - \sigma\mathbf{M}\right)x = \left(\lambda - \sigma\right)\mathbf{M}x \tag{4.19}$$

which can be recast as a standard eigenvalue problem:

$$(\mathbf{A} - \sigma\mathbf{M})^{-1}\mathbf{M}x = \frac{1}{(\lambda - \sigma)}x = \theta x \tag{4.20}$$

If the true eigenvalue is near the estimated eigenvalue $\theta = (\lambda - \sigma)^{-1} \rightarrow \infty$ and this eigenvalue is mapped very far from all others. This is shown in Fig. 23. This shift-invert strategy in Eq. 4.20 leads to very rapid convergence for the iterative method, provided there is an efficient way of supplying the matrix-vector product:

$$v_{i+1} = (\mathbf{A} - \sigma\mathbf{M})^{-1}\mathbf{M}v_i \tag{4.21}$$

Another method for improving the convergence of the IRAM is a slightly more complicated transform advocated by Schmid and coworkers[63, 59], that seeks to exploit the shift-invert convergence behavior of Eq. 4.20, but improve the matrix-vector product computation. Noting that Eq. 4.20 maps the eigenvalue of interest toward ∞, but all other eigenvalues toward zero, it is expected that the condition number for the matrix inversion, approximated as the largest eigenvalue over the smallest, will get very large. To remedy this instead of mapping the eigenvalues to zero, a generalized Cayley transform is employed that maps unwanted eigenvalues to one, and provides the additional flexibility of rotating this mapping in the complex plane.

Starting again with Eq. 4.15 and multiplying both sides by the same factor:

$$(\xi - 1)\,\mathbf{A}x = (\xi - 1)\lambda\mathbf{M}x \tag{4.22}$$

this can be rearranged:

$$\xi\mathbf{A}x = \mathbf{A}x + (\xi - 1)\lambda\mathbf{M}x \tag{4.23}$$

letting what will once again be the initial eigenvalue guess be σ, a term can be subtracted from both sides:

$$\xi \mathbf{A}x - \sigma\xi\mathbf{M}x = \mathbf{A}x + (\xi - 1)\lambda\mathbf{M}x - \sigma\xi\mathbf{M}x \tag{4.24}$$

factoring and inverting the left-hand side leaves:

$$\xi x = (\mathbf{A} - \sigma\mathbf{M})^{-1}(\mathbf{A} - (\xi\sigma - (\xi - 1)\lambda)\mathbf{M})\, x \tag{4.25}$$

Letting $\mu = \xi\sigma - (\xi - 1)\lambda$, gives the final form for the generalized Cayley transform:

$$\xi x = (\mathbf{A} - \sigma\mathbf{M})^{-1}(\mathbf{A} - \mu\mathbf{M})\, x \tag{4.26}$$

Now, specifying σ near the true eigenvalue once again maps the true solution toward infinity as:

$$\xi = \frac{\mu - \lambda}{\sigma - \lambda} \quad . \tag{4.27}$$

Solutions far from σ are mapped toward one, and μ provides another parameter that allows rotations in the complex plane to move desired eigenvalues to different places that are more accessible to the iterative procedure. The eigenvalue can be recovered:

$$\lambda = \frac{\xi - \mu}{\xi - 1} \tag{4.28}$$

and the eigenvectors are the same as for the un-altered case.

Whether Equations 4.16, 4.20 or 4.26 are employed an efficient method of providing a matrix-vector product involving an inverse is necessary. Taking Eq. 4.20 as an example, the IRAM (or any iterative method) requires repeated matrix-vector products of the form:

$$v_{i+1} = (\mathbf{A} - \sigma\mathbf{M})^{-1}\mathbf{M}v_i \tag{4.29}$$

For reasons of computational cost and accuracy, finding the inverse of the matrix in Eq. 4.29 is undesirable. Fortunately, because an iterative method is being employed as opposed to a factorization method, this matrix need never be calculated. Instead, the following procedure is used to compute the matrix-vector product necessary for iterations. First the straightforward matrix-vector product is computed:

$$w = \mathbf{M} v_i \tag{4.30}$$

Undoing the inverse procedure would give a system of linear equations in the following form:

$$\left(\mathbf{A} - \sigma \mathbf{M}\right) v_{i+1} = w \tag{4.31}$$

Noting that the matrix on the left hand side is constant for each iteration (it only changes when the parameters in Eq. 4.13 change), it is possible to prefactor the left hand side once, and use this factorization for all iterations. Computing the LU Decomposition:

$$\left(\mathbf{A} - \sigma \mathbf{M}\right) = \mathbf{L}\mathbf{U} \tag{4.32}$$

the "inverse" can be computed at every iteration with only simple back and forward substitutions, and what is is left is a three step procedure for evaluating every iteration that requires no factorization at all.

$$\text{Multiply :} \qquad w = \mathbf{M} v_i \tag{4.33}$$

$$\text{Solve :} \qquad \mathbf{L} y = w \tag{4.34}$$

$$\text{Solve :} \qquad \mathbf{U} v_{i+1} = y \tag{4.35}$$

In practice, if a reasonable guess for σ is chosen, the one-time LU factorization is more time consuming than all subsequent iterations.

The Cayley transform is of less importance for the problem of present interest than in the works cited[63, 59]. First, because of the inviscid assumption, the resulting eigenvalue problem is significantly less stiff than the viscous problem. Second, since the solution approach involves a relatively straightforward LU factorization, and the back and forward substitutions, it is less sensitive to ill-conditioned systems than solving Eq. 4.31 using an advanced iterative method (i.e. GMRES, or Bi-Conjugate Gradient Methods) as was necessary in Ref. [59]. This makes the shift-invert approach the method of choice for most computations.

An example of the improvement in computational time is shown in Fig. 24. Here a standard QZ factorization method (used for optimal perturbation calculations) is contrasted with the iterative method for different combinations of wall-normal grid points and spanwise modes included in the Floquet expansion. The total size of the eigenvalue problem is the product of these two numbers. On a standard desktop computer with no parallelization, Fig. 24 shows that the computational time for QZ algorithm goes as $N^{3.2}$, whereas the iterative method goes as $N^{2.2}$. There is a spread in the iterative method as the initial condition is randomized every time, whereas the QZ algorithm is deterministic from run-to-run. For the large scale eigenvalue problems considered in the next section, the iterative method provides a substantial time savings.

The procedure for computing and tracking eigenvalues is to solve Eq. 4.13 for a basic state with a high-amplitude transient perturbation. This high amplitude ensures that the eigenvalue spectrum is sufficiently spread off the real line to allow the IRAM to converge to the several largest imaginary values. Once these largest values are found, each one is tracked using a transform method as the transient-growth amplitude is decreased.

Figure 25 shows why the shift-invert procedure is necessary. For high-amplitude transient growth, the standard IRAM procedure converges rapidly. In fact in converges more rapidly than the shift invert procedure as the shift invert transformation requires computations be done with complex numbers instead of real numbers. However, as the amplitude is decreased, the computational cost of the shift-invert method stays constant while the standard method begins to grow unpredictably, and does not converge for $u_{TG,rms} < 0.08$.

C. Neutral Curve Computations

An additional problem presents itself when dealing with the inviscid stability equations as opposed to the full Orr–Sommerfeld/Squire equations. Complications in interpreting solutions to the inviscid stability equations in relation to the viscous limit of the Orr–Sommerfeld system have been known for many decades[64]. Of note is that although the eigenvalues of Eq. 4.13 appear in complex conjugate pairs, due to the fact the equation is real-valued, these solutions do not represent damped modes. Rather they are solutions on a different branch of the complex plane resulting from a logarithmic singularity that exists in Tollmien's inviscid solutions[46]. For the inviscid computation there is a spectrum of neutral modes that arise as a result of a singularity at the critical layer. Trying to track the eigenvalues of interest through the real line ($c_i = 0$) is neither possible computationally given our iterative method (which requires isolated eigenvalues for rapid convergence), nor it it physically meaningful as the solutions exist on a separate part of the complex plane.

These singular modes are neutral due to the fact that the basic state velocity is real, and thus $U = c$ only on the real line. In order to track an eigenvalue below the real line, $c_i < 0$, these modes must be diverted downward and out of the way. If the goal is to have these singular modes at $c_i < 0$, it is necessary for $U \rightarrow U_c$, with $\mathrm{Im}(U) < 0$. This is accomplished via analytical continuation, mapping the eigenvalue problem from real y to complex y_c. If this deflection of y into the complex plane is chosen correctly, a complex basic state velocity will be obtained with a negative imaginary part, thus mapping the singular modes away from the region of interest.

Following Ref. [33], the wall normal coordinate y can be replaced with a complex value y_c:

$$y_c = y - iC\sqrt{y_{\max} y - y^2} \tag{4.36}$$

which results in a shallow arc into the complex plane depending on the amplitude of the parameter C. For this new y_c, complex-valued Chebyshev polynomials can be created to solve the collocation problem, as the analytical continuation of a polynomial is straightforward. While not available explicitly, the complex basic state U_c can be found numerically using analytical continuation (via a Taylor Series):

$$U_c = U_r + iy_i \frac{\partial U_r}{\partial y} \quad . \tag{4.37}$$

As the eigenvalues approach the neutral point, increasing values of C can be used to deflect the singular modes away and allow for the unambiguous computation of the neutral curve for the inviscid solutions.

D. Energy Analysis

The Navier–Stokes Equations can be manipulated to derive an evolution equation for the total perturbation kinetic energy. This energy equation holds for all flows, and is not a linearized approximation.

$$\frac{dE}{dt} = -\int_V \left[\boldsymbol{u}'\boldsymbol{u}' \colon \nabla \boldsymbol{U} + \frac{1}{Re} \left(\nabla \boldsymbol{u}' \colon \nabla \boldsymbol{u}' \right) \right] dV \tag{4.38}$$

Defining the perturbation kinetic energy density as $e' = (u'^2 + v'^2 + w'^2)/2$ it is possible to derive an evolution equation for the total perturbation kinetic energy in terms of the disturbance modes that isolates the production mechanisms.

Following Ref. [34], the total energy in a given wavelength for a basic state

$\boldsymbol{U} = [U(y,z), 0, 0]$, can be written:

$$\frac{dE}{dt} = T_y + T_z - D \tag{4.39}$$

where the terms in Eq. 4.39 are integrated values for the total disturbance energy and the its production and dissipation:

$$\begin{aligned}
E &= \frac{1}{\lambda_x \lambda_z} \int_0^{\lambda_z} \int_0^{\infty} \int_0^{\lambda_x} e' \, dx\, dy\, dz & (4.40)\\
T_y &= \frac{1}{\lambda_x \lambda_z} \int_0^{\lambda_z} \int_0^{\infty} \int_0^{\lambda_x} (-u'v') \frac{\partial U}{\partial y} \, dx\, dy\, dz & (4.41)\\
T_z &= \frac{1}{\lambda_x \lambda_z} \int_0^{\lambda_z} \int_0^{\infty} \int_0^{\lambda_x} (-u'w') \frac{\partial U}{\partial z} \, dx\, dy\, dz & (4.42)\\
D &= \frac{Re^{-1}}{\lambda_x \lambda_z} \int_0^{\lambda_z} \int_0^{\infty} \int_0^{\lambda_x} (\nabla \boldsymbol{u}')^2 \, dx\, dy\, dz \quad . & (4.43)
\end{aligned}$$

$D = 0$ in the inviscid limit as $Re \to \infty$. The integrals are computed by substituting in the normal modes expansion defined previously. The integral in the x direction can be removed as the velocity components have no x dependence. This gives the system in terms of the complex quantities available from solving the eigenvalue problem.

$$
\begin{aligned}
Ee^{-2\omega_i t} = \tilde{E} &= \frac{1}{\lambda_z}\int_0^{\lambda_z}\int_0^{\infty}(\tilde{u}\bar{\tilde{u}} + \tilde{v}\bar{\tilde{v}} + \tilde{w}\bar{\tilde{w}})\,dy\,dz && (4.44)\\
T_y e^{-2\omega_i t} = \tilde{T}_y &= \frac{-1}{\lambda_z}\int_0^{\lambda_z}\int_0^{\infty}(\tilde{u}\bar{\tilde{v}} + \bar{\tilde{u}}\tilde{v})\frac{\partial U}{\partial y}\,dy\,dz && (4.45)\\
T_z e^{-2\omega_i t} = \tilde{T}_z &= \frac{-1}{\lambda_z}\int_0^{\lambda_z}\int_0^{\infty}(\tilde{u}\bar{\tilde{w}} + \bar{\tilde{u}}\tilde{w})\frac{\partial U}{\partial z}\,dy\,dz && (4.46)
\end{aligned}
$$

Substituting these equations into Eq. 4.39 gives a relationship between the temporal growth rate ω_i and the kinetic energy measures.

$$
\omega_i = \frac{\tilde{T}_y}{2\tilde{E}} + \frac{\tilde{T}_z}{2\tilde{E}} \tag{4.47}
$$

Eq. 4.47 serves two purposes. First, it is a useful check on the accuracy of the eigenvalue computation. Since the eigenvalue problem is solved for pressure and then transformed back to full two-dimensional velocity fields, agreement between Eq. 4.47 and the eigenvalue solution is an indication of accuracy. Second, Eq. 4.47 reveals the physical mechanisms responsible for the energy growth in the secondary disturbances.

E. Numerical Tools

Several numerical tools are developed to carry out the secondary instability and and energy analysis outlined in this section. Some details of the codes can be found in the Appendix B.

IRAM Drivers Computational routines for solving large-scale eigenvalue problems using shift-invert and generalized Cayley transforms for generalized, complex, non-symmetric eigenvalue problems using an Implicitly Restarted Arnoldi Method

General Inviscid Floquet Solver Inviscid stability analysis of spanwise periodic, wall-normal non-homogeneous basic states, allowing specification of the number of wall-normal points, grid clustering, number of basic state modes and number of solution modes

(Anti) Symmetric Floquet Solver For fundamental secondary instabilities ($\gamma = 0$), symmetry is exploited to double the spectral resolution at comparable computational cost.

Contour Deflection Floquet Solver Analytic continuation is employed to deflect singular neutral modes off the real line and calculate the neutral curves for secondary instabilities.

Post-Processing Routines Results from the above solver are processed to validate eigenfunctions via energy analysis, and provide two and three-dimensional output that can be analyzed in Tecplot in addition to standard plotting routines.

CHAPTER V

SECONDARY INSTABILITY RESULTS

The methods outlined in the previous chapter are used to study three separate base flows. The goal is to identify the main differences between optimal transient growth predictions and roughness-induced transient growth, and examine their effects on secondary instability behavior. There are four primary differences examined in this chapter. First, roughness-induced perturbations occur lower in the boundary layer than optimal perturbations, and the effect of this location is analyzed. Second, roughness-induced perturbations are more complex than optimal perturbations. Multiple spanwise modes are generated by each roughness element as opposed to single mode optimal perturbations. Third, the effect of the magnitude of the transient growth is evaluated to determine the onset of the secondary instability, and finally the effect of different spanwise modes evolving downstream at different rates is addressed.

The first baseflow is a simplified model of a streaky boundary layer. It consists of the superposition of the Blasius profile with an optimal perturbation, scaled to different heights in the boundary layer. This approach gives insight into the importance of perturbation location. The second basic state will be the flow in the mid wake of the roughness element with velocity profiles generated by DNS. This complex boundary layer will include many spanwise harmonics and characterize the range where the third harmonic, $\lambda_k/3$, is the dominant flow structure. The third baseflow will be further downstream, where the fundamental spanwise mode, λ_k, is dominant.

A. Model Boundary Layer

Despite differences in initial conditions that lead to optimal or sub-optimal transient growth, the resulting “streak” profile in the streamwise velocity is relatively consistent. In fact, the resulting streak profile is similar whether perturbations are generated by free-stream turbulence, roughness, blowing and suction, or other means[29]. Due to this, a generic streak is ubiquitous not only in laminar boundary layers but in turbulent boundary layers as well. One important difference found by White[14] is that the maximum amplitude of sub-optimal perturbations occurs lower in the boundary layer than optimal predictions. Further work by Fransson et al.[35] showed that compressing an optimal initial condition lower in the boundary layer led to energy growth more consistent with experimental results. This connection between the wall-normal streak location and reduced energy growth was confirmed via multimode decomposition[54].

Given the important link between the optimality of perturbations and their location in the boundary layer relative to the wall, a simple model for contrasting optimal perturbations with sub-optimal perturbations is to stretch or compress a generic streak, found either via DNS, experiment or optimization. In spite of the fact this representation is not self-consistent as an input condition, the output provides a straightforward means of contrasting optimal and sub-optimal transient growth. Fig. 26 shows a streak profile with different wall-normal scalings, with the initial streak found by solving the optimization problem, Eq. 2.21. Compressing the streak downward, gives a streak that is increasingly closer to the experimental conditions. Therefore, a simple model is to calculate the stability behavior of the model boundary layer for different scalings.

The optimal perturbation is computed for a zero-pressure gradient, flat-plate boundary layer. Following Ref. [30] the case considered is for $Re = 10^3$, $\beta = 0.45$, with the optimization length taken to be $x/\delta = 10^3$. This is different than the conditions used in Ref. [33] for secondary instability analysis, but it will be shown the results are similar. Fig. 27 shows excellent agreement with previous work. The left figure is the input perturbation, and consists of a streamwise vortex with zero initial streamwise velocity perturbation. The right figure shows the output streamwise streak $10^3\delta$ downstream. The vortex with no streamwise velocity evolves into periodic accelerated and decelerated zones of streamwise velocity, i.e., streaks. The initial condition has purely real wall-normal velocity, and purely imaginary spanwise velocity, as the optimal perturbation is symmetric in v and anti-symmetric in w. The v and w components decay monotonically, while the streamwise velocity perturbation experiences undergoes initial growth before decay.

Figure 28 shows the superposition of the Blasius solution and the optimal output perturbation with maximum amplitude of 36% of the freestream velocity. The lines in Fig. 28 are streamwise velocity contours and show a decelerated zone, the low-speed streak, about $z = 0$.

Consistent with Ref. [33] the streak amplitude is given by:

$$A_s = \frac{1}{2}\left[\max u_{TG} - \min u_{TG}\right] . \tag{5.1}$$

When only one spanwise mode is present this measurement is well defined, and the maximum amplitude of the optimal perturbation is used to contrast different amplitudes of transient growth with previous work[33, 34]. In subsequent sections, with more complicated flowfields, the maximum spanwise root-mean-squared velocity will be used instead of the maximum amplitude to better account for the total disturbance energy. The best way to measure the "size" of the perturbation for more complicated transient growth is not readily apparent. While measuring the maximum amplitude does not account for increased complexity associated with multiple spanwise modes in the basic state, measuring the average of the perturbation will tend to underestimate more localized disturbances (e.g., as the roughness elements are spaced further apart). This should be kept in mind when comparing the results of the present work to other roughness configurations.

In reality, with an amplitude as large as 36% of streamwise velocity, there would likely be non-linear distortion of the mean flow. For the computations here, the "shape assumption" is employed, so potential non-linear distortion of the streak is not considered. This assumption has been used in secondary instability analysis for T–S waves[23] and streamwise streaks[33]. While not truly valid in a physical situation this assumption is sufficient for the qualitative analysis of the effect of streak height on the secondary instability, and can be compared to previous results. The assumption is more appropriate for the work presented here than previous work as the secondary instabilities will be apparent at lower streak amplitudes.

Figure 29 shows the two-dimensional mode shapes of the secondary instability for optimal transient growth. The thin solid lines are contours of the absolute value of streamwise velocity perturbation, with the largest magnitude in the center. This represents what would be measured as unsteady fluctuations with a hotwire. The thick line represents the basic state velocity at the critical layer, where the phase speed of the perturbation is equal to the basic state velocity $c_r = U(y, z)$. For the sinuous perturbation (left figure) the left and right lobes are out of phase, and each lobe is out of phase about the critical layer.

The physical meaning of this can be seen in Fig. 30. This is a top down view of a slice in the $x - z$ plane at constant $y = 2.2$. The contours here are streamwise velocity and include the streaky basic state and the secondary instability at a single instant in time. The sinuous mode oscillates side-to-side in the spanwise direction as the flow travels in the streamwise direction. This is in contrast to the varicose mode which oscillates in and out. These mode shapes compare very well with the results found in Ref. [33] despite the non-parallel method, and differences in Re and optimization length x_*.

The focus of the present work is primarily on the fundamental sinuous mode. While the fundamental varicose mode (right figure) is more unstable in this case, it has non-zero velocity at the wall, and would likely be strongly attenuated by viscosity. Further, previous work has isolated the central importance of the sinuous secondary instability in breakdown of streaks to turbulence (see Refs. [33, 65]). The sinuous instability of optimal transient growth has been explored previously and forms the basis of all subsequent work on transient growth. The differences between this case and roughness-induced transient growth is explored below.

Effect of Streak Height

Analyzing the effect of the streak height in the boundary layer is a simplified model contrasting optimal results with roughness-induced perturbations. Fig. 31(a) shows the dramatic effect of the re-scaling approach. Placing the streak lower in the boundary layer yields a substantial increase in the growth rate of the secondary instability. Here, c is the scaling parameter such that $y \rightarrow cy$ moves the perturbation lower in the boundary layer for $c < 1$. For a fixed streak amplitude, moving the location of the streak down by 10% doubles the growth rate of the secondary instability. Moving the streak down to $c \sim 0.5$, which is in line with the experiments of Ergin and White[52], results in a maximum growth rate nearly ten times greater than the optimal perturbation for this amplitude.

This rescaling also expands the range of wavenumbers, α, that are unstable. This is important because the range of unstable temporal frequencies is directly related to this range, and potential interaction with T–S instabilities relies on matching between these wavenumbers and frequencies. The larger the range of unstable wavenumbers, the greater the possibility for interaction.

The physical mechanism for the enhanced growth rate is seen by using the method outlined in Chapter IV. Fig. 31(b) shows the production based on meanflow gradients in the y direction, T_y, and the production based on z gradients, T_z. When summed and normalized by the total energy these two components give the growth rate. For a fixed wavenumber, $\alpha = 0.3$, Fig. 31(b) plots these values against the scaling parameter c. This figure shows that while the production of energy from the spanwise direction remains relatively constant, the production from wall-normal gradients changes from negative to positive as the perturbation is moved lower in the boundary layer. That is, in an optimal perturbation the wall-normal velocity gradients are *stabilizing* while in the sub-optimal case they contribute to the secondary instability growth.

This result is consistent with physical intuition. Rescaling the optimal perturbation in y does not change the spanwise gradients much; however, the wall-normal gradients change significantly. Optimal perturbation theory favors the perturbation with smaller y gradients in order to minimize dissipation of the streak, but the steeper gradients seen in the rescaling approach dramatically decrease the stability of the flow.

This trend can be seen at all wavenumber and amplitude combinations. Fig. 32 shows the neutral curve for the optimal and $c = 0.5$ case. The critical amplitude for the optimal case here is just over 28%, which is very similar to the result found in [33] (despite a non-parallel streak model and different Re and optimization length). In the present work, the critical amplitude for the sub-optimal perturbation is less than half that of the optimal perturbation, near 12.5% amplitude.

Given this, deliberately introducing high-amplitude streaks for use in delaying T–S waves is risky if the streaks are generated by roughness elements. This simple model shows how significantly more unstable the boundary layer is with the addition of sub-optimal perturbations. Future analysis of T–S stabilization by streaks should also include potential interactions between the streak, the T–S wave, and the secondary instability to fully account for potential resonance. This will be discussed in more detail in the next section.

B. Near Wake

The second characteristic of roughness-induced transient growth that is distinct from optimal perturbation calculations is the complexity of the boundary layer. Unlike an optimal perturbation, the boundary layer in the wake of a roughness element contains energy in various spanwise wavelengths, each of which may be experiencing growth or decay at a location downstream. Using the DNS of Ref. [39] as the base flow 40 mm downstream of the roughness gives a profile significantly more complex than those both in the previous section, as well as earlier work. Not only is the dominant perturbation in the third harmonic, but many more spanwise wavelengths must be considered in order to resolve the basic state correctly. The inclusion of these additional basic state modes makes the problem increasingly interesting and more numerically complex. This complex behavior is illustrated in Fig. 33, where the energy of the different spanwise modes are rising and falling independently. Contrasting secondary instability results as the number of included spanwise modes are increased bridges the gap between an optimal perturbation and a roughness-induced perturbation.

Figure 34 shows contours of streamwise velocity found in Ref. [39] at two locations downstream of the roughness. Both these locations are in regions where the evolution of the perturbation is well described by linear theory. Fig. 33 shows the energy evolution of the dominant spanwise modes. After the nonlinear interactions in the near-wake region, by 40 mm downstream (mid wake, station 1) the third harmonic is the dominant energy component. Note that $x = 0$ is the roughness location, not the leading edge. Further downstream at 190 mm (far wake, station 2) the fundamental spanwise mode is dominant. Station 2 will be addressed in the next section.

The secondary instability approach outlined in Section 3 uses a Floquet expansion to express the base flow in its spanwise Fourier modes. Fig. 35(e) shows the energy content in each of the spanwise harmonics (based on the roughness element spacing, λ_k). At 40 mm downstream, the third harmonic is the dominant velocity component, followed by the fourth and so on. Determining how many spanwise modes to include in the basic state is not as straightforward as in the case of optimal perturbations where only one spanwise wavelength is considered.

The present work examines several cutoffs, both to ensure convergence of the eigenvalues, and to evaluate the effect of the increasingly complex behavior found behind more realistic roughness elements. Fig. 35 shows the streamwise velocity contours for various cutoffs, A–D at 40 mm downstream. Case A includes just the dominant transiently growing mode, Case B includes the first 4 modes etc. An attempt is made to make these breaks where natural, however the size of the banded matrix computed in the secondary stability calculations is determined by whether there is a common integer factor in the included modes. That is, the one mode computation for $\lambda_k/3$ can be computed with the same computational size as the fundamental wavelength simply by changing the spanwise wavenumber β used in the computation. Similarly $\lambda_k/3$ and $\lambda_k/6$ can be used with only a doubling of the non-zero matrix elements. However, a computation involving $\lambda_k/3$ and $\lambda_k/4$, cannot be reduced and thus, at least in terms of matrix structure, there is no reason not to also include the first and second harmonics. The secondary stability calculations are performed for the various number of modes shown in Fig. 35 for the basic state 40 mm downstream. For the second location, 190 mm downstream, only a case with a high number of spanwise basic-state modes is considered in the next section. This section looks at cases A–D, 40 mm downstream of the roughness elements.

Figure 36 shows the convergence behavior of the spanwise modes of the pressure fluctuation, $\hat{p}_k$ obtained by solving the eigenvalue problem, Eq. 4.13. For the fundamental sinuous instability, symmetry has been exploited to reduce the computational cost, and more than 45 spanwise perturbation modes are calculated. Fig. 36 shows that for all cases, roughly 30 spanwise modes are necessary to capture the full perturbation. All eigenvalue calculations are deemed converged if the residual is $\mathcal{O}(10^{-10})$, and the high spanwise mode numbers all fall below this threshold. Case A exhibits slightly different behavior, as it only includes 1 spanwise mode in the basic state, and that mode is not the fundamental.

1. Effect of Complexity

Figure 37(a) shows how, for fixed streak amplitude, the growth rate increases, and the band of unstable wavenumbers expands as more spanwise modes are included. The unstable secondary instability is able to extract more energy from the spanwise variation of the basic state as more modes are added. Here, Case A is the single-spanwise-mode approximation, including only the third harmonic. This boundary layer profile is similar to the rescaled optimal perturbation with $c = 0.5$. This agreement is good despite different β and Re of the basic state. For Cases B, C, and D, the increased complexity suggests the maximum root-mean-square of the disturbance velocity be used to measure the amplitude.

Figure 37(a) increases the amplitude of the DNS perturbation to keep the spanwise $u_{TG,\mathrm{rms}}$ at the same level as the 36% streak amplitude in previous computations, thus the amplitude of the $\lambda_k/3$ basic-state mode decreases from case to case, as the total rms disturbance is kept constant and more modes are added. Case A's amplitude is the same under both schemes. The results show much increased growth with realistically complex disturbances and that approximating a roughness-induced perturbation with a rescaled optimal perturbation is likely to greatly underestimate the growth rate. It should be noted that the amplitude used here is larger than the true amplitude from the DNS in order to make comparisons to previous optimal results.

Figure 38 shows how the mode shapes change as more spanwise basic state modes are included. The basic-state streak and perturbations becomes more localized. The fluctuations cluster around the steep gradients associated with the up-welling of low-momentum fluid, i.e. the low speed streak. It is this region that would begin to oscillate back and forth as the streak became unstable.

Interestingly, Fig. 38(a) shows that the most unstable sinuous instability for case A is really the 1/3 subharmonic, not a periodic arrangement of instabilities shaped like those in Fig. 29. This is shown further in Fig. 37(b), which plots this growth rate as a function of the Floquet detuning parameter γ. The 1/3 subharmonic ($\gamma = 1/3$) has a growth rate more than 35% higher than the fundamental. This contrasts with results found in Ref. [33] for optimal perturbations that in most cases the fundamental was the least stable, and that generally there was very little variation in growth rate. For sub-optimal perturbations, detuned modes can have significantly higher growth rates. Further, increased complexity expands the range of unstable α.

The increased complexity has another effect in addition to localizing the perturbation. Previous results (and the present work) for optimal disturbances show the existence of a single varicose and a single sinuous fundamental instability. For the more complex basic state found in the DNS a second sinuous and second varicose fundamental mode are found. Fig. 39 shows the mode shapes for these disturbances. Further, while the non-zero velocity components at the wall make the first fundamental varicose mode an unlikely candidate for generating boundary layer breakdown, the second varicose mode is localized away from the wall in an area where it may be sensitive to unsteady effects emanating from the top of the roughness element.

This type of instability could play a role in an as-yet-unseen varicose breakdown [65] related to strong gradients/separation from the top of a roughness element. More modes can be found with high amplitude basic states, but those are less unstable than those shown in Fig. 39.

2. Mode Validation

Figure 40 shows the dominant secondary instability at station 1 for the $Re_k = 202$ case, i.e. the true DNS condition. The colors here represent the absolute value of the $\tilde{u}$ fluctuations that would be measured by a hotwire. Fig. 41 shows similar unsteady contours, from the DNS and the experiment. The experimental contours are the time-averaged fluctuations, the DNS contours are an instantaneous snapshot. The secondary instability mode is the dominant wavenumber $\alpha = 0.086$, though it is representative of all the unstable frequencies.

Contrasting the secondary instability with the DNS shows the growth of the two lobes about the centerline. The experiment shows these two unstable lobes as well. Further, close examination shows that there are also bands of increased instability in the region where the basic state profile is two-dimensional, $|z/\lambda_k| > 0.25$, consistent with the outboard fluctuations in the secondary sinuous mode.

Despite this agreement, the sinuous secondary instability does not account for the central point of large fluctuation intensity along the centerline. While in the experiment this may be ascribed to the hotwires inability to resolve the small separation distance between the two out of phase lobes, this would not be a problem in the DNS. Thus it seems likely there is an additional unsteady feature in the flow that is not completely described by the sinuous secondary instability.

There are a few potential explanations for this. First, an additional instability related to to separation off the top of the roughness element could play a role. Second, though at this amplitude the second varicose mode is not amplified, in this region a potential interaction between that mode, a nascent T–S type instability, and the transient growth may be causing this feature. This possibility and its implications will be discussed in Chapter VI. Third, the basic state is evolving in the x direction, but the stability analysis is purely local. It is possible this x evolution is redistributing the fluctuating spanwise and wall-normal velocity components into the streamwise direction, resulting in seeming growth in the streamwise fluctuations.

It is important to note that the receptivity environments are quite different for the DNS and the experiment. The DNS includes no initial unsteadiness upstream of the roughness elements, whereas there is non-zero freestream disturbances in the wind tunnel. These differences can result in different secondary modes being preferred in the transition process as has been noted in many cases involving the transition of T–S and crossflow instabilities. The DNS did not store information about the fluctuating spectrum at this location, and the experiment does not do a good job of resolving the relative low temporal frequencies seen here. Future wind tunnel work to isolate some of these features will be discussed in Chapter VI.

3. Effect of Amplitude

Experimental work by White and coworkers[15, 52, 37] has established a receptivity scaling for transient growth behind an array of cylindrical roughness elements. The total kinetic energy (as well as the modal components) of the disturbance scales well with the roughness-height Reynolds number squared, Re_k^2. Further, these works show that the location of the perturbation in the wall-normal direction (the importance of which was discussed above) is only weakly affected by changing roughness height. In addition to this result, the theoretical analysis done in Ref. [47] using the DNS results of Ref. [39] demonstrated the linearity of the transient growth for $Re_k \sim 200$. The combination of these various results gives a physical meaning to rescaling the amplitude of the DNS results of Ref. [39] as a proxy for roughness height, and investigating the onset of unsteadiness as a function of Re_k. Performing a full DNS for a range of roughness heights numerically infeasible; however, combining theory, experiment and simulation can give some insight to an otherwise intractable receptivity problem.

Using the scaling of White, Rice and Ergin[15] to translate from disturbance amplitude to Re_k, the solid lines in Fig. 43 shows growth rate curves for the dominant sinuous perturbation as a function of non-dimensional frequency $F = \omega_r/Re$, and Re_k. The non-dimensional frequency is related to the dimensional frequency of the perturbation $F = 2\pi f\nu/U_\infty^2$, and is used to categorize the stability of T–S waves in a way that is independent of streamwise location. Here the Reynolds number is from the DNS 40 mm downstream of the roughness elements. The top axis shows the correlation between Re_k and the maximum disturbance amplitude. The low amplitudes that sustain unsteadiness are striking compared to the optimal perturbation which has a minimum critical amplitude of $\max(u_{TG,\mathrm{rms}}) \approx 0.2$ (see top axis of Fig. 32). From this figure it is clear that the boundary layer can exhibit instability at relatively low values of Re_k, and for frequencies in the T–S wave passband. Both experiments and computations[52, 39] observe transition for $Re_k \sim 335$, which lies in the region of instability, although in the experimental work the frequency range of interest was not closely examined, and the DNS did not retain frequency components.

The frequency range does compare favorably to that seen by Bakchinov[25] using rectangular instead of cylindrical roughness elements at much higher $Re_k \sim 750 - 1000$. Fig. 44 shows the secondary instability spectra from that experiment in physical space. For the first case, $Re_k = 750$, Fig. 43 shows the peak unsteadiness for $F \approx 200$, using $U_\infty = 8.2$m/s, and standard viscosity, the peak dimensional frequency $f \approx 135$Hz. This is consistent with the peak unsteadiness in this case. Similarly, using $U_\infty = 10\text{m/s}$ and $F \approx 225$ shifts the spectrum an appropriate amount to agree with the second spectrum plot for $Re_k = 1000$, $f \approx 225\text{Hz}$. This comparison is not rigorous, as these frequencies are being plotted at many different x locations with different Reynolds numbers and stability behavior. It does give some insight into how flow behind roughness elements may be somewhat universal.

Frequency analysis aside, what can be gleaned from Fig. 43 is that even relatively small-amplitude roughness can create transient disturbances that can sustain unsteadiness. Designing flow control methods using the beneficial stabilizing properties of streaks must be done with caution. If the streaks are created by streamwise vorticity generated by roughness elements, they will likely be sub-optimal and thus much more risky than calculations made using optimal disturbances would suggest. Further, the extent to which these streaks sustain unsteady disturbances that may interact with T–S waves and their secondary instabilities must be addressed in greater detail.

It should be noted that the boundary layer is evolving in the streamwise direction, and therefore not all values of α_r (and hence F) are physically meaningful. Low values of α_r (F) result in wavelengths longer than the development length of the transient growth, and are thus unphysical. Further, in order to trigger transition to turbulence, a perturbation must grow significantly before the nature of the basic state changes significantly. Ref. [52] outline how the transition process in the wake of these roughness elements is a competition between the growing unsteadiness and the inevitable decay of the transient growth. The secondary instabilities must reach a sufficient amplitude before the underlying velocity gradients dissipate. Thus relatively high growth rates are necessary in order for there to be significant boundary layer destabilization. The onset of unsteadiness alone is not enough.

The growth rate curves in Fig. 43 allow an order-of-magnitude N-factor estimate.

In experiments and DNS, transition is observed behind this configuration of roughness elements at roughly $Re_k \sim 350$. This region has a maximum temporal growth rate of approximately $\omega_i \approx 0.01$. Using Gaster's transformation, this can be related to a spatial growth rate $\alpha_i \approx \omega_i/c_r$ ($\partial c_r/\partial a_r$ is small). For the sinuous perturbations this gives $\alpha_i \sim 0.03$. This growth rate is an order of magnitude larger than T–S growth rates, and simple N factor correlations based on slower growth rates are likely suspect. However, examining Fig. 33, and noting that $\delta \approx 0.75$mm, the region dominated by the third harmonic is approximately 100δ in length. For this growth rate, that is a relatively small $N \approx 3$ for transition. As explained above, using this as a transition criteria would be complicated by the complex receptivity environment, as well as the centerline unsteadiness.

It should be noted that the transition location for these cases is extremely sensitive. The DNS[39] and later experiments[37] find transition relatively quickly in the mid-wake region, whereas Ergin and White[52] finds the onset of substantial turbulent fluctuations into the region where the fundamental spanwise mode is dominant. Differences in how the roughness elements were created is given as one reason for this, and illustrate how sensitive the transition location is to small changes. Thus, it is unlikely an e^N correlation will be able to capture these effects. Small unsteadiness around the roughness element would dramatically affect the receptivity in these regions. More work is required to define a workable transition criteria for these cases.

C. Far Wake

In experimental investigations of flow behind distributed and isolated roughness, a common parameter of interest is the "critical" Reynolds number. That is, the Reynolds number based on roughness element height that results in the transition location moving forward dramatically. Ref. [18] describes this behavior as critical because with a small change in the roughness height relative to the boundary-layer thickness the transition location jumps from its T–S dominated transition location to a location in the wake of the roughness element. Though this result was for isolated roughness elements, further work by others on periodic arrays of elements found similar behavior (see Ref. [9], and White and coworkers). Contrasting the mid wake with behavior in the far wake gives insight into this phenomenon.

As the perturbation continues to evolve downstream the fundamental spanwise mode begins to dominate, and this persists over a long distance. Station 2 in Fig. 33 provides a second important basic state to analyze for secondary instabilities. This region is more consistent with the optimal theory in that there is only one dominant mode, and it is the fundamental spanwise mode.

Figure 45 shows the mode shapes of the dominant far-wake modes, computed from the DNS basic-state 190 mm downstream of the roughness elements. It is important to note the difference in appearance of the dominant sinuous mode here in contrast with the dominant sinuous mode in the mid wake. In fact, the dominant mode here is the second sinuous mode in the mid-wake. That is, a significant amount of the perturbation is outboard of the streak structure. Therefore strong growth in the dominant mid-wake mode may not translate to strong fluctuations downstream. It is not known whether the mid-wake frequencies would also be dominant in the far wake and what effect this would have on the growth of secondary instabilities in this region.

The dashed lines in Fig. 43 shows that for a range of wavenumbers the boundary layer in the far wake of the roughness elements is significantly more stable than the mid wake. The minimum critical amplitude is more than double the case of the mid-wake. This provides a mechanism for understanding the sharp change in transition location observed in experiments. The far wake is significantly more stable than the mid-wake region 40 mm behind the elements, and is dominated by a different class of disturbance modes. As the height of the roughness element is increased, the transition location would skip this far-wake region and jump from the T–S dominated region to the mid-wake region dominated by rapidly-growing secondary instabilities shown in Fig. 38, resulting in the critical behavior seen experimentally. In fact, this result agrees well with the above comparisons between roughness-induced transient growth and the optimal perturbation method. The far wake is much closer to an optimal perturbation than the mid wake, in that there is a single dominant spanwise mode and it occurs higher in the boundary layer. Any configuration for which the far wake could cause transition would be even more unstable in the mid wake.

The long persistence of this region downstream makes it interesting for future work on the interaction between T–S waves and transient growth. Any instabilities in this region would have a large distance to grow and influence the T–S disturbances. It is likely that interactions in this region are responsible for the slight increase in transition location seen when subcritical roughness elements are placed in the flow, but don't initiate turbulence in the mid-wake region. How these interaction are impacted by potential upstream unsteadiness is also an open question. In DNS and some experiments, basic states such as this location have shown reduction in the growth rate of T–S waves. However, previous work has shown that transition is brought about by the onset of three-dimensional secondary instabilities, and the interaction of this part of the wake with those secondary instabilities is an important topic for future work.

D. Summary

This chapter has established several important results regarding the secondary instability of roughness-induced transient growth. First, optimal predictions dramatically over-estimate the stability of streaky boundary layers. If streaks are generated by roughness elements, they are substantially less stable than optimal disturbances, and thus optimal theory is not an appropriate "worst case" design estimate. Only detailed receptivity analysis can say how likely a particular roughness configuration is to cause transition. That is: "optimal" and "most-dangerous" are not synonymous. Second, the increased complexity of the roughness induced perturbations increases the growth rate of the instability when the maximum rms disturbance amplitude is kept fixed. Thus, a more complex perturbation, with the same total energy, is less stable. This results in simplified model perturbations also underestimating the growth rate of roughness-induced perturbations.

Using the energy scaling found by White and coworkers, the amplitude of the roughness elements is scaled to an effective perturbation amplitude. This scaling provided a neutral stability diagram that clearly contains the observed experimental unsteadiness in sub-critical and super-critical transient growth experiments. Finally, the mechanism for the "criticality" in flow behind roughness elements is explained by the changes in stability behavior between the mid wake and the far wake. The more stable far wake results in the transition location moving forward rapidly as the mid wake region goes unstable. These results encourage future work on receptivity and roughness effects, as well as the interaction between transient growth, T–S waves, and the resulting secondary instabilities.

CHAPTER VI

CONCLUSIONS AND FUTURE WORK

This dissertation has explored numerous factors that influence transition to turbulence in the wake of surface roughness. The fundamental results can be distilled into a single sentence. *While receptivity is non-linear, physically realizable transient growth is a linear process, and the resulting complex boundary layer is much less stable than optimal-theory predictions.* The remainder of this dissertation explored the causes and provided justification for this claim, as well as provided details of the resulting instability.

Chapter II outlined the mathematical preliminaries necessary for continuous spectrum analysis. For the first time it gave explicitly formulas for calculating the normalization constants for arbitrary continuous spectrum solutions. With the normalization constants and the adjoint solutions multimode decomposition was formulated rigorously. In addition, methods for calculating optimal perturbations were grounded in variational calculus and linear algebra, and linear receptivity methods were shown. A method for calculating receptivity functions for arbitrary, experimentally measured, disturbances was given for the first time.

Chapter III gave the results of a multimode decomposition for various cases and contrasted DNS, experimental and theoretical results. The continuous spectrum solutions proved capable of representing an arbitrary disturbance for multiple spanwise wavelengths. The decomposition showed the clear differences between optimal perturbations, linear receptivity, and physically-realistic transient growth. The extent of the receptivity region was determined, and the linear initial value problem was shown to describe the physics well downstream of this region.

A method for calculating the stability of the streaky boundary layer resulting from the transient growth was presented in Chapter IV. An inviscid Floquet expansion was developed for the purpose of studying sinuous secondary instabilities. Numerical methods were presented for solving large-scale eigenvalue problems resulting from this expansion and the computational effectiveness of this scheme was analyzed. Finally, the chapter outlined an energy analysis method to examine the physical mechanisms at work in the stability of boundary layer streaks.

Chapter V used the secondary instability analysis to examine both a model problem involving optimal streaks and two boundary layers obtained via the DNS. The model problem showed substantial destabilization of the boundary layer streaks as their location in the boundary layer moved closer to the wall, in closer agreement with experiments. The stability analysis of the DNS showed that increasing the complexity of the boundary layer resulted in increasing growth rate as well. Thus the two key distinctions between optimal perturbations and physically realistic transient growth the location and complexity of the streak, both underestimate the resulting instability. In addition, new mode shapes were found that could contribute to mode interaction in future analysis. Finally, analysis of the far wake behind the roughness element showed it to be significantly more stable than the region closer to the roughness, providing physical justification for the critical nature of roughness-induced transition.

A. Does Path C Exist?

Despite the conclusions above, this dissertation does not make a conclusive case for the existence of transition via Path C in Fig. 1. The unsteady velocity contours found in the DNS and experiment in Chapter V agree well with the unsteadiness predicted by the secondary instability calculation. However, the present calculations cannot account for the unsteadiness found along the centerline of the roughness element found in both DNS and experiments. Thus it appears that while the instabilities discussed in this dissertation exist in the wake of these roughness elements, there are other instabilities present. The instability ultimately responsible for transition is not clear. In the transitional case analyzed by DNS, unsteadiness along the centerline played a dominant role, in transition experiments it seems that a combination of modes is at work. This distinction can be attributed to the very different receptivity environments, but it highlights the difficulties in isolating physical mechanisms.

The additional instabilities could be three-dimensional modes associated the rapidly changing flow field that exists in the near-wake of the element or with unsteadiness emanating from the roughness element. Another possibility is that the observed unsteadiness is the result of interaction among multiple modes. At the Reynolds number seen in these experiments, there is a slowly growing T–S instability (modulated somewhat by the transient growth), in addition to the unstable modes seen in this work. While the varicose modes seen in this work are either not amplified for $Re_k \approx 200$ (Mode 2) or the growth rate is non-physically large (Mode 1), a resonant interaction between them could greatly increase the growth rate. This behavior is seen in three-dimensional boundary layers distorted by crossflow instabilities in Ref. [57] and the potential for interaction exists in transiently growing boundary layers as well.

It is worth noting that the canonical transient growth setup analyzed in this dissertation is designed to produce large, measurable, transient growth. That is, the transient growth examined here is more dramatic than what would likely be seen on a realistic surface with random, distributed roughness. If transition in the present case is dictated by resonant interactions with “primary” and secondary instabilities, this would also be true in the realistic case. In fact it is less likely to be Path C transition as relatively large amplitudes are still required. It seems unlikely that realistic distributed roughness would create transient growth of sufficient amplitude to cause transition via purely secondary instabilities a la Path C.

What is more likely is that the mechanisms analyzed here interact with classical instabilities in a way that enhances the growth rate and onset of the three-dimensionality that is the harbinger of transition to turbulence. That is, the transient growth mechanism is what enables surface roughness to have profound effects on transition, but the purely linear analysis does not capture all of the complicated mechanisms necessary to describe roughness-induced transition.

B. Future Work

The complications outlined above suggest a wide array of future work to isolate the physical mechanisms at work in roughness-induced transition.

1. Computational

Many computational problems present themselves as natural outgrowth of the current work. First, expanding the two-dimensional stability calculation to viscous problems is an important next step. While the sinuous modes studied in the present dissertation should not be affected a great deal, the viscous code should produce a more realistic varicose Mode 1, as well as allow the computation of transient-growth modulated T–S waves. With these mode shapes available, a next step would be expanding to parabolized stability or interaction-type computations to analyze the effect of the various instability modes on one another. Many different types of interaction are possible and a full two-dimensional interaction problem is of great interest.

In addition, a coupled DNS/three-dimensional stability computation of the type proposed in Ref. [59] in the region of the roughness element could give insight into potential unsteady fluctuations generated by roughness element itself. These large-scale computations push against current computational limits but have the potential to analyze unsteady shedding/flow separation in these types of flows. One of main focuses of this work will be how to appropriately define the basic state about which to linearize the disturbance equations, and how to extrapolate the results of an individual calculation to broader classes of flows.

2. Experimental

The Klebanoff–Saric Wind Tunnel (KSWT) at Texas A&M is an ideal facility to try and isolate some of the mechanisms highlighted in this dissertation[66]. The low disturbance level in this facility should make it ideal for studying the onset of unsteadiness in the flow behind roughness elements. Previous work has either had difficulty isolating the particular frequencies of interest because of tunnel noise, or did not keep the complete time history necessary to compute the disturbance shapes in the frequency domain.

Future work in the KSWT can be done in combination with the present method of analysis to identify the likely instabilities, and possible apply forcing to increase the receptivity and make the secondary instabilities easier to observe. This type of detailed experimental work will also shed some light on the centerline unsteadiness. If the frequency of this centerline unsteadiness is the same as the sinuous instability, than the instability is potentially related to the same mode. If it is different, the combination can be explored via possible selection mechanisms that would produce the necessary frequency.

In addition to the secondary instability computations, detailed measurements on realistic roughness can be used as input to the experimental decomposition method described in Chapters II and III. The receptivity of the flow to “random” roughness such as that in Ref. [41] can be contrasted to the present work and reveal more information about the physics of the receptivity process. Hopes of general modeling will require consistent features be extracted from different roughness geometries. This can be done quantitatively via multimode decomposition.

3. Theoretical

There is a great deal of work still needed to develop transient growth "theory." The present work has shown that concept of optimal energy growth is inherently limited as it naturally insulates the resulting transient growth from secondary instabilities and does not accurately capture physically realizable transient growth. A key necessity for future theoretical work is to move away from an energy optimal toward an optimal defined by the likelihood of the perturbation to cause transition. It is the combination of the growth of the streamwise streak, and the growth of secondary instabilities of that streak that may cause transition. Formulating the optimization problem to find the maximum integrated growth rate of the resulting secondary disturbances would provide a way to make transient growth more physically meaningful as a design tool.

A second advance would be the ability handle more general roughness configurations with an eye toward modeling truly random features. In the case of finite perturbations generated by roughness this may be possible using the experimental decomposition methods and data from the KSWT. In the case of infinitesimal perturbations this means developing a solution to the linearized initial value problem for randomized surfaces. It is not clear at this point whether this will be satisfactory as flow over very small distributed roughness likely leads to energy growth via disturbance accumulation as opposed to true transient growth (see Ref. [51]), and the extent to which this can be included in present theories is an open question.

More generally, the mathematical abstractions necessary for the analysis outlines in Chapter II make continuous spectrum analysis somewhat daunting. However, the approach taken by numerical analysts (including parts of this dissertation) of simply allowing a Chebyshev collocation solver to discretize the continuous spectrum is limited in terms of future theoretical advances. Analysis of perturbations via continuous spectrum modes neglects some knowledge of the physics in the sense that it is known a-priori that the perturbations tend to zero in the free-stream. Exploiting this fact to generate more conceptually tractable "wave-packets," that nonetheless constitute a complete set for expanding an arbitrary perturbation would make this type of analysis easier to comprehend. If the continuous spectrum modes could be converted into a set of distinct wave-packet solutions this would eliminate the dual conceptual hurdles of an uncountable set of modes and as well as oscillatory behavior infinitely far from the wall. This would be an important step in converting transient growth analysis from a problem in applied mathematics to a true engineering tool.

APPENDIX A

MATRIX AND VECTOR COMPONENTS

$$\mathcal{L}_{OS} = \tag{A.1}$$

$$\begin{pmatrix} 0 & 1 & 0 & 0 & 0 & 0 \\ i(\alpha U-\omega)Re+\beta^2+\alpha^2 & 0 & ReDU & i\alpha Re & 0 & 0 \\ -i\alpha & 0 & 0 & 0 & -i\beta & 0 \\ 0 & -\frac{i\alpha}{Re} & \frac{-\beta^2-\alpha^2}{Re}-i(\alpha U-\omega) & 0 & 0 & -\frac{i\beta}{Re} \\ 0 & 0 & 0 & 0 & 0 & 1 \\ 0 & 0 & 0 & i\beta Re & i(\alpha U-\omega)Re+\beta^2+\alpha^2 & 0 \end{pmatrix}$$

where $D = \partial/\partial y$

$$\begin{aligned}
{}^{(1)}_{\infty}\phi_\alpha &= [\alpha, \lambda_1\alpha, -i\lambda_1, -\alpha, \beta, \lambda_1\beta]^T \\
{}^{(2)}_{\infty}\phi_\alpha &= [\alpha, \lambda_2\alpha, -i\lambda_2, -\alpha, \beta, \lambda_2\beta]^T \\
{}^{(3)}_{\infty}\phi_\alpha &= [1, \lambda_3, -i\alpha/\lambda_3, 0, 0, 0]^T \qquad (A.2) \\
{}^{(4)}_{\infty}\phi_\alpha &= [1, \lambda_4, -i\alpha/\lambda_4, 0, 0, 0]^T \\
{}^{(5)}_{\infty}\phi_\alpha &= [0, 0, -i\beta/\lambda_5, 0, 1, \lambda_5]^T \\
{}^{(6)}_{\infty}\phi_\alpha &= [0, 0, -i\beta/\lambda_6, 0, 1, \lambda_6]^T
\end{aligned}$$

$$\begin{aligned}
{}^{(1)}_{\infty}\psi_{\alpha} &= \left[0, \alpha^2, -i\alpha\lambda_3^2, -iRe\alpha\lambda_1, 0, \alpha\beta\right]^T \\
{}^{(2)}_{\infty}\psi_{\alpha} &= \left[0, \alpha^2, -i\alpha\lambda_3^2, -iRe\alpha\lambda_2, 0, \alpha\beta\right]^T \\
{}^{(3)}_{\infty}\psi_{\alpha} &= \left[iRe\lambda_3\alpha, -\alpha(Re - i\alpha), i\alpha\lambda_3^2, iRe\alpha\lambda_3, 0, -\alpha\beta\right]^T \qquad \text{(A.3)} \\
{}^{(4)}_{\infty}\psi_{\alpha} &= \left[-Re\lambda_4\alpha, \alpha(Re - i\alpha), -\alpha\lambda_4^2, -Re\alpha\lambda_4, 0, -i\alpha\beta\right]^T \\
{}^{(5)}_{\infty}\psi_{\alpha} &= \left[0, i\alpha\beta, \beta\lambda_5^2, Re\beta\lambda_5, Re\lambda_5\alpha, i\beta^2 - Re\alpha\right]^T \\
{}^{(6)}_{\infty}\psi_{\alpha} &= \left[0, -i\alpha\beta, -\beta\lambda_6^2, -Re\beta\lambda_6, -Re\lambda_6\alpha, -i\beta^2 + Re\alpha\right]^T
\end{aligned}$$

$$\text{(A.4)}$$

$$\mathbf{A_1} = \begin{pmatrix}
0 & 1 & 0 & 0 & 0 & 0 & 0 & 0 & 0 \\
\beta^2 & 0 & ReDU & 0 & 0 & 0 & 0 & 0 & 0 \\
0 & 0 & 0 & -i\beta & 0 & 0 & 0 & 0 & 0 \\
0 & 0 & -\beta^2/Re & 0 & 0 & -i\beta/Re & 0 & 0 & 0 \\
0 & 0 & 0 & 0 & 0 & 1 & 0 & 0 & 0 \\
0 & 0 & 0 & -i\beta Re & 0 & \beta^2 & 0 & 0 & 0 \\
0 & 0 & 0 & 0 & 0 & 0 & 1 & 0 & 0 \\
0 & 0 & 0 & 0 & 0 & 0 & 0 & 1 & 0 \\
0 & 0 & 0 & 0 & 0 & 0 & 0 & 0 & 1
\end{pmatrix} \tag{A.5}$$

and

$$\mathbf{A_2} = \begin{pmatrix} 0 & 0 & 0 & 0 & 0 & 0 & 0 & 0 & 0 \\ URe & 0 & 0 & Re & 0 & 0 & -1 & 0 & 0 \\ -1 & 0 & 0 & 0 & 0 & 0 & 0 & 0 & 0 \\ 0 & -1/Re & -U & 0 & 0 & 0 & 0 & 1/Re & 0 \\ 0 & 0 & 0 & 0 & 0 & 0 & 0 & 0 & 0 \\ 0 & 0 & 0 & 0 & URe & 0 & 0 & 0 & -1 \\ -1 & 0 & 0 & 0 & 0 & 0 & 0 & 0 & 0 \\ 0 & 0 & -1 & 0 & 0 & 0 & 0 & 0 & 0 \\ 0 & 0 & 0 & 0 & -1 & 0 & 0 & 0 & 0 \end{pmatrix} \tag{A.6}$$

Conversion between 6x6 and 9x9

Using the definition of Ψ and the 9x9 system $\mathbf{A} = \mathbf{A}_1 + i\alpha\mathbf{A}_2$:

$$-\frac{\partial \Psi}{\partial y} = \mathbf{A}^T \Psi \tag{A.7}$$

the relation between the three additional adjoint terms, Ψ_{7-9}, can be found from setting the last three rows to zero:

$$\begin{aligned} \psi_7 &= i\alpha\psi_2 \\ \psi_8 &= -i\alpha/Re\psi_4 \\ \psi_9 &= i\alpha\psi_6\,. \end{aligned} \tag{A.8}$$

Evaluating the inner product $\langle \mathbf{A_2}\Phi, \Psi \rangle$ gives:

$$\langle \mathbf{A_2}\Phi, \Psi\rangle = \begin{bmatrix} 0 \\ URe\phi_1 + Re\phi_4 - i\alpha\phi_1 \\ -\phi_1 \\ -\phi_2/Re - U\phi_3 + i\alpha\phi_3/Re \\ 0 \\ (URe - i\alpha)\phi_5 \\ -\phi_1 \\ -\phi_3 \\ -\phi_5 \end{bmatrix} \begin{bmatrix} \psi_1 \\ \psi_2 \\ \psi_3 \\ \psi_4 \\ \psi_5 \\ \psi_6 \\ i\alpha\psi_2 \\ -i\alpha\psi_4/Re \\ i\alpha\psi_6 \end{bmatrix} \tag{A.9}$$

Rearranging to eliminate the additional rows

$$\langle \mathbf{A_2}\Phi, \Psi\rangle = -i[(iURe + 2\alpha)\phi_1\psi_2 + iRe\phi_4\psi_2 - i\phi_1\psi_3 - i/Re\phi_2\psi_4 - \ldots \tag{A.10}$$

$$(2\alpha/Re + iU)\phi_3\psi_4 + (2\alpha + iURe)\phi_5\psi_6)] \tag{A.11}$$

Which is identically equal to

$$\langle \mathbf{A_2}\phi, \psi\rangle = -i\left\langle \frac{\partial \mathcal{L}_{OS}}{\partial \alpha}\phi_0, \psi_\alpha \right\rangle \tag{A.12}$$

APPENDIX B

DETAILS OF NUMERICAL METHODS

Many numerical techniques are used throughout this dissertation. This appendix includes short explanations of some of the relevant features. The treatment is not meant to be exhaustive but more to define the terms and give appropriate references.

Chebyshev Collocation

There are several approaches to solving the differential eigenvalue problems outlined in this dissertation. Given an initial guess for the eigenvalue, integration methods can be used iteratively to converge on the true solution. This method allows control over the accuracy of the solution, but gives only one eigenvalue/vector at a time and requires a sufficiently good guess to iterate toward the true solution. The continuous spectrum solutions use integral methods because the eigenvalues are known a-priori and thus no iteration is required. The other eigenvalue problems addressed in this dissertation, the optimization and secondary instability problems, are better handled by first converting the differential eigenvalue problem to an algebraic eigenvalue problem, and then applying a method to obtain the eigenvalues from the resulting matrices. While initial discretization errors are introduced, when combined with a factorization method, the conversion to an algebraic eigenvalue problem provides the complete spectrum with no initial guesses for the eigenvalues.

Many methods are available to discretize eigenvalue problems, but Chebyshev pseudo-spectral collocation is a common choice in hydrodynamic stability. The most straightforward definition of the Chebyshev polynomials is via the recurrence relation:

$$\begin{aligned} T_0 &= 1 \\ T_1(y) &= y \\ T_n(y) &= 2yT_{n-1} - T_{n-2} \end{aligned} \tag{B.1}$$

However, to compute the solutions numerically the trigonometric definition is more easily computed:

$$T_n(y) = \cos(n\cos^{-1}(y)). \tag{B.2}$$

The polynomials are an orthogonal set in the region $y \in [-1 : 1]$ with the following relation

$$\int_{-1}^{1} \frac{T_n(y)T_m(y)}{\sqrt{1-y^2}}dy = \pi/2\delta_{nm} \tag{B.3}$$

and an arbitrary function can be represented as a sum of Chebyshev polynomials:

$$f(y) = \sum_{n=0}^{N} a_n T_n(y) \tag{B.4}$$

The sum of Chebyshev polynomials is substituted into the eigenvalue problem, and evaluated at N points in y to give an algebraic eigenvalue problem:

$$\mathbf{A}x = \lambda \mathbf{M}x \tag{B.5}$$

where each row represents a y location, and the unknown eigenvector x is the vector of Chebyshev coefficients. To maximize accuracy the collocation grid to be at the maxima of the highest order polynomial

$$y_j = \cos(j\pi/N) \tag{B.6}$$

where N is the number of polynomials used, and also the number of collocation points.

The domain is transformed from the Chebyshev domain to the physical domain using the rational map from Ref. [46] that clusters points in the boundary layer. Letting η be the wall-normal coordinate, and $y \in [-1:1]$ be the Chebyshev domain the map:

$$\eta = a\frac{1+y}{b-y} \quad a = \frac{\eta_i \eta_{\max}}{\eta_{\max} - 2\eta_i} \quad b = 1 + \frac{2a}{\eta_{\max}} \tag{B.7}$$

distributes half the grid between 0 and η_i. η_i and $\eta_{\max}$ are specified by the user.

Chebyshev polynomials are an attractive choice as their derivatives can be written as a sum of lower order polynomials:

$$\frac{d^k}{dy^k}(T_n(y)) = 2n\frac{d^{k-1}}{dy^{k-1}}(T_{n-1}) + \frac{n}{n-2}\frac{d^k}{dy^k}(T_{n-2}). \tag{B.8}$$

This allows a derivative of $f(y) = \sum_{n=0}^{N} a_n T_n(y)$ to be written as $\sum_{n=0}^{N} a_s D_{ns} T_n(y)$ where D_{ns} is a known differentiation matrix (post-mulitplication in matrix form if the y locations are stored in columns of T). The second, third and fourth derivatives can similarly be computed as powers of this D matrix.

$$D = \begin{bmatrix} 0 & 1 & 0 & 3 & 0 & 5 & 0 & 7 & 0 & 9 & \dots \\ 0 & 0 & 4 & 0 & 8 & 0 & 12 & 0 & 16 & 0 & \dots \\ 0 & 0 & 0 & 6 & 0 & 10 & 0 & 14 & 0 & 18 & \dots \\ 0 & 0 & 0 & 0 & 8 & 0 & 12 & 0 & 16 & 0 & \dots \\ 0 & 0 & 0 & 0 & 0 & 10 & 0 & 14 & 0 & 18 & \dots \\ \vdots & \vdots & \vdots & \vdots & \vdots & \vdots & \vdots & \vdots & \vdots & \vdots & \end{bmatrix} \tag{B.9}$$

For the spatial Orr-Sommerfeld problem, the discretization is applied to the linear first order form of the equations, Eq. 2.3, with three additional equations so the eigenvalue α appears linearly. Defining all the variables as a system x_i with $u = x_1$, $Du = x_2$, $v = x_3$, $p = x_4$, $w = x_5$, $Dw = x_6$, $\partial u/\partial x = x_7$, $\partial v/\partial x = x_8$ and

$\partial w/\partial x = x_9$. This yields the set of 9 equations for the 9 unknowns.

$$\begin{aligned}
Dx_1 - x_2 = 0 \qquad & Dx_5 - x_6 = 0 \\
Dx_3 + x_7 + i\beta x_5 &= 0 \\
Ux_7 + DUx_3 - Dx_2/Re + (\beta^2/Re - i\omega)x_1 &= \alpha\,[ix_7/Re - ix_4] \\
Ux_8 + Dx_4 + i\beta x_6/Re + (\beta^2/Re - i\omega)x_3 &= \alpha\,[ix_8/Re - ix_2/Re] \\
Ux_9 - Dx_6/Re + i\beta x_4 + (\beta^2/Re - i\omega)x_5 &= \alpha\,[ix_9/Re] \\
x_7 = \alpha\,[ix_1] \quad x_8 &= \alpha\,[ix_3] \quad x_9 = \alpha\,[ix_5]
\end{aligned} \tag{B.10}$$

The boundary conditions on the first and last 9 rows are given by

$$\begin{aligned}
x_{1,3,5,7,8,9} &= 0 \\
Dx_3 &= 0 \\
Dx_4 + Dx_7/Re + i\beta x_6/Re &= 0 \\
i\beta x_4 - Dx_6/Re &= 0
\end{aligned} \tag{B.11}$$

at the wall and infinity.

For the secondary instability eigenvalue problem, Eq. 4.13, the equations are left in second order form and the eigenvalue appears linearly so no additional terms are required.

Quadrature Integration

An additional benefit to using a spectral method for discretizing the problem is that spectrally accurate quadrature formulas can be derived to compute integrals based on the Chebyshev coefficients at the grid points. For a quadrature method the goal is to replace an integral with a weighted sum:

$$\int_{-1}^{1} f(y)dy = \sum_{j=0}^{N} f(y_j)W(y_j) \tag{B.12}$$

where the weighting coefficients W can be determined in advance from the polynomials. This approach is adopted from Ref. [67]. Using Eq. B.4, and the integrals of the polynomials:

$$\int_{-1}^{1} T_n(y)dy = \frac{2}{1-n^2} \qquad n \text{ even} \tag{B.13}$$

gives the weights:

$$W(y_j) = \frac{c_j}{2N}\left\{2 + \sum_{n=2}^{N} c_n \frac{1+(-1)^n}{1-n^2}\cos\left(\frac{nj\pi}{N}\right)\right\}. \tag{B.14}$$

here $c_0 = c_N = 1$ and $c_j = 2$ for $j \neq 0, N$. This can be expanded to calculate the integrals in the new mapped coordinates. Let η be the coordinates defined above, then the weights can be generalized:

$$W(\eta_j) = \frac{c_j}{2N}\sum_{n=0}^{N}\left\{c_n \cos\left(\frac{nj\pi}{N}\right)\int_{-1}^{1} T_n(y)\frac{d\eta}{dy}\,dy\right\}. \tag{B.15}$$

The integral term in Eq. B.15 is evaluated using the quadrature rule from Eq. B.14 to preserve the spectral accuracy. This quadrature integration is used to evaluate the integrals in the energy analysis.

Arnoldi Iteration

In addition to standard factorization methods, iterative methods are used in this dissertation to compute selected eigenvalues of large scale problems. These iterative methods do not give the complete spectrum, but rather rapidly find a desired subset of the spectrum, in this case the least stable eigenvalues. In contrast to a factorization method, iterative methods do not rely on reconstructing an entire matrix, but rather matrix-vector products which can be found efficiently. The brief development here will follow Ref. [61], and Ref. [68].

Consider the eigenvalue problem:

$$\mathbf{A}x = \lambda x \tag{B.16}$$

The simplest iterative method is power iteration where, starting with and initial guess x_0, the iteration simply replaces the current vector with a new vector $x_{i+1} \leftarrow \mathbf{A}x_i$. If, after rescaling to unit norm, $x_{i+1} = x_i$, an eigenvalue has been found. This method is simple to implement but is limited in terms of convergence properties and finding multiple eigenvalues.

A more sophisticated iterative scheme uses the notion that power series tend to converge to dominant eigenvalues to improve on this method. Instead of simply computing the power iterations, let $\mathcal{K}$ be a *Krylov Subspace*. The k-th Krylov subspace is defined:

$$\mathcal{K}_k = \text{span}\left\{x, \mathbf{A}x, \mathbf{A}^2x, \dots \mathbf{A}^kx\right\}. \tag{B.17}$$

That is, the vector space spanned by the iterations. Let $\mathbf{A} \in \mathcal{C}^{n\times n}$, and $\mathbf{V}_k \in \mathcal{C}^{n\times k}$ be an orthonormal basis extracted from $\mathcal{K}_k$ (using e.g. Gram-Schmidt) then for appropriately chosen basis the following relationship (Arnoldi Factorization) holds:

$$\mathbf{A}\mathbf{V}_k = \mathbf{V}_k\mathbf{H}_k + f_ke_k^T \tag{B.18}$$

where $\mathbf{H}_k \in \mathcal{C}^{k\times k}$ is upper-Hessenberg and the rank one error terms are orthogonal to $\mathbf{V}_k$. It can be shown[61] that the eigenvalues of $\mathbf{H}_k$ are the eigenvalues of $\mathbf{A}$ within a tolerance defined by the error f_k. These eigenvalues can be found quickly as $\mathbf{H}_k$ is smaller than $\mathbf{A}$ and already in upper-Hessenberg form. However, simply increasing k until convergence is unwieldy and would have large storage requirements as the problem grows.

To remedy this, a restarting procedure is implemented to periodically condense the "good" information from the iterative scheme. In this restarting let k be the number of eigenvalues desired, and m be the total number of Arnoldi vectors being used in the computation. After constructing the Arnoldi factorization, and thus $\mathbf{H}_m$, an implicitly shifted QR algorithm is applied to $\mathbf{H}_m$ with $p = m - k$ shifts. This pulls the eigenvector behavior out of the larger $\mathbf{H}_m$ into the first k rows/columns. The remaining p columns are then truncated and $\mathbf{H}_m$ is reformed using the Arnoldi factorization and the new k columns.

Thus the IRAM requires factorization methods on only a small subset of the total computation. In the present work $k < 10$ and $m < 40$ in all computations and typically $k = 1$ and $m = 10$ for the shift-invert computations. Thus all that is required is a rapid method of supplying the matrix-vector product necessary for creating the initial subspaces.

APPENDIX C

FIGURES

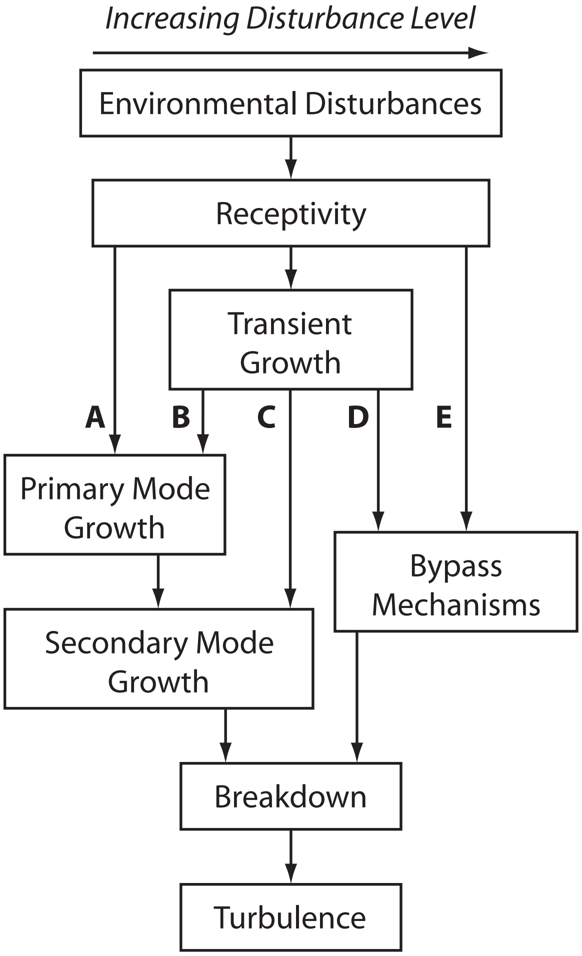

Fig. 1. Transition roadmap – adapted from Morkovin et al.[6]

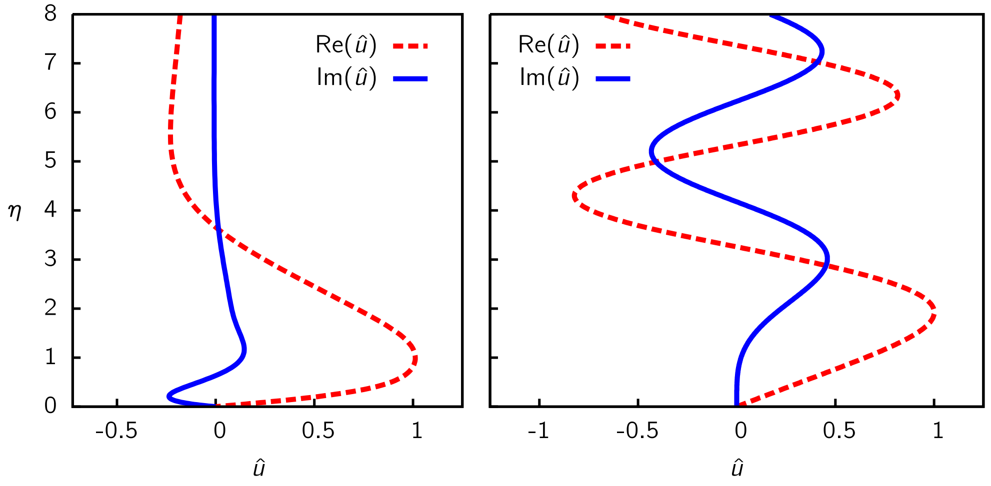

(a) Discrete

(b) Continuous

Fig. 2. Mode shapes of the Orr–Sommerfeld equation

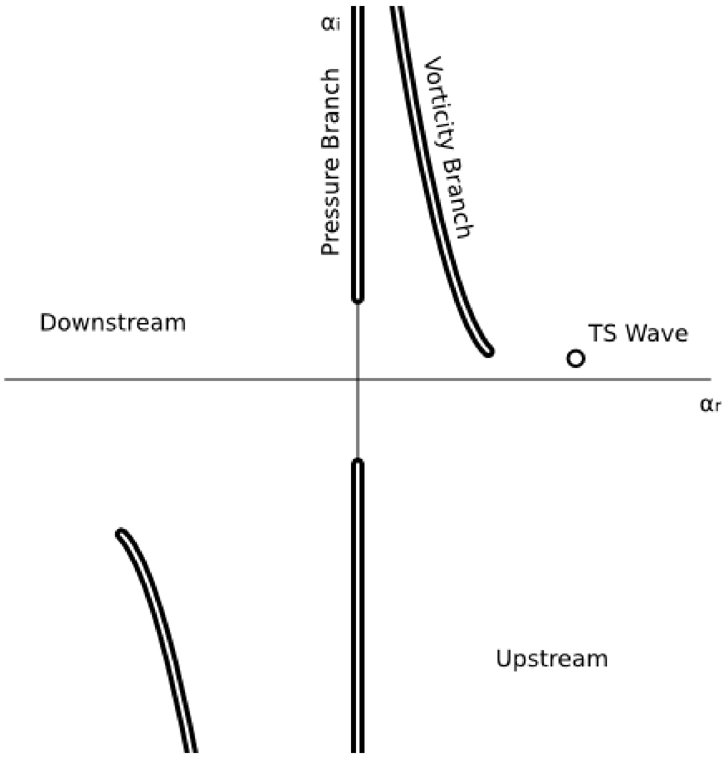

Fig. 3. Complex plane of the Orr–Sommerfeld equation for boundary layer flow

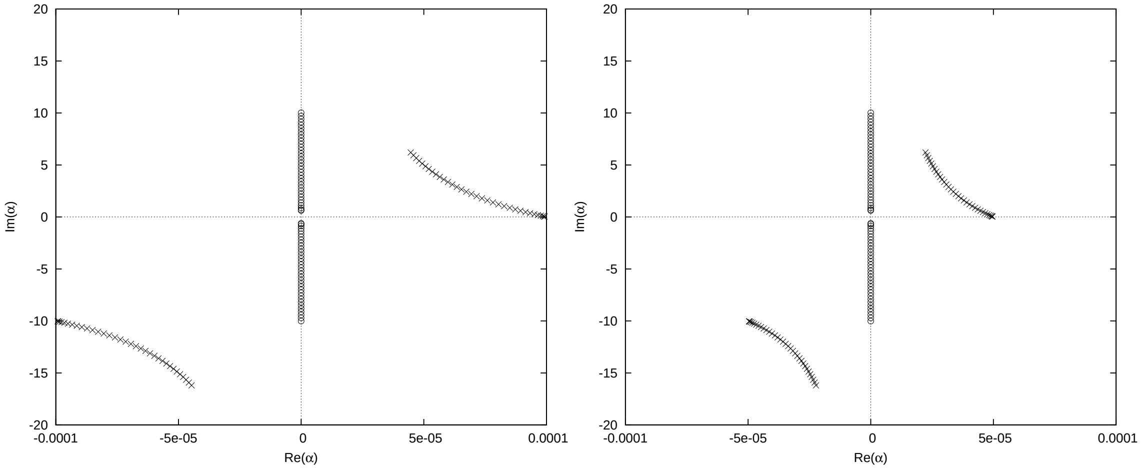

(a) $\omega = 10^{-4}$ (b) $\omega = 10^{-5}$

Fig. 4. Example branch cuts in the α plane – $Re = 10$, $\beta = 0.621$, $\kappa = 0 \rightarrow 10$ (κ for every branch is smallest at its closest point to the x-axis)

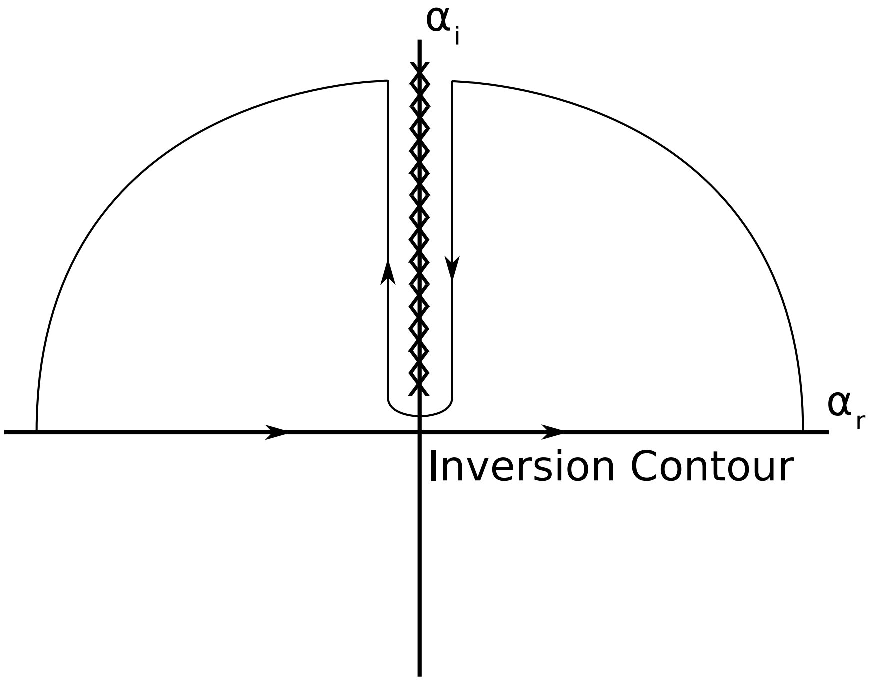

Fig. 5. Branch cut and inversion contour in the α plane for the current configuration, $\omega = 0$

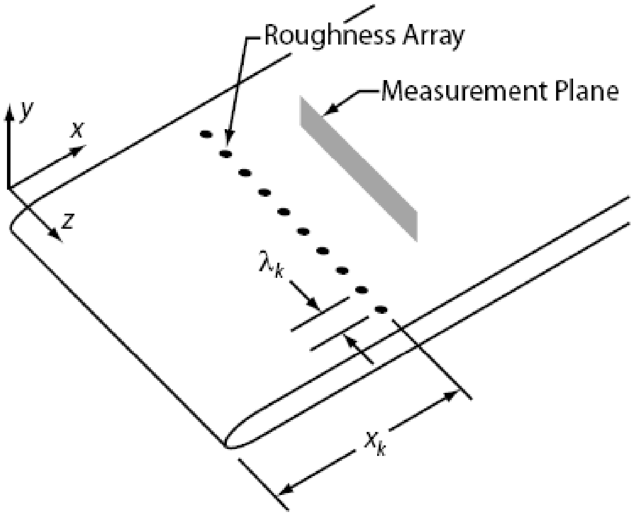

Fig. 6. Schematic of setup for experiment of Ref. [52] and DNS of Ref. [39]

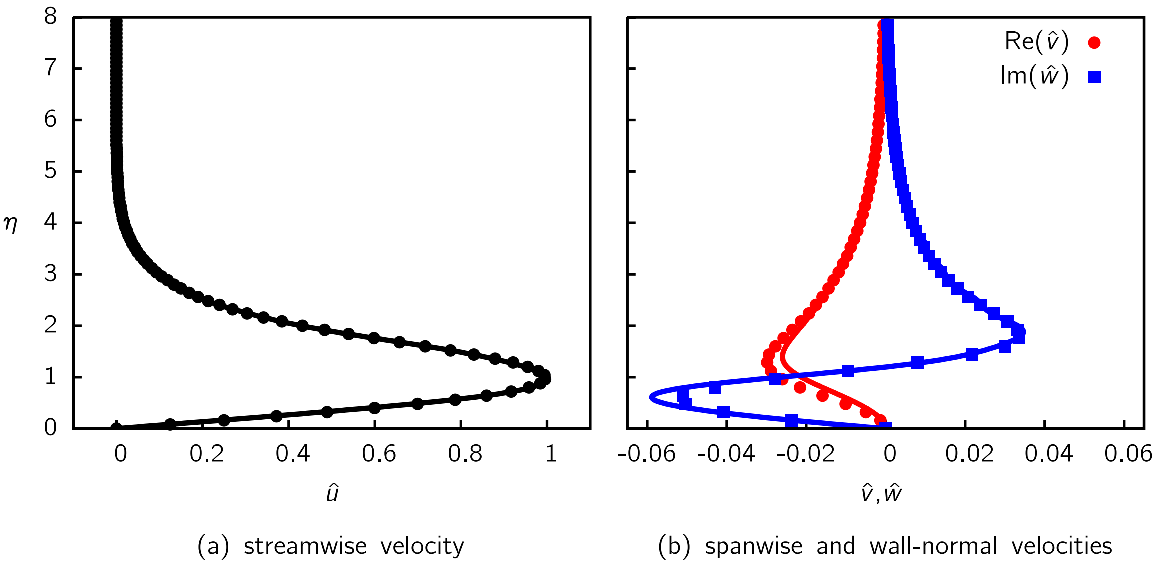

(a) streamwise velocity

(b) spanwise and wall-normal velocities

Fig. 7. Decomposition profiles – symbols are DNS of Ref. [39], lines are multimode decomposition

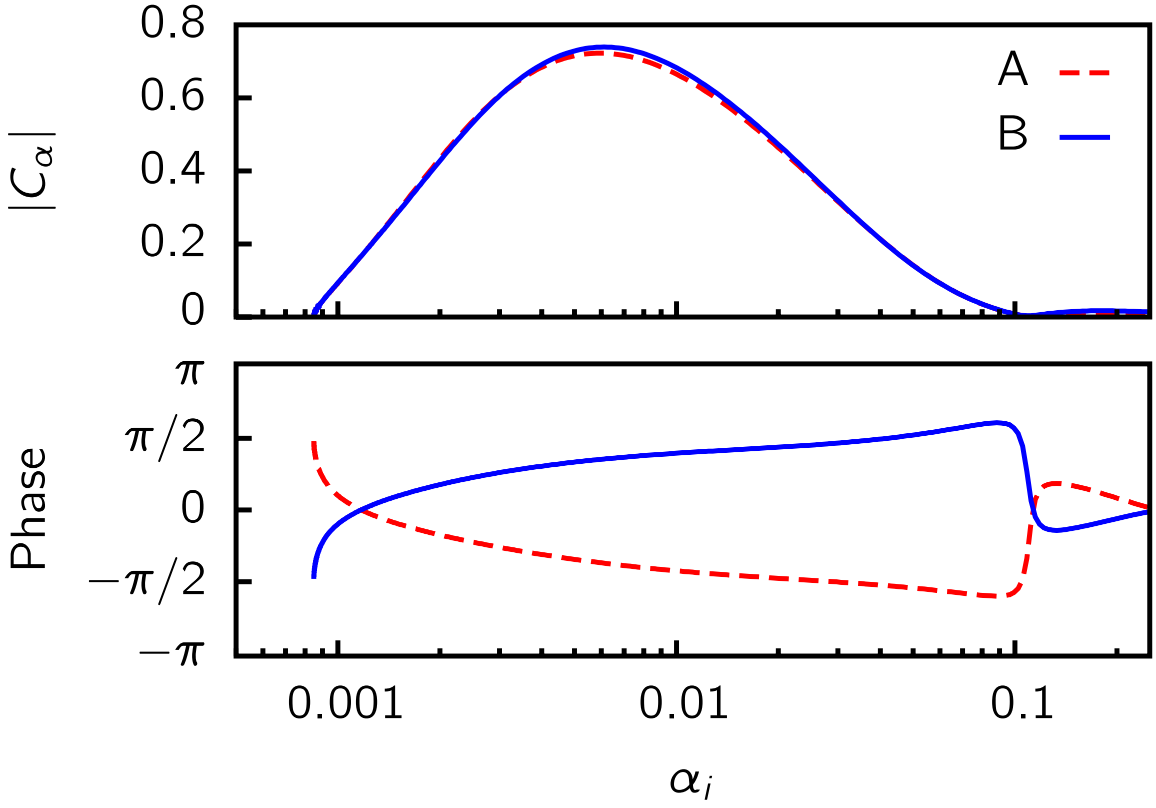

Fig. 8. Amplitude and phase of C_α for $\lambda_k/3$, 25mm downstream of the roughness elements

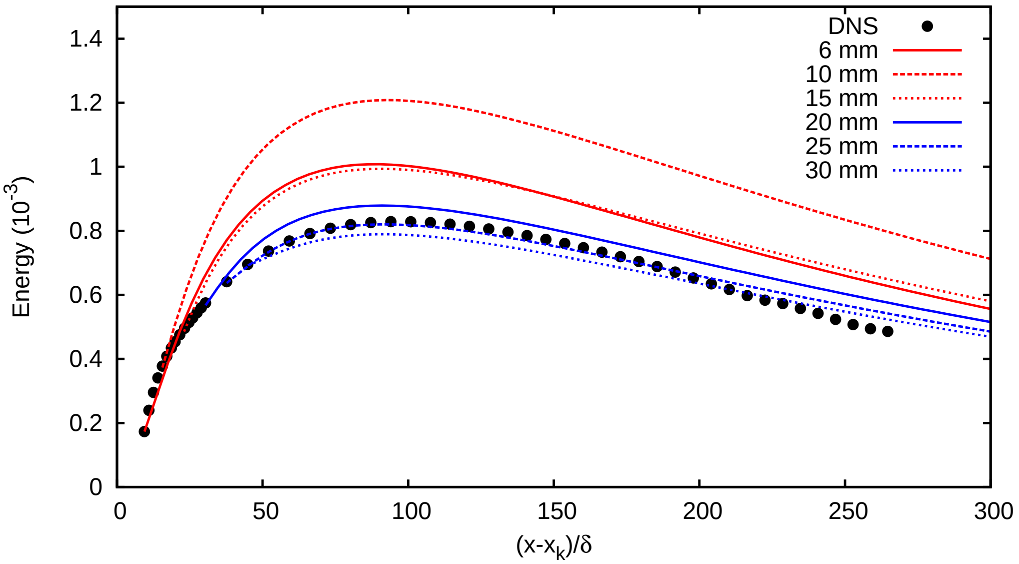

Fig. 9. $\lambda_k/3$ disturbance energy evolution for DNS and decomposition performed at various downstream locations

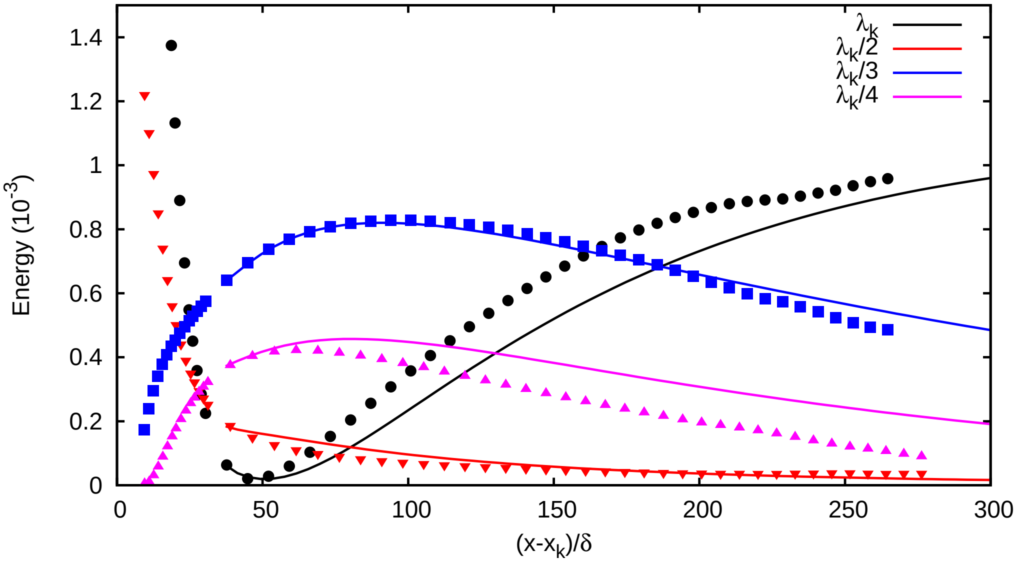

Fig. 10. Disturbance energy for the first four harmonics. Symbols are DNS; lines are reconstructions based on multimode decomposition 25mm downstream.

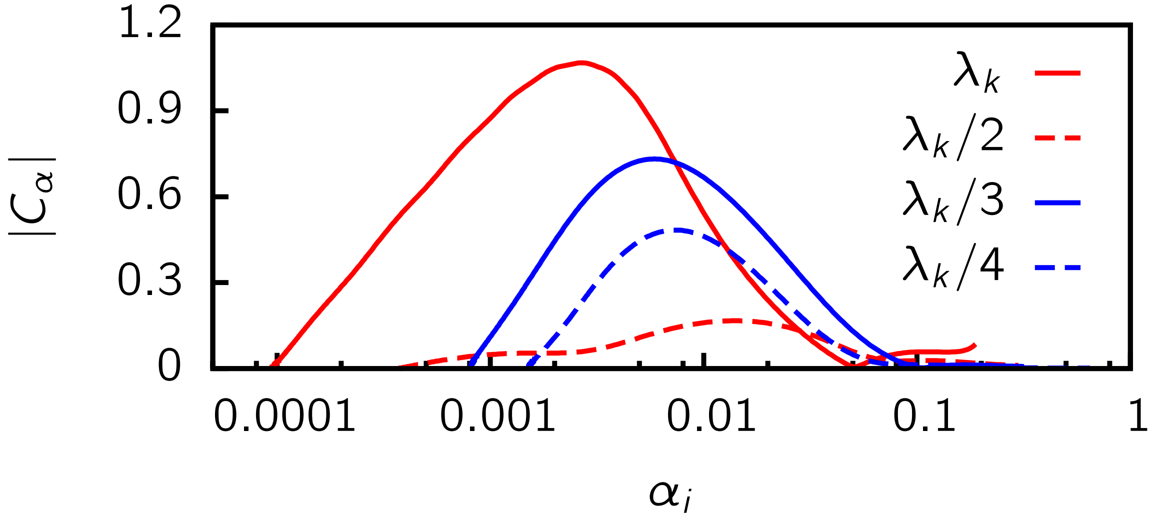

Fig. 11. 'A' branch amplitude distributions for the first four spanwise harmonics

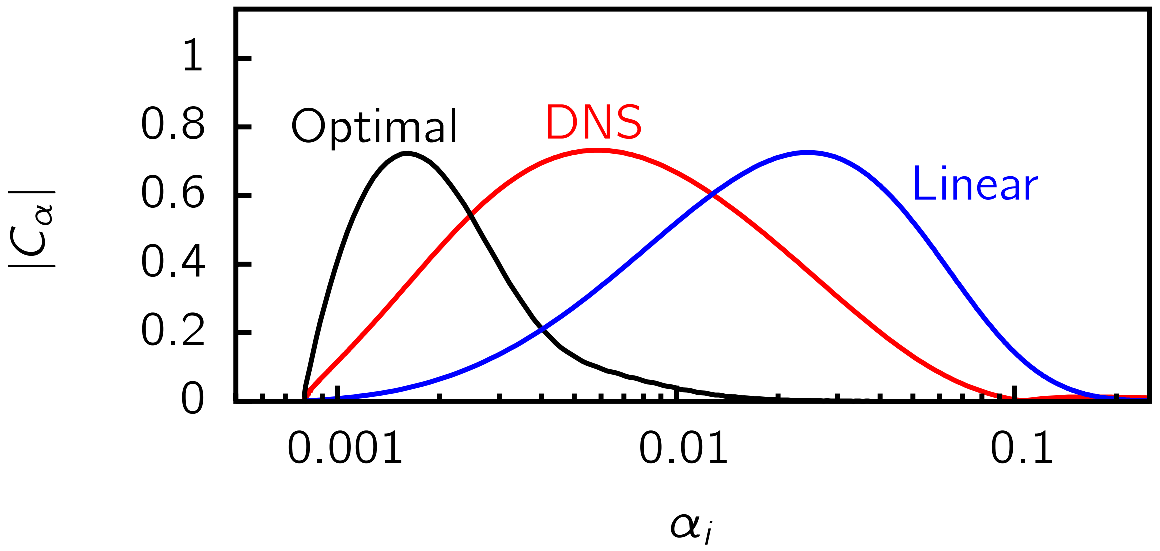

Fig. 12. Comparison of continuous spectrum amplitudes of the 'A' branch for optimal, DNS, and linear receptivity theory

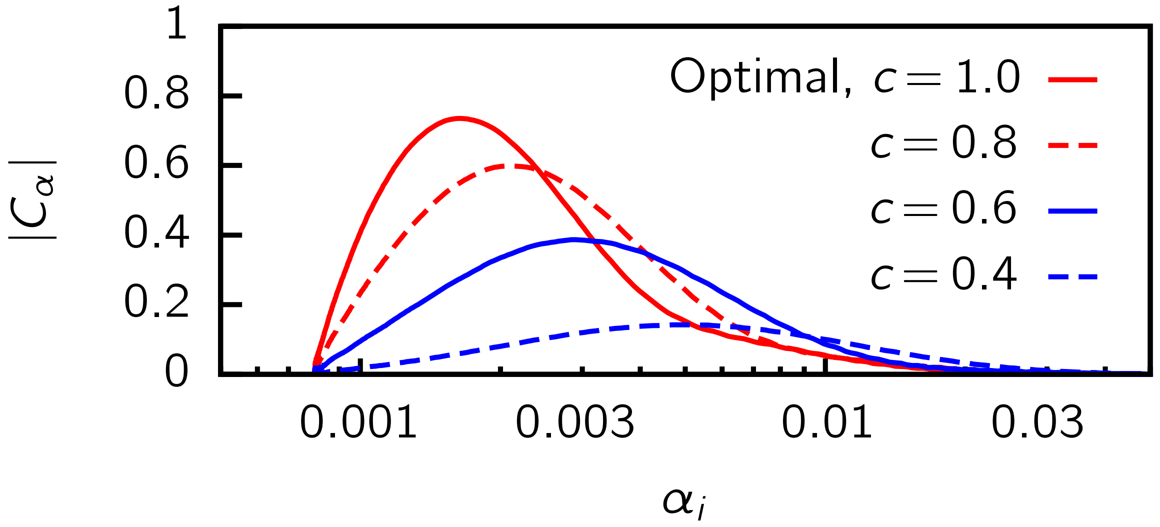

Fig. 13. Comparison of continuous spectrum amplitudes as an optimal disturbance is rescaled ($y \to cy$) to occur lower in the boundary layer

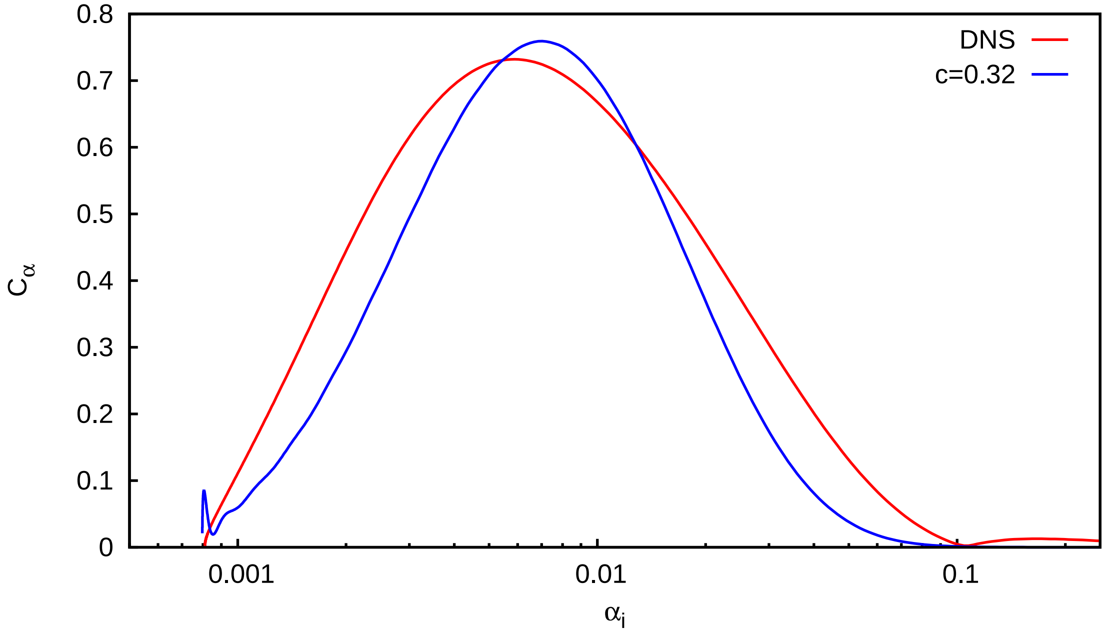

Fig. 14. $\lambda_k/3$ continuous spectrum amplitudes for the rescaled optimal disturbance in best agreement with DNS results (normalized differently than previous figure)

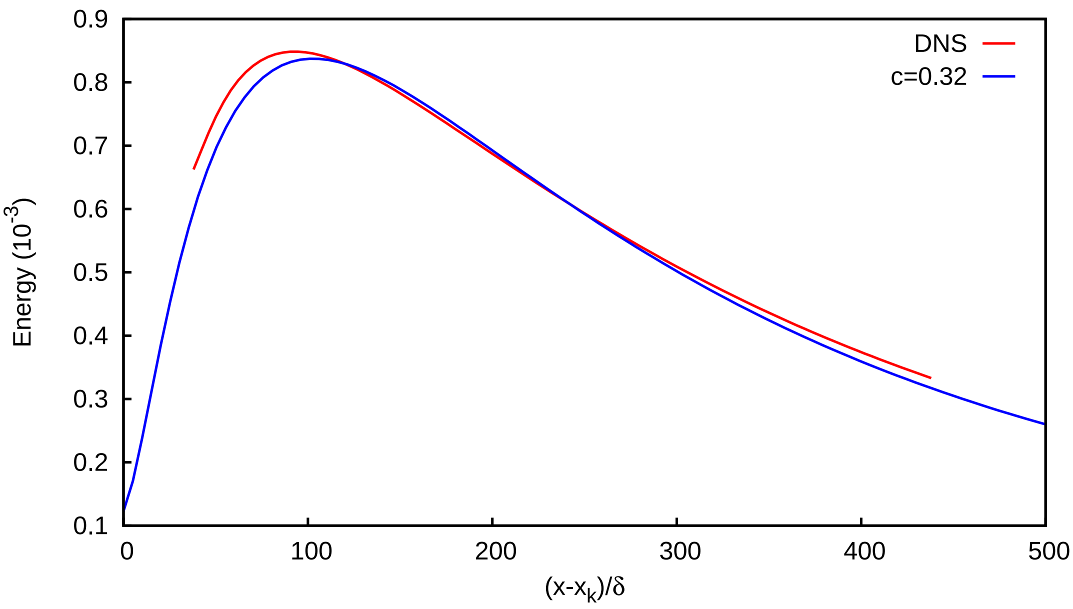

Fig. 15. $\lambda_k/3$ disturbance energy evolution for the rescaled optimal disturbance in best agreement with DNS results

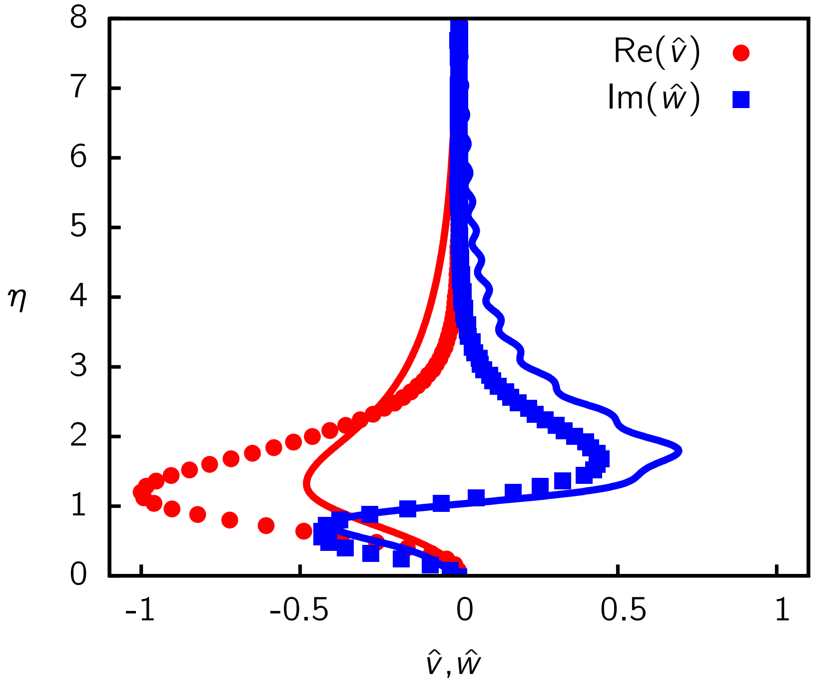

Fig. 16. Comparison of velocity profiles for rescaled optimal (symbols), decomposition (lines)

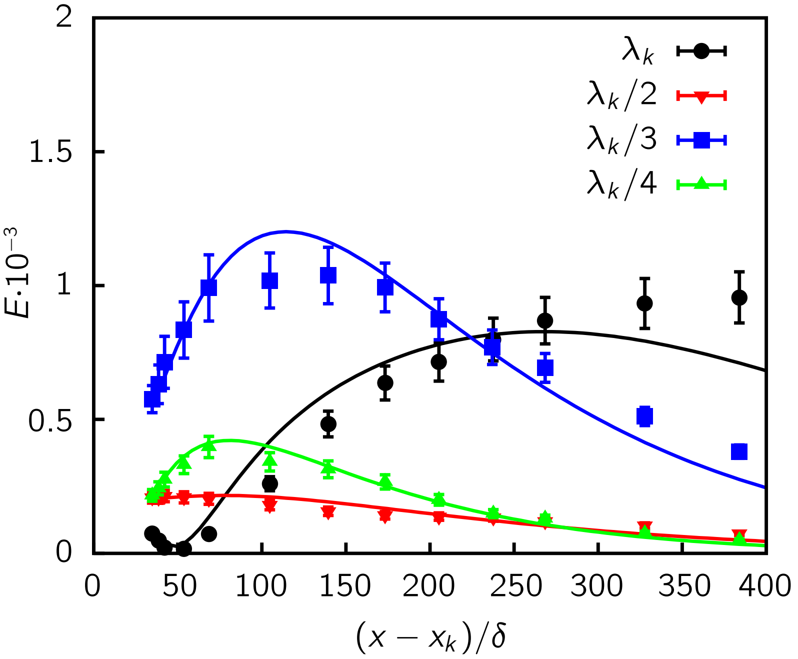

Fig. 17. Disturbance energy for the first four spanwise harmonics using the partial data Method

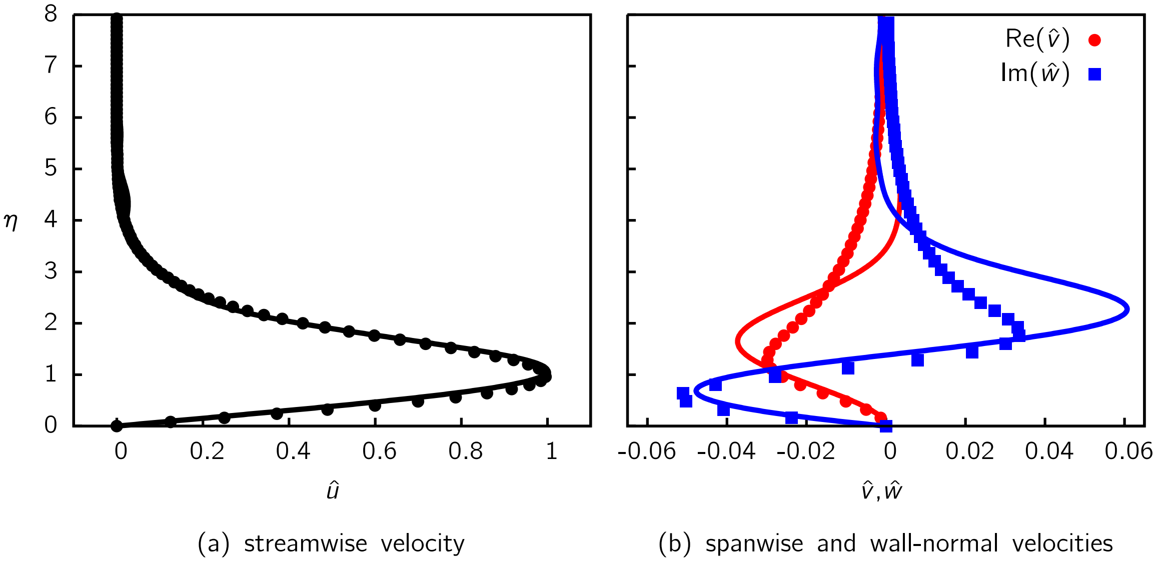

(a) streamwise velocity (b) spanwise and wall-normal velocities

Fig. 18. Comparison of partial data method (lines) with DNS (symbols) 25mm downstream of the roughness elements

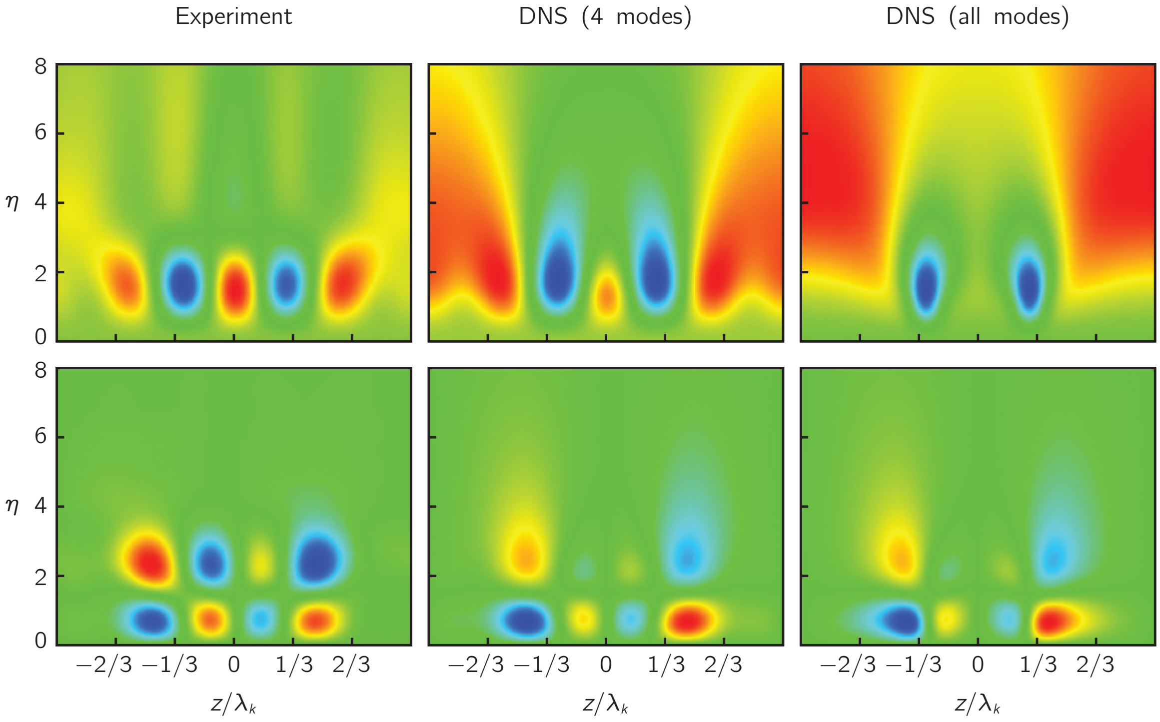

Fig. 19. Wall normal (top) and spanwise (bottom) velocity contours for experimental reconstruction, DNS with four dominant modes, and full DNS – 50 mm downstream

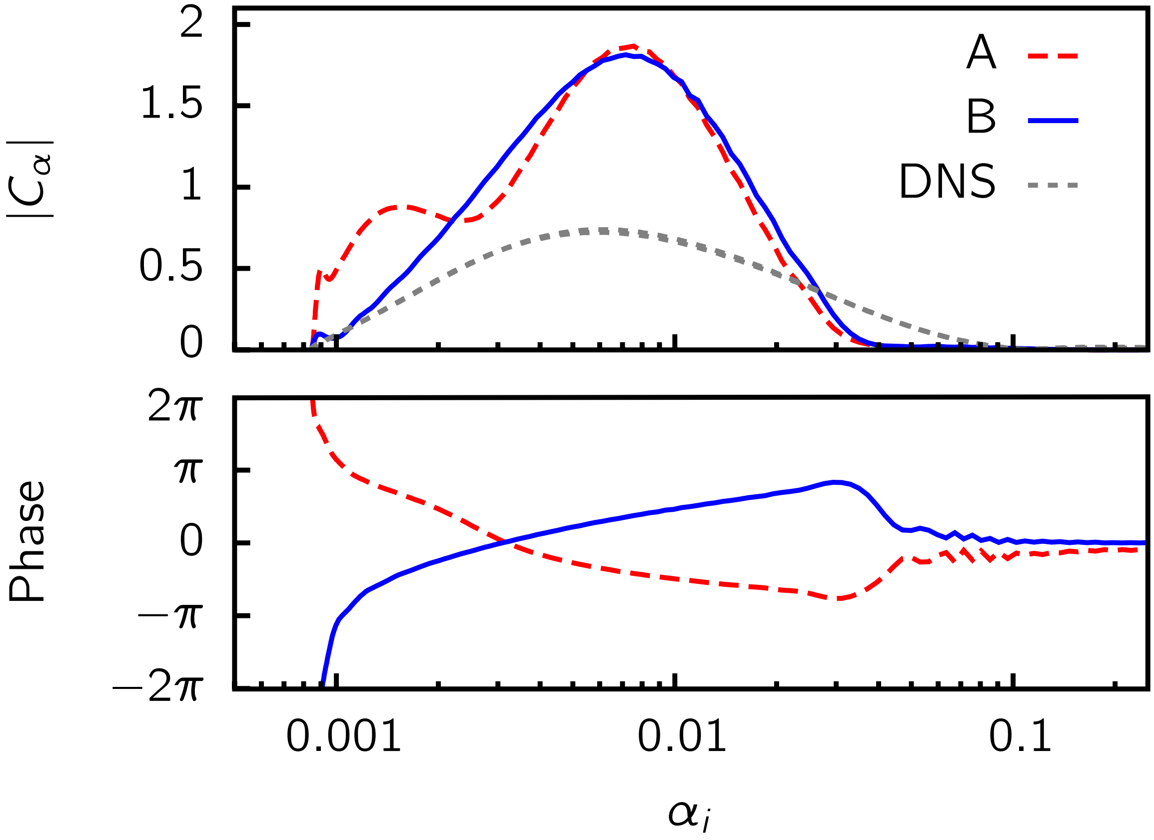

Fig. 20. Amplitude and phase of the coefficients of the continuous spectrum modes for $\lambda_k/3$ using the partial data technique

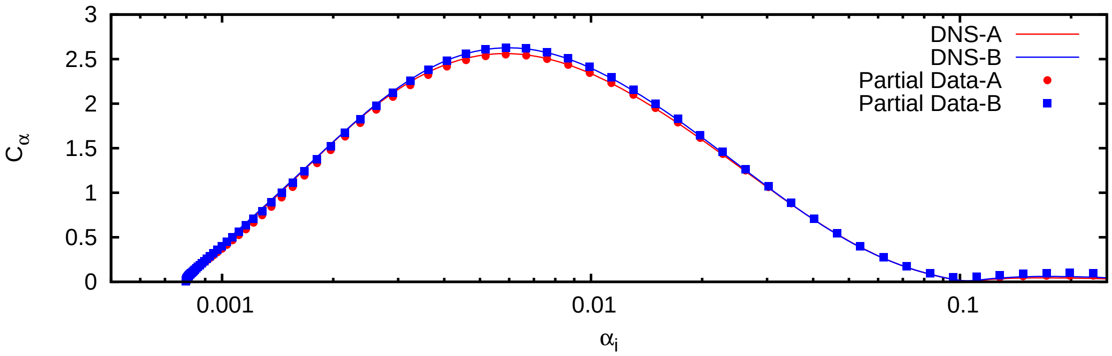

Fig. 21. Receptivity amplitude for $\lambda_k/3$, 25mm downstream using no pressure information

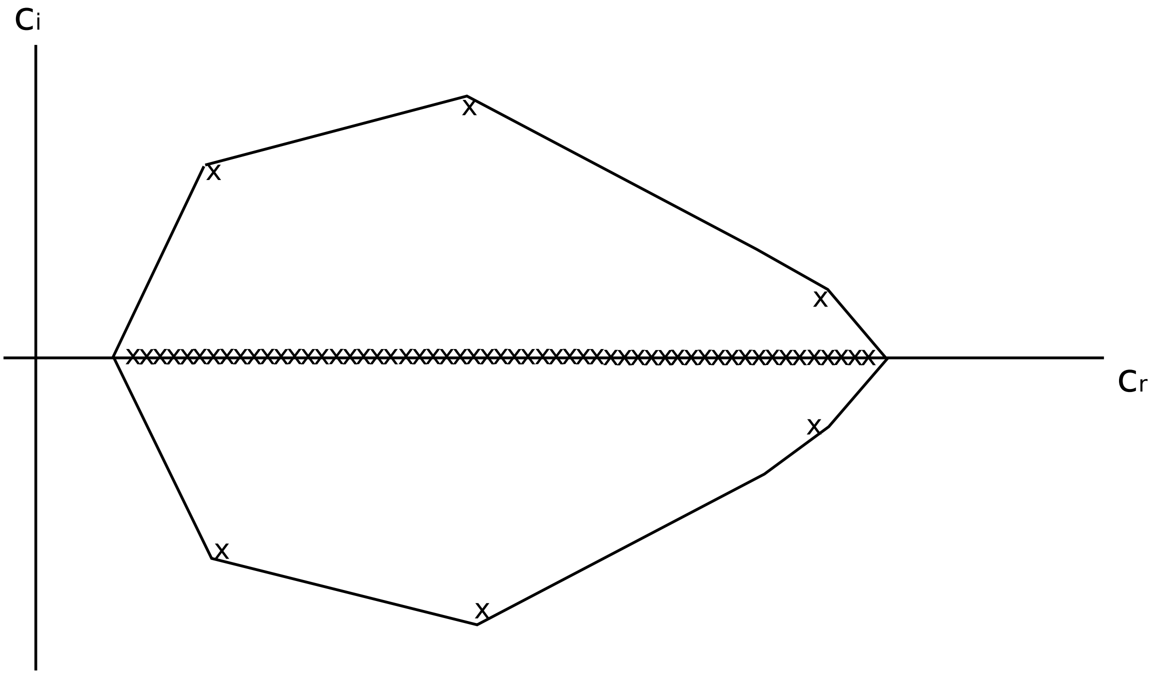

Fig. 22. The solid line is the convex hull, x's represent eigenvalues, the iterative method will converge to the eigenvalues off the real line, nearest the solid line

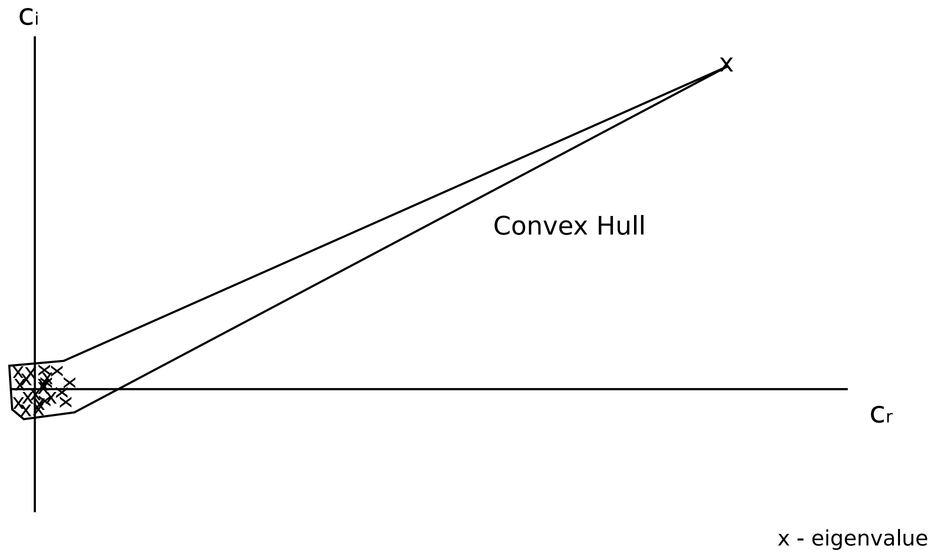

Fig. 23. Shift invert transform mapping the eigenvalue of interest toward ∞ and all others toward zero

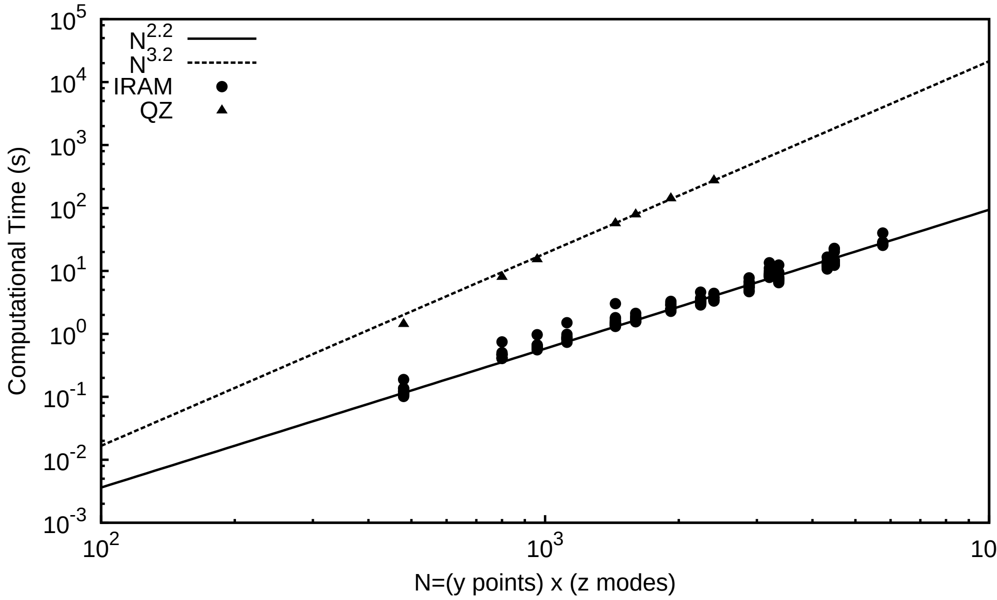

Fig. 24. Computational time comparison between QZ factorization method and implicitly restarted Arnoldi method for fundamental sinuous instability

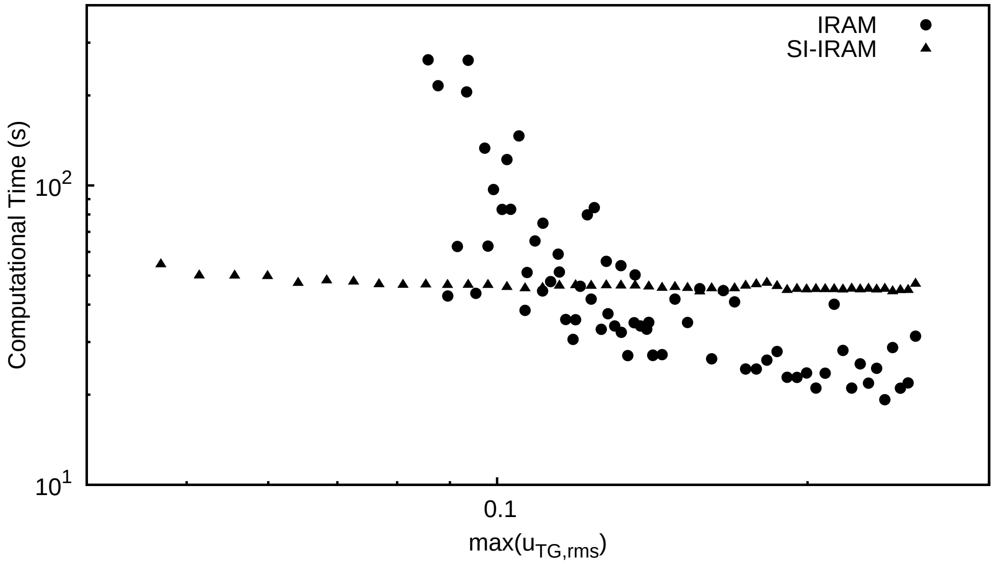

Fig. 25. Computational time comparison between standard and shift-invert eigenvalue problem for decreasing basic state amplitude

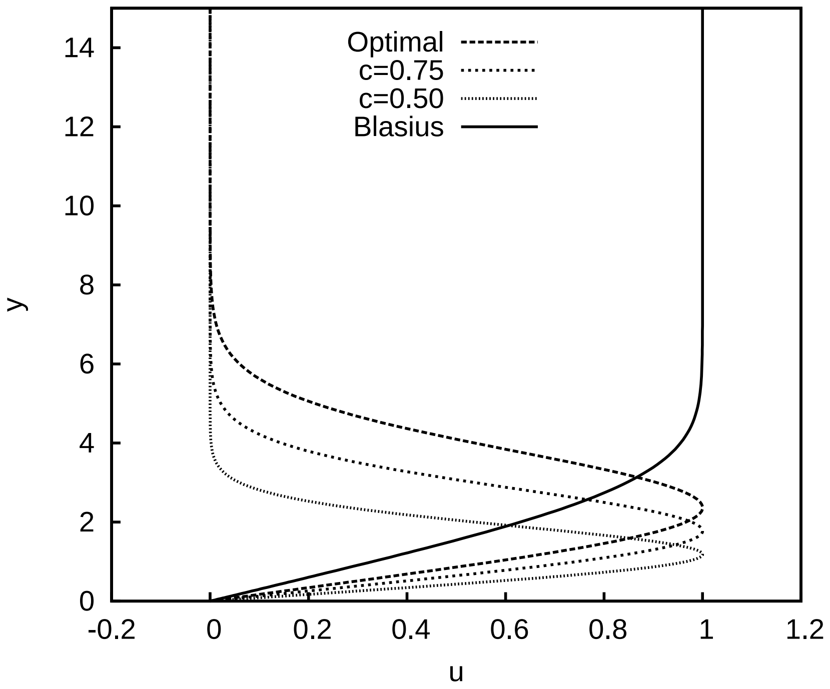

Fig. 26. Streamwise velocity profiles, model streak basic state

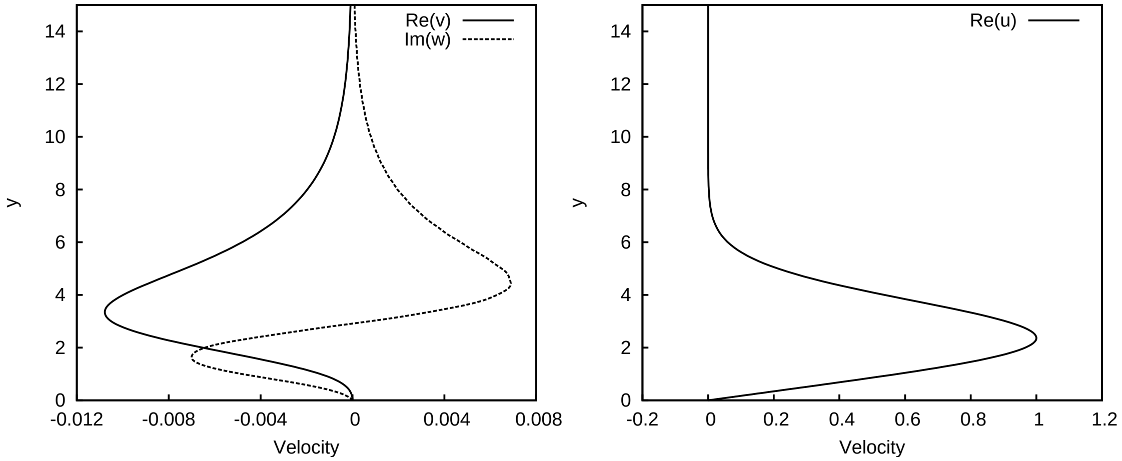

(a) Initial condition

(b) Optimal profile, $x/\delta = 10^3$

Fig. 27. Optimal perturbation, spanwise and wall-normal velocity (left) and streamwise velocity (right), $Re = 10^3$, $\beta = 0.45$, $\omega = 0$

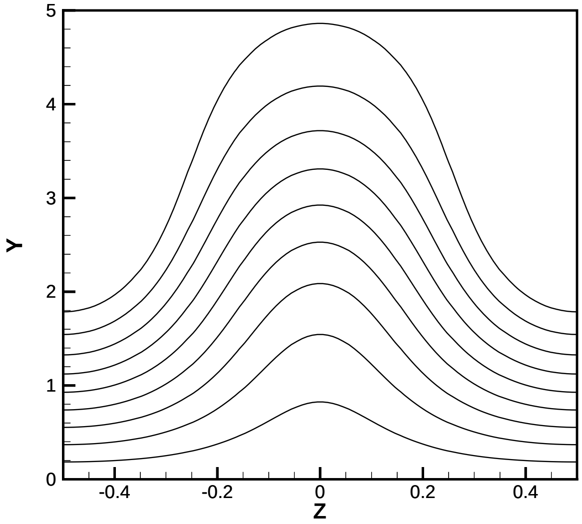

Fig. 28. Streamwise velocity, optimal basic state, $A_s = 0.36$, lines are $10\%U_\infty$

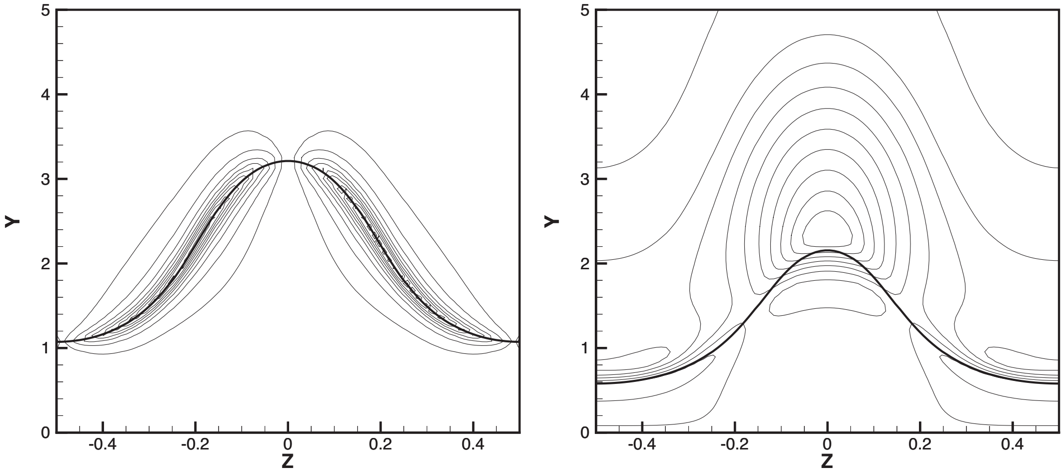

(a) Fundamental sinuous mode, $c = 0.575$, $\omega_i = 0.0036$

(b) Fundamental varicose mode, $c = 0.314$, $\omega_i = 0.008$

Fig. 29. $A_s = 36\%$, $\alpha = 0.13$, contours are 10% $|\tilde{u}|$, thick line is basic state velocity at the critical layer $U = c_r$

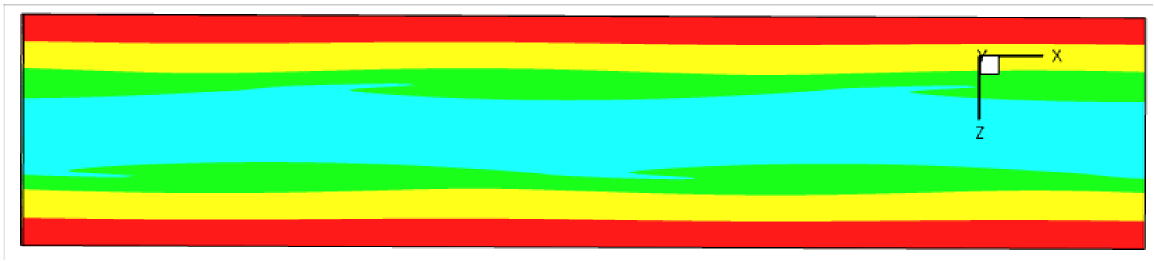

Fig. 30. Top down view of sinuous streak instability, contours of streamwise velocity

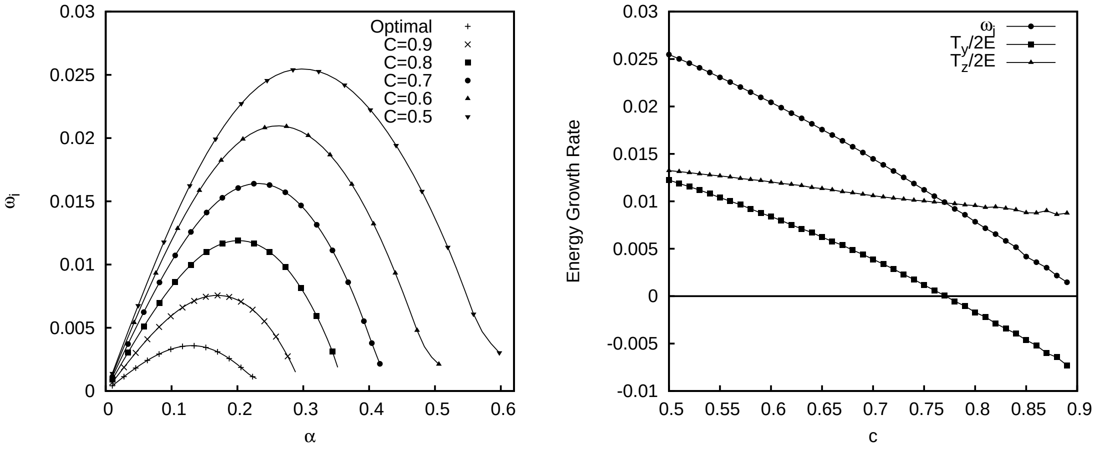

(a) Increase in temporal growth rate with sub-optimality

(b) Change in energy production for fixed $\alpha = 0.3$

Fig. 31. Effect of the perturbation height, $A_s = 36\%$, $y \rightarrow cy$

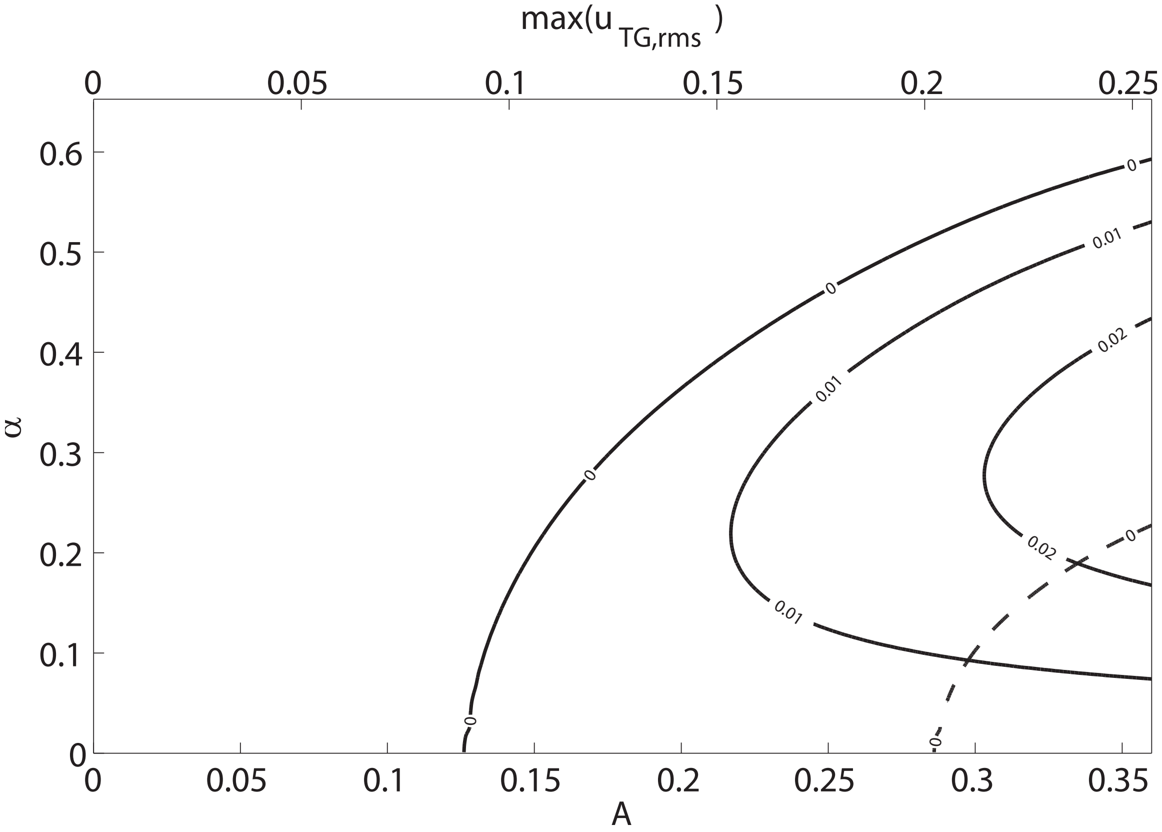

Fig. 32. Curves of constant growth rate (ω_i) for the dominant sinuous mode – optimal perturbation (dashed) and rescaled perturbation (solid)

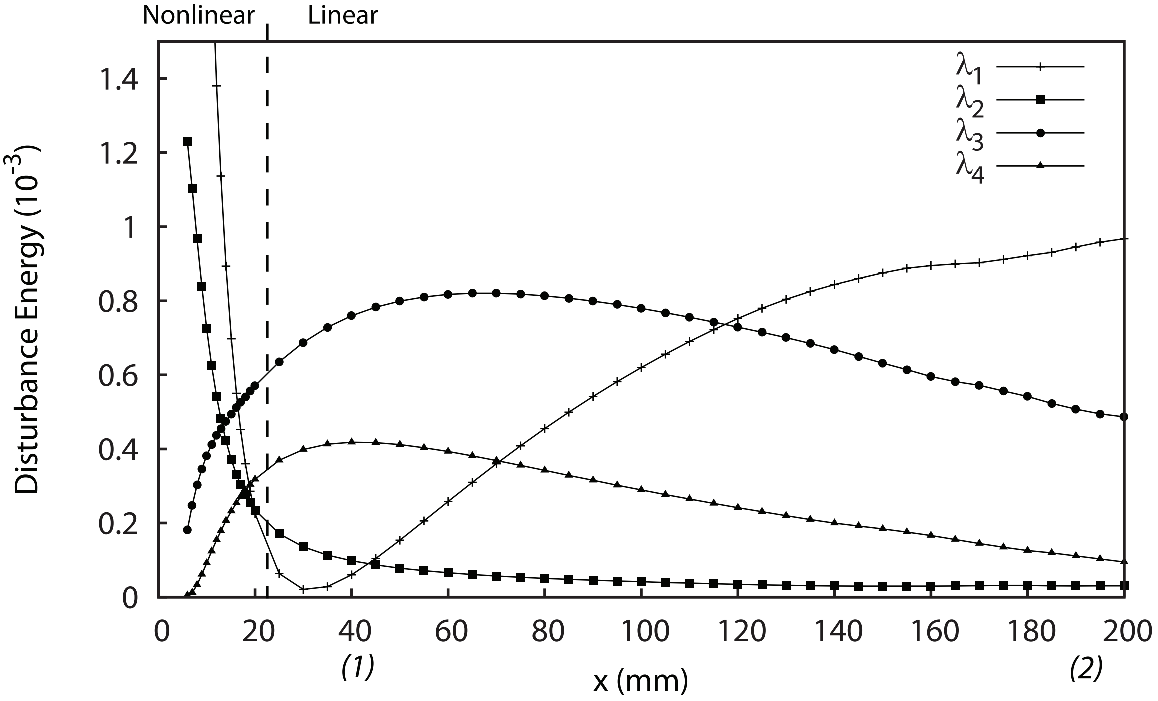

Fig. 33. Streamwise energy evolution for spanwise harmonics from DNS of Ref. [39]

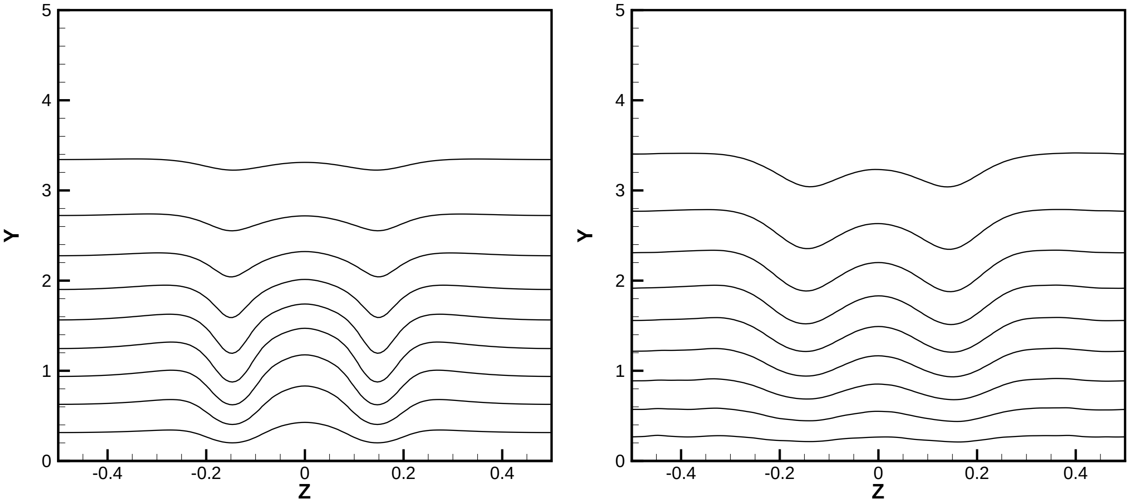

(a) 40mm downstream – station 1

(b) 190mm downstream – station 2

Fig. 34. Basic state streamwise velocity from DNS of Ref. [39] – lines are $10\% U_\infty$

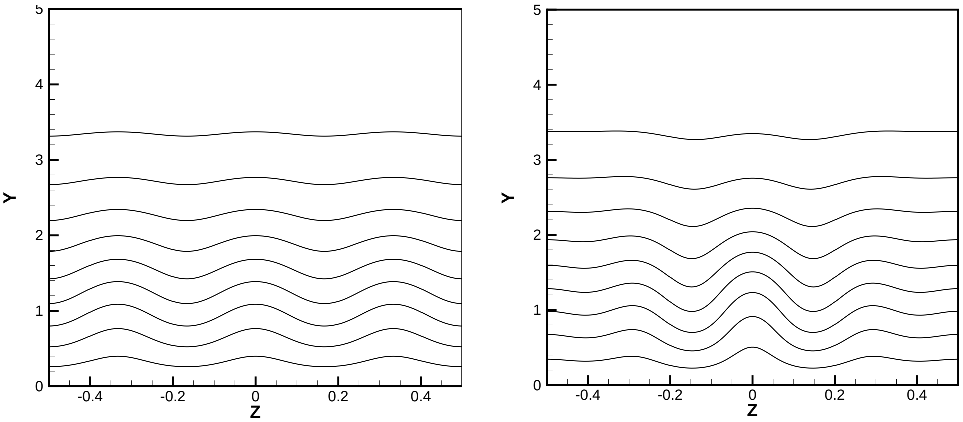

(a) A: 1 mode ($\lambda_k/3$)　(b) B: First 4 modes

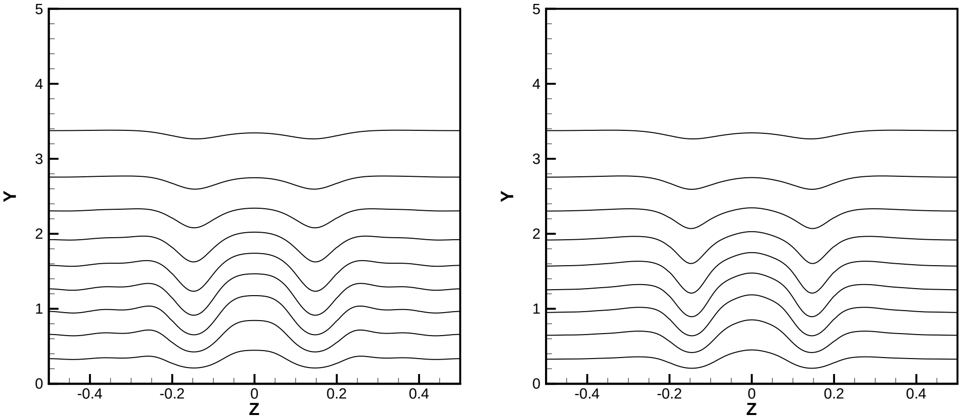

(c) C: First 7 modes　(d) D: First 11 modes

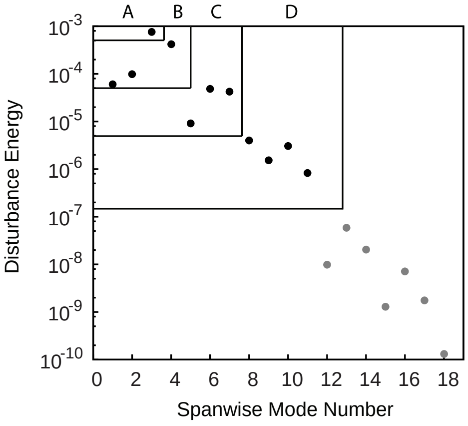

(e) Modal Energy Components

Fig. 35. Basic states – streamwise velocity contours 40mm downstream

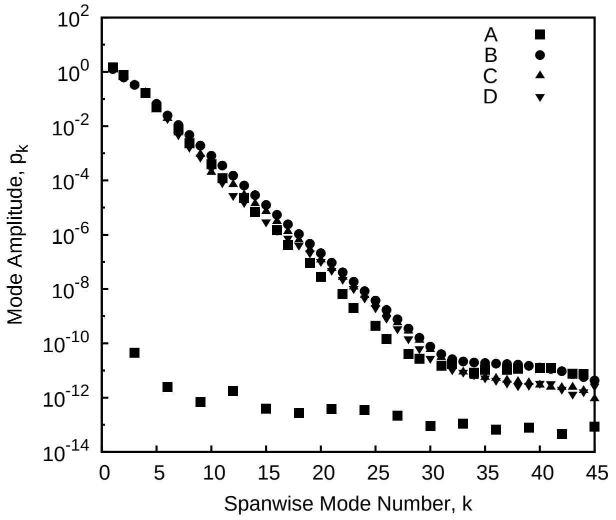

Fig. 36. Mode amplitudes for sinuous secondary instability

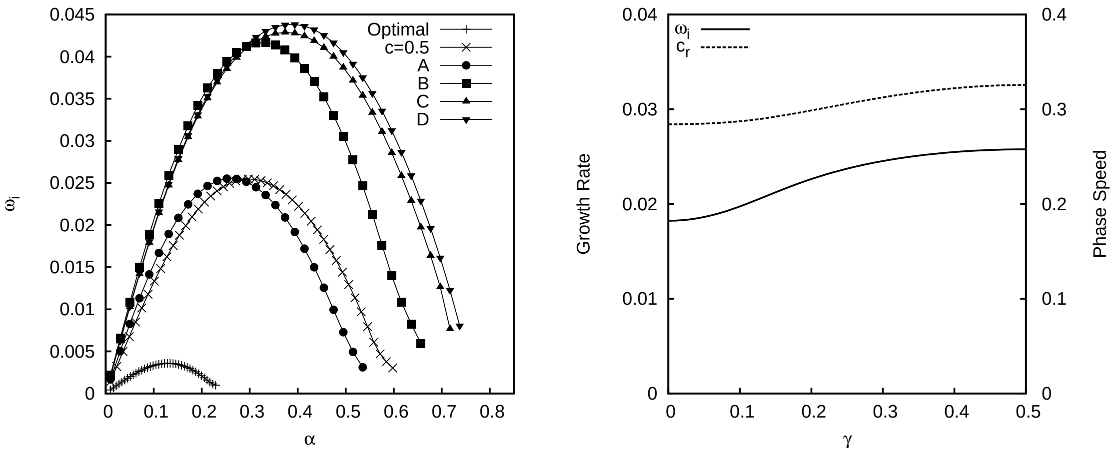

(a) Growth rate with increasing complexity

(b) Subharmonic effect for case A, $\alpha = 0.3$

Fig. 37. Constant $u_{TG,\mathrm{rms}} = 36\%/\sqrt{2}$, DNS basic state

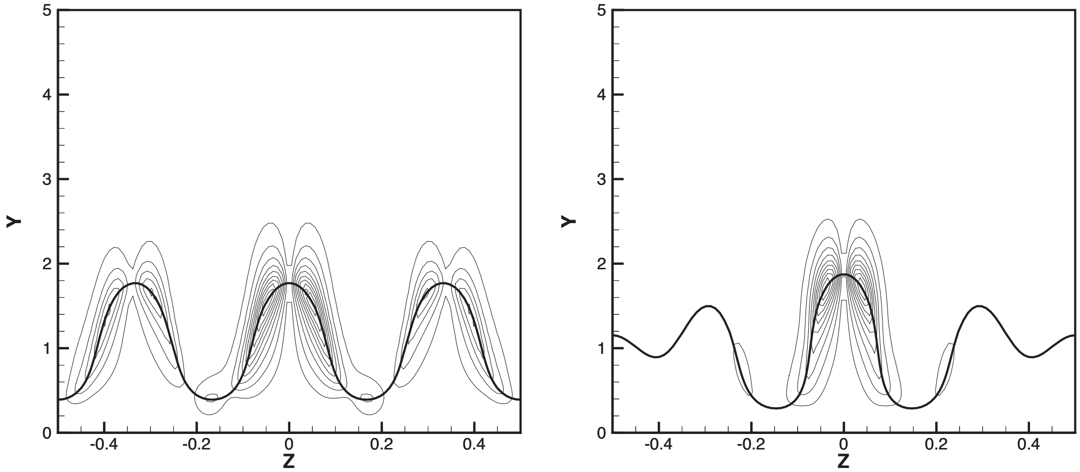

(a) Case A: 1 basic state, 45 disturbance modes ($\lambda_k/3$), $c_r = 0.316$

(b) Case B: First 4 basic state modes, $c_r = 0.296$

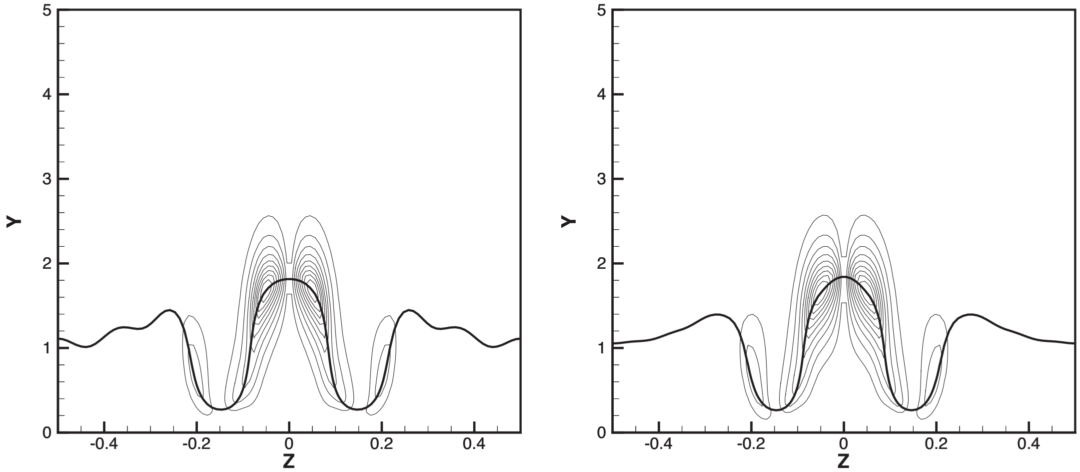

(c) Case C: First 7 basic state modes, $c_r = 0.315$

(d) Case D: First 11 basic state modes, $c_r = 0.318$

Fig. 38. Sinuous secondary instability – 40mm downstream, $u_{TG,\mathrm{rms}} = 36\%/\sqrt{2}$, $\alpha = 0.3$

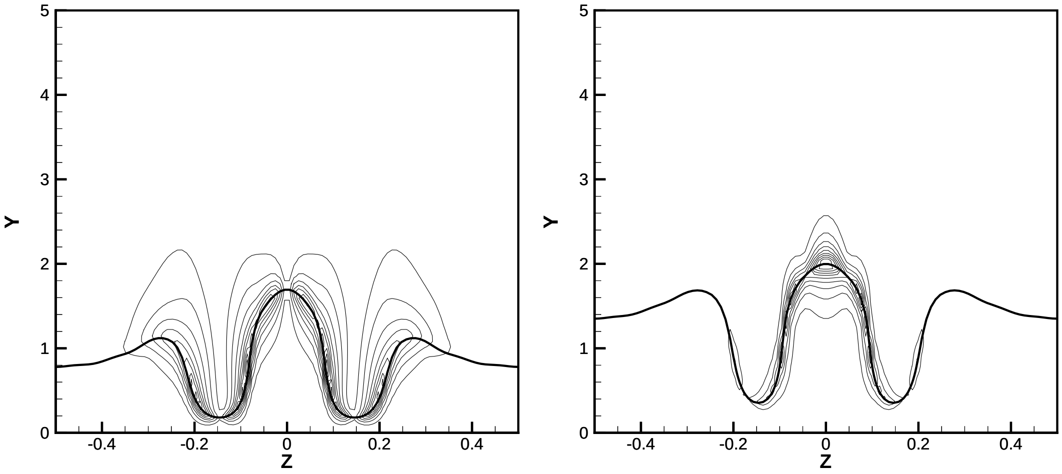

(a) Sinuous mode 2, $c_r = 0.218$ (b) Varicose mode 2, $c_r = 0.425$

Fig. 39. Additional modes, DNS basic state, $u'_{\rm rms} = 36\%/\sqrt{2}$, $\alpha = 0.1$

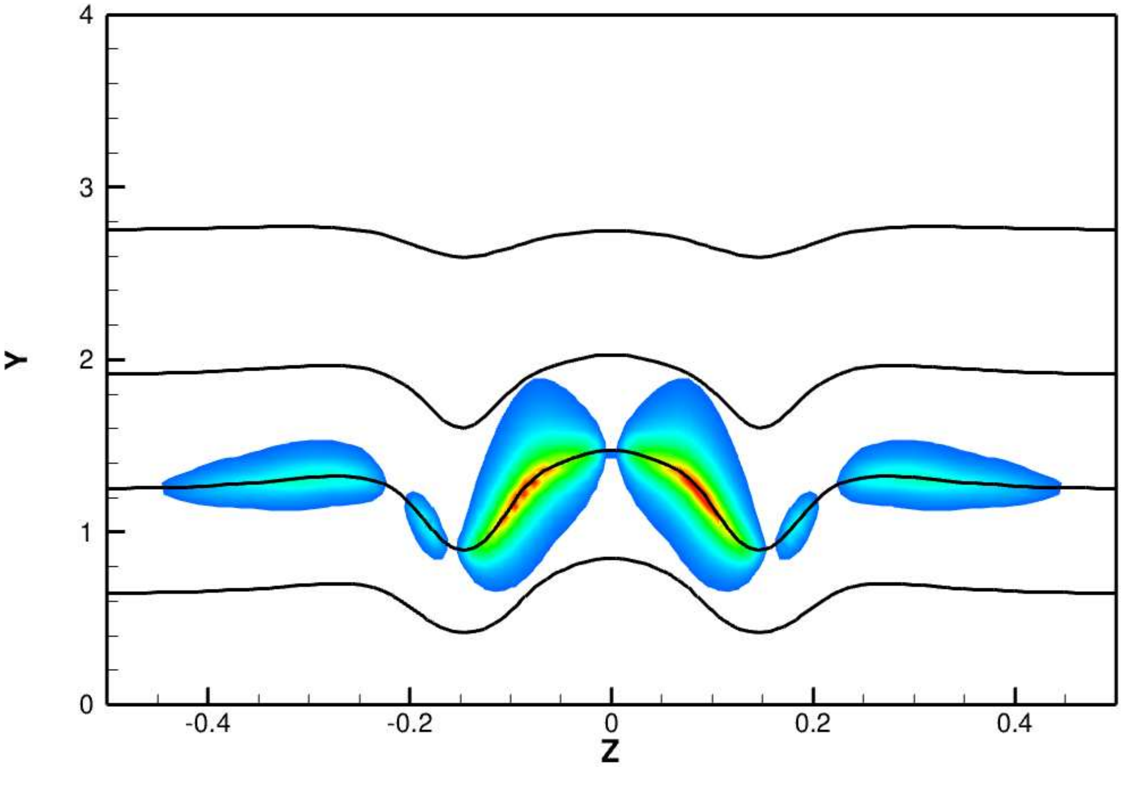

Fig. 40. Fundamental sinuous mode, $Re_k = 202$, 40mm downstream, solid lines are 10% U_∞, colors are fluctuating $|\tilde{u}|$

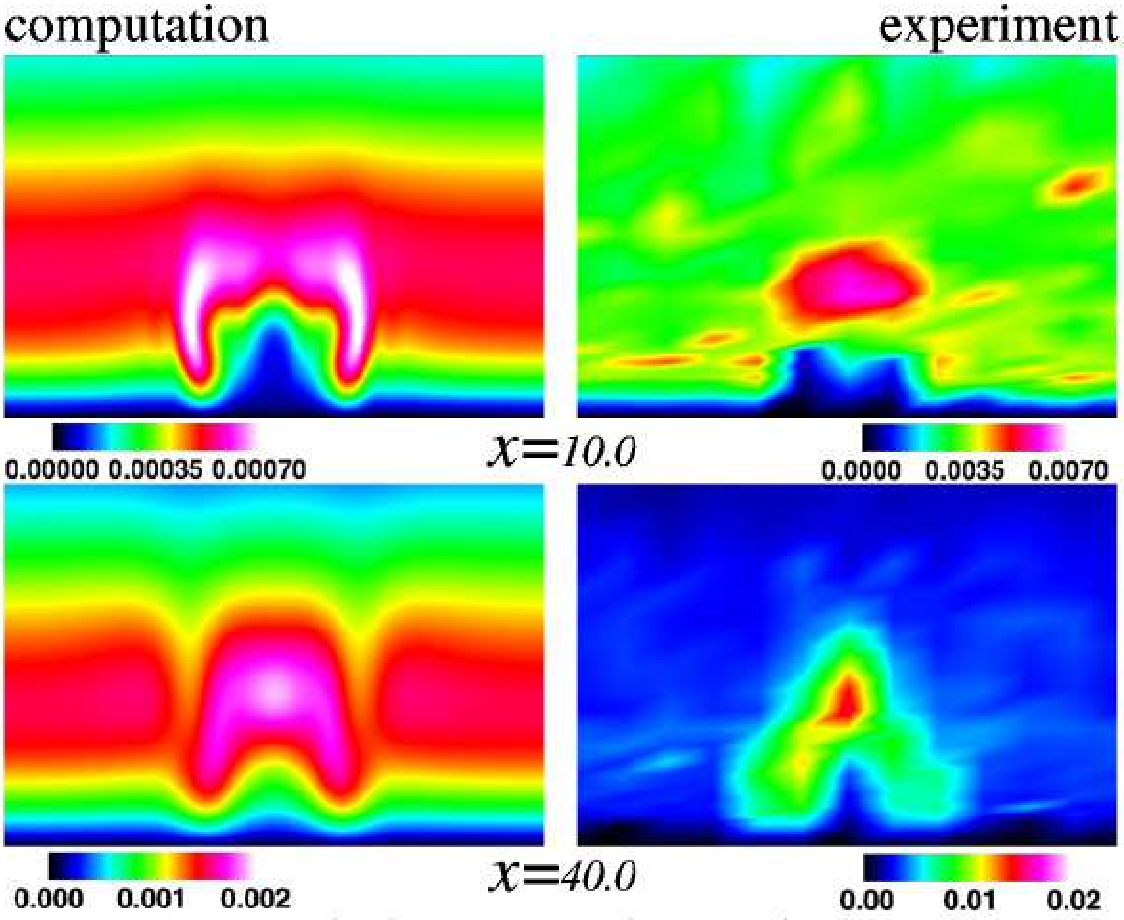

Fig. 41. Figure from Ref. [69], DNS and experimental[52] fluctuating streamwise velocity, $Re_k = 202$, 40mm downstream

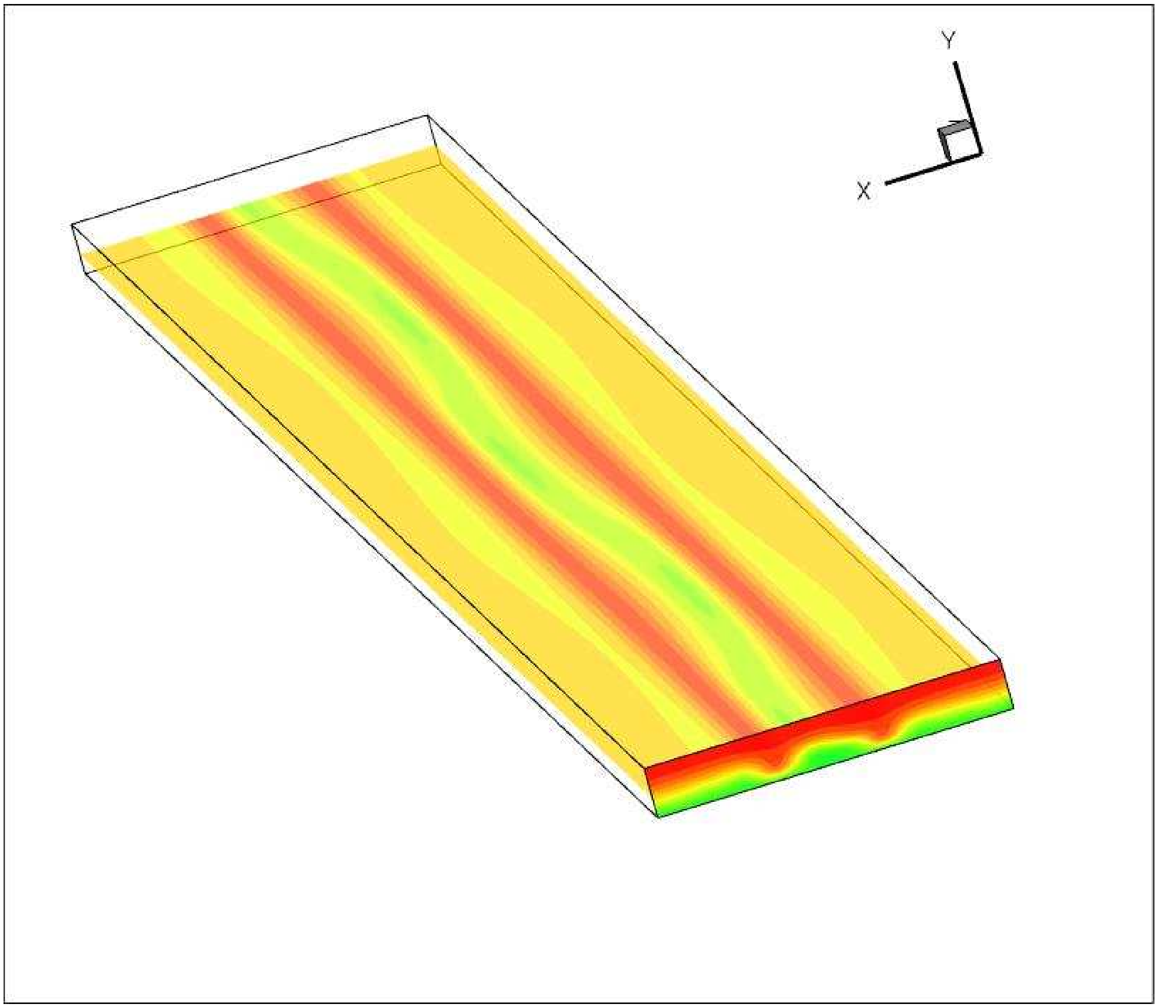

Fig. 42. 3D streamwise velocity contour slices, basic state plus fundamental sinuous mode

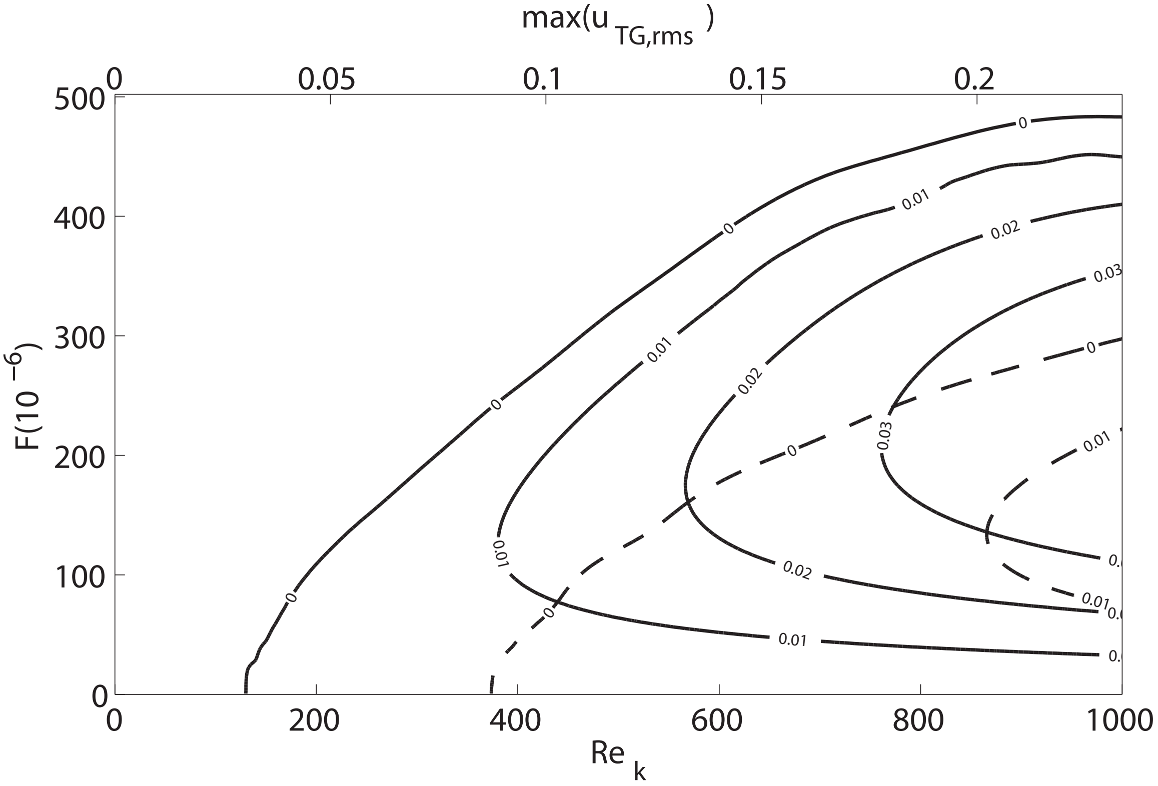

Fig. 43. Growth rate curves for the dominant sinuous mode – DNS basic state, 40 mm downstream (Solid), and 190 mm downstream (dashed)

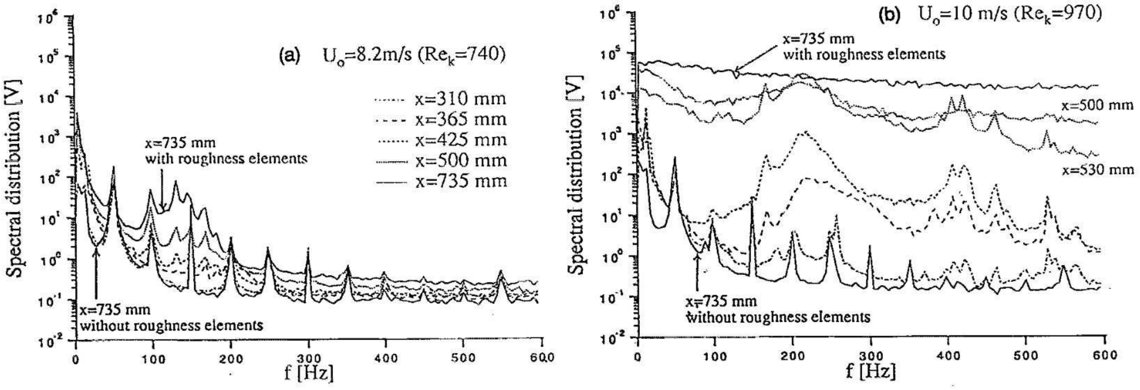

Fig. 44. Spectra from Ref. [25], $Re_k \approx 750$ (left) and $Re_k \approx 1000$ (right)

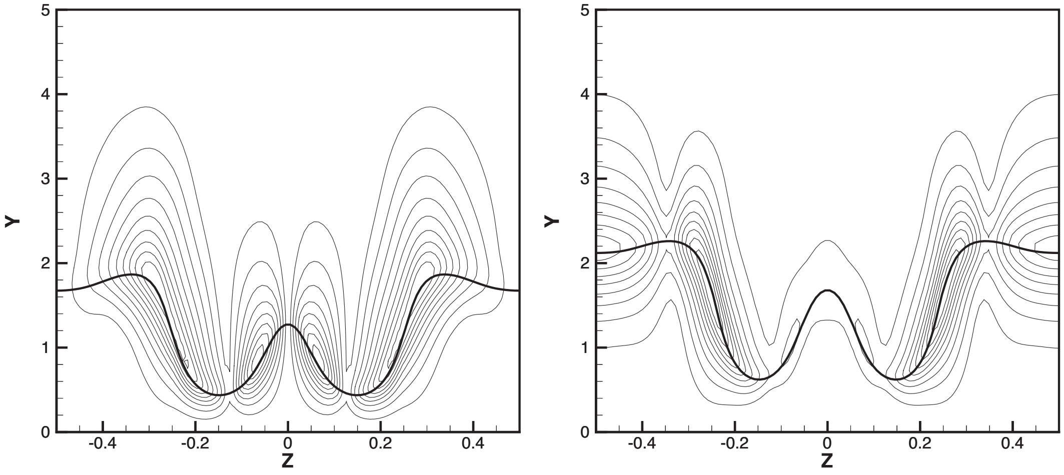

(a) Sinuous mode, $c_r = 0.334$ (b) Varicose mode, $c_r = 0.234$

Fig. 45. Far wake modes, DNS basic state, $u_{TG,\mathrm{rms}} = 36\%/\sqrt{2}$, $\alpha = 0.05$

REFERENCES

[1] F. White, *Viscous Fluid Flow*, 2nd ed. New York: McGraw Hill, 1995.

[2] T. Ellingsen and E. Palm, "Stability of linear flow," *Phys. Fluids*, vol. 18, pp. 487–488, 1975.

[3] M. T. Landahl, "A note on an algebraic instability of inviscid parallel shear flows," *J. Fluid Mech.*, vol. 98, pp. 243–251, 1980.

[4] L. S. Hultgren and L. H. Gustavsson, "Algebraic growth of disturbances in a laminar boundary layer," *Phys. Fluids*, vol. 24, pp. 1000–1005, 1981.

[5] E. Reshotko, "Transient growth—A factor in bypass transition," *Phys. Fluids*, vol. 13, no. 5, pp. 1067–1075, 2001.

[6] M. Morkovin, E. Reshotko, and T. Herbert, "Transition in open flow systems—A reassessment," *Bull. APS*, vol. 39, no. 9, p. 1882, 1994.

[7] E. Reshotko and L. Leventhal, "Preliminary experimental study of disturbances in a laminar boundary layer due to distributed roughness," ser. AIAA Paper 81-1224, 1981.

[8] T. C. Corke, A. Bar-Sever, and M. V. Morkovin, "Experiments on transition enhancement by distributed roughness," *Phys. Fluids*, vol. 29, no. 10, pp. 3199–3213, 1986.

[9] J. Kendall, "Laminar boundary layer velocity distortion by surface roughness: Effect upon stability," ser. AIAA Paper 81-0195, 1981.

[10] J. H. M. Fransson, L. Brandt, A. Talamelli, and C. Cossu, "Experimental study of the stabilization of Tollmien–Schlichting waves by finite amplitude streaks," *Phys. Fluids*, vol. 17, no. 5, pp. 054 110–(1–15), 2005.

[11] C. Cossu and L. Brandt, "Stabilization of Tollmien–Schlicting waves by finite amplitude optimal streaks in the Blasius boundary layer," *Phys. Fluids*, vol. 14, no. 8, pp. L57–L60, 2002.

[12] R. Hanson, P. Lavoie, A. Naguib, and J. Morrison, "Control of transient growth induced boundary layer transition using plasma actuators," in *Seventh IUTAM Symposium on Laminar-Turbulent Transition*, ser. IUTAM Bookseries, P. Schlatter and D. Henningson, Eds. New York: Springer, 2010, vol. 18, pp. 183–188.

[13] E. Reshotko, "Roughness–induced transition, experiment and modeling," ser. AIAA Paper 2008-4294, 2008.

[14] E. B. White, "Transient growth of stationary disturbances in a flat plate boundary layer," *Phys. Fluids*, vol. 14, no. 12, pp. 4429–4439, 2002.

[15] E. B. White, J. M. Rice, and F. G. Ergin, "Receptivity of stationary transient disturbances to surface roughness," *Phys. Fluids*, vol. 17, no. 6, pp. 064 109–(1–12), 2005.

[16] C. E. Grosch and H. Salwen, "The continuous spectrum of the orr–sommerfeld equation. Part 1. The spectrum and the eigenfunctions." *J. Fluid Mech.*, vol. 87, pp. 33–54, 1978.

[17] H. L. Dryden, "Review of published data on the effect of roughness on transition from laminar to turbulent flow," *J. Aero. Sci.*, vol. 20, no. 7, pp. 477–482, July 1953.

[18] P. Klebanoff, G. Schubauer, and K. Tidstrom, "Measurements of the effect of two-dimensional and thee-dimensional roughness elements on boundary-layer transition," *J. Aero. Sci.*, vol. 22, pp. 803–804, 1955.

[19] N. Gregory and W. S. Walker, "The effect on transition of isolated surface excrescences in the boundary layer," Aero. Res. Council, Tech. Rep. R. & M. 2779, 1956.

[20] I. Tani, "Boundary-layer transition," *Annu. Rev. Fluid Mech.*, vol. 1, pp. 169–196, 1969.

[21] M. V. Morkovin, "On roughness-induced transition: Facts, views & speculation," in *Instability and Transition*, M. Y. Hussaini and R. G. Voight, Eds., vol. 1. New York: Springer, 1990, pp. 281–295.

[22] R. Norman, "On obstacle-generated secondary flows in laminar boundary layers and transition to turbulence," Ph.D. dissertation, Illinois Institute of Technology, 1972.

[23] T. Herbert, "Secondary instability of boundary layers," *Annu. Rev. Fluid Mech.*, vol. 20, pp. 487–526, 1988.

[24] P. Klebanoff, W. Cleveland, and K. Tidstrom, "On the evolution of a turbulent boundary layer induced by a three-dimensional roughness element," *J. Fluid Mech.*, vol. 237, pp. 101–187, 1992.

[25] A. Bakchinov, G. Grek, B. Klingman, and V. Kozlov, "Transition experiments in a boundary layer with embedded streamwise vortices," *Phys. Fluids*, vol. 7, no. 4, pp. 820–832, 1995.

[26] K. Butler and B. Farrell, “Three-dimensional optimal perturbations in viscous shear flow,” *Phys. Fluids A*, vol. 4, no. 8, pp. 1637–1650, 1992.

[27] P. J. Schmid, D. S. Henningson, M. R. Khorami, and M. R. Malik, “A study of eigenvalue sensitivity for hydrodynamic stability operators,” *Theor. Comput. Fluid Dyn.*, vol. 4, pp. 227–240, 1993.

[28] P. J. Schmid and D. S. Henningson, “Optimal energy density growth in hagen-poiseuille flow,” *J. Fluid. Mech.*, vol. 277, pp. 197–225, 1994.

[29] P. Andersson, M. Berggren, and D. S. Henningson, “Optimal disturbances and bypass transition in boundary layers,” *Phys. Fluids*, vol. 11, no. 1, pp. 134–150, 1999.

[30] A. Tumin and E. Reshotko, “Spatial theory of optimal disturbances in boundary layers,” *Phys. Fluids*, vol. 13, no. 7, pp. 2097–2104, 2001.

[31] K. J. A. Westin, A. V. Boiko, B. G. B. Klingmann, V. V. Kozlov, and P. H. Alfredsson, “Experiments in a boundary layer subjected to free stream turbulence. Part 1. Boundary layer structure and receptivity,” *J. Fluid Mech.*, vol. 281, pp. 193–218, 1994.

[32] M. Matsubara and P. H. Alfredsson, “Disturbance growth in boundary layers subjected to free-stream turbulence,” *J. Fluid Mech.*, vol. 430, pp. 149–168, 2001.

[33] P. Andersson, L. Brant, B. Allessandro, and D. Henningson, “On the breakdown of boundary layer streaks,” *J. Fluid Mech.*, vol. 428, pp. 29–60, 2001.

[34] C. Cossu and L. Brandt, “On Tollmien–Schlichting-like waves in streaky boundary layers,” *European J. Mech. B/Fluids*, vol. 23, no. 6, pp. 815–833, 2004.

[35] J. H. M. Fransson, L. Brandt, A. Talamelli, and C. Cossu, “Experimental and theoretical investigation of the non-modal growth of steady streaks in a flat plate boundary layer,” *Phys. Fluids*, vol. 16, no. 10, pp. 3627–3638, 2004.

[36] F. G. Ergin and E. B. White, “Unsteady and transitional flows behind roughness elements,” *AIAA Journal*, vol. 44, no. 11, pp. 2504–2514, 2006.

[37] N. A. Denissen and E. B. White, “Roughness induced bypass transition, revisited,” *AIAA Journal*, vol. 46, no. 7, pp. 1874–1877, 2008.

[38] P. Fischer and M. Choudhari, “Numerical simulation of roughness-induced transient growth in a laminar boundary layer,” ser. AIAA Paper 2004-2539, 2004.

[39] D. P. Rizzetta and M. R. Visbal, “Direct numerical simulations of flow past an array of distributed roughness elements,” *AIAA J.*, vol. 45, no. 8, pp. 1967–1976, August 2007.

[40] K. A. Stephani, J. Albright, C. Doolittle, M. Jackson, and D. Goldstein, “DNS study of transient disturbance growth and bypass transition,” ser. AIAA Paper 2009-0585, 2009.

[41] R. S. Downs III, E. B. White, and N. A. Denissen, “Transient growth and transition induced by random distributed roughness,” *AIAA Journal*, vol. 42, no. 2, pp. 451–462, 2008.

[42] A. Tumin, “Multimode decomposition of spatially growing perturbations in a two-dimensional boundary layer,” *Phys. Fluids*, vol. 15, no. 9, pp. 2525–2540, 2003.

[43] H. Salwen and C. E. Grosch, “The continuous spectrum of the orr–sommerfeld

equation. Part 2. Eigenfunction expansions." *J. Fluid Mech.*, vol. 104, pp. 445–465, 1981.

[44] D. Ashpis and E. Reshotko, "The vibrating ribbon problem revisited," *J. Fluid Mech.*, vol. 213, pp. 531–547, 1990.

[45] P. Luchini, "Reynolds-number-independent instability of the boundary layer over a flat surface: Optimal perturbations," *J. Fluid Mech.*, vol. 404, pp. 289–309, 2000.

[46] P. J. Schmid and D. S. Henningson, *Stability and Transition in Shear Flows.* New York: Springer, 2001.

[47] N. A. Denissen and E. B. White, "Continuous spectrum analysis of roughness-induced transient growth," *Phys. Fluids*, vol. 21, no. 11, pp. 114 105–(1–13), 2009.

[48] A. Tumin, X. Wang, and X. Zhong, "Direct numerical simulation and the theory of receptivity in a hypersonic boundary layer," *Phys. Fluids*, vol. 19, no. 1, pp. 014 101–(1–14), 2007.

[49] A. Tumin, M. Amitay, C. Jacob, and M. D. Zhou, "A normal multimode decomposition method for stability experiments," *Phys. Fluids*, vol. 8, no. 10, pp. 2777–2779, 1996.

[50] V. S. A.N. Tikhonov, A.V. Goncharsky and A. Yagola, *Numerical Methods for the Solution of Ill-Posed Problems*, English ed. Boston: Kluwer Academic Publishers, 1995.

[51] A. Tumin and E. Reshotko, "Receptivity of a boundary-layer flow to a three-dimensional hump at finite reynolds numbers," *Phys. Fluids*, vol. 17, no. 9, pp.

094 101–(1–8), 2005.

[52] F. G. Ergin and E. B. White, “Unsteady and transitional flows behind roughness elements,” *AIAA J.*, vol. 44, no. 11, pp. 2504–2514, 2006.

[53] A. Tumin and E. Reshotko, “The problem of boundary-layer flow encountering a three-dimensional hump revisited,” ser. AIAA Paper 2004-0101, 2004.

[54] N. A. Denissen, R. S. Downs III, and E. B. White, “Transient growth due to surface roughness: Theory, simulation and experiment,” ser. AIAA Paper 2009-175, 2009.

[55] P. Klebanoff, K. Tidstrom, and L. Sargent, “The three-dimensional nature of boundary-layer instability,” *J. Fluid Mech.*, vol. 12, pp. 1–34, 1962.

[56] W. Saric and A. Thomas, “Experiments on the subharmonic route to turbulence in boundary layers,” in *Turbulence and Chaotic Phenomena in Fluids*, T. Tatsumi, Ed. Amsterdam: North-Holland, 1984, pp. 117–122.

[57] H. Reed, “Wave interactions in swept-wing flows,” *Phys. Fluids*, vol. 30, no. 11, pp. 3419–3426, 1987.

[58] M. R. Malik, F. Li, and C.-L. Chang, “Crossflow disturbances in three-dimensional boundary layers: Nonlinear development, wave interaction and secondary instability,” *J. Fluid Mech.*, vol. 268, pp. 1–36, 1994.

[59] C. Mack and P. Schmid, “A preconditioned Krylov technique for global hydrodunamic stability analysis of large-scale compressible flows,” *Journal of Computational Physics*, vol. 229, pp. 541–560, 2010.

[60] C.-L. Chang, “Langley stability and transition analysis code (lastrac) version 1.2

user's manual," NASA Langley Research Center, Tech. Rep. NASA/TM-2004-213233, 2004.

[61] R. Lehoucq, D. Sorensen, and C. Yang, "Arpack users' guide. Software, environments and tools," Society for Industrial and Applied Mathematics, Tech. Rep., 1999.

[62] R. Lehoucq and J. A. Scott, "An evaluation of software for computing eigenvalues of sparse nonsymmetric matrices," Argonne National Laboratory, Argonne, IL, Tech. Rep. MCS-P547-1195, 1996.

[63] P. J. Schmid, "The description of fluid behavior by coherent structures," in *Seventh IUTAM Symposium on Laminar-Turbulent Transition*, ser. IUTAM Bookseries, P. Schlatter and D. Henningson, Eds. New York: Springer, 2010, vol. 18, pp. 51–58.

[64] C. Lin, "Some mathematical problems in the theory of the stability of parallel flows," *Journal of Fluid Mechanics*, vol. 10, no. 3, pp. 430–438, 1961.

[65] P. Schlatter, L. Brandt, H. Lange, and D. Henningson, "On streak breakdown in bypass transition," *Physics of Fluids*, vol. 20, no. 10, pp. 101 505–(1–15), 2008.

[66] L. Hunt, R. S. Downs III, M. Kuester, E. White, and W. Saric, "Flow quality measurements in the klebanoff-saric wind tunnel," ser. AIAA Paper 2010-4538, 2010.

[67] A. Hanifi, P. Schmid, and D. Henningson, "Transient growth in compressible boundary layer flow," *Physics of Fluids*, vol. 3, no. 8, pp. 826–837, 1996.

[68] Y. Saad, *Iterative Methods for Sparse Linear Systems*, 1st ed. Philadelphia: PWS Publishing, 1996.

[69] D. P. Rizzetta and M. R. Visbal, “Direct numerical simulations of flow past an array of distributed roughness elements,” ser. AIAA Paper 2006-2865, 2006.

VITA

Name Nicholas Allen Denissen

Address Department of Aerospace Engineering
H.R. Bright Building, Rm. 701, Ross Street
Texas A&M University, College Station, TX 77843-3141

Email nad11@tamu.edu

Education B.S. Aerospace Engineering, Case Western Reserve University, 2007
Ph.D. Aerospace Engineering, Texas A&M University, 2011

Professional Experience Assistant Lecturer, January 2010–Present, Texas A&M University, Department of Aerospace Engineering
NSF Graduate Research Fellow, August 2008–Present
Texas A&M National Excellence Fellow/Regents Fellow, August 2007–Present